INL/EXT-18-51320-Revision-0

Characterization Report on Optimized Fuel Compositions for Improved Fuel Performance and FCCI

Michael T Benson

September 2018

INL/EXT-18-51320-Revision-0

Characterization Report on Optimized Fuel Compositions for Improved Fuel Performance and FCCI

Michael T Benson

September 2018

Idaho National Laboratory
Idaho Falls, Idaho 83415

http://www.inl.gov

Prepared for the
U.S. Department of Energy

Under DOE Idaho Operations Office
Contract DE-AC07-05ID14517

INL/EXT-18-51320
Revision 0

Characterization Report on Optimized Fuel Compositions for Improved Fuel Performance and FCCI

Nuclear Technology Research and Development

Prepared for
U.S. Department of Energy
Advanced Fuels Campaign
Michael T. Benson
Idaho National Laboratory
September 2018
NTRD-FUEL-2018-000088

ABSTRACT

This milestone report contains four manuscripts (accepted versions) and one conference proceedings, all published in FY18 and presented in their entirety. The only changes to these documents are that the Figure and Table labels now represent the appropriate Section within this document, and the references have been co-located. The as-cast and annealed characterization of U-10Zr alloys containing the additive Sn are described. The conference proceedings in the next section continues that work, with results of a diffusion couple between U-10Zr-4.3Sn and the Ln mix. Tin is a promising fuel additive. These papers are the first investigations of tin's ability to bind the lanthanides in a metallic fuel. Another promising additive is antimony. The next section details the investigation of the alloys U-10Zr-2Sn-2Sb and U-10Zr-2Sn-2Sb-4Ln. In this mixed additive system, the different reactivities of Sn and Sb towards Zr and the lanthanides are discussed. The final two sections are continuations of previous studies using Pd and a fuel additive. The annealed alloys U-12Zr-4Pd and U-12Zr-4Pd-4.3Ln are characterized, while in the last section, Pu has been added to the alloys containing Pd, to investigate the efficacy of using Pd in a transmutation fuel.

INTENTIONALLY BLANK

CONTENTS

FIGURES

TABLES

INTENTIONALLY BLANK

ACRONYMS

BSE	Backscattered electrons
DSC	Differential Scanning Calorimetry
EBR-II	Experimental Breeder Reactor -II
EDS	Energy Dispersive X-ray Spectrometer
EML	Electron Microscopy Laboratory
FCCI	Fuel-Cladding Chemical Interaction
FEG	Field emission gun
FFTF	Fast Flux Test Facility
FIB	Focused ion beam
FMF	Fuel Manufacturing Facility
HAADF	High angle annular dark-field
ICP-MS	Inductively coupled plasma mass spectrometry
JCPDS	Joint Committee on Powder Diffraction Standards
JEOL	Japan Electron Optics Laboratory
Ln	Lanthanides
Ln mix	53Nd-25Ce-16Pr-6La
PIE	Post-Irradiation Examination
SAED	Selected area electron diffraction
SEM	Scanning Electron Microscope
STEM	Scanning transmission electron microscope
TEM	Transmission electron microscope
U.S. DOE	United States Department of Energy
WDS	Wavelength dispersive spectroscopy
XRD	X-ray Diffraction

INTENTIONALLY BLANK

1. INTRODUCTION

Fuel-cladding chemical interaction (FCCI) occurs when the nuclear fuel or fission products react with the cladding material. A major cause of FCCI in U-Zr and U-Pu-Zr fuels during irradiation is fission product lanthanides (Ln), which tend to migrate to the fuel periphery, coming in contact with the cladding. The result of this interaction is degradation of the cladding and will eventually lead to rupture of the fuel assembly [1][2]. The lanthanides can be created as fission products or can be present in fuel produced with recycled uranium. A small amount of lanthanides is expected to remain with uranium after pyroprocessing, thus being incorporated into fresh fuel [3]. In this case, as soon as the fuel contacts the cladding due to swelling, at roughly 1-2% burnup, there are already lanthanide impurities in the recycled fuel available to initiate FCCI. This early form of FCCI in recycled fuel will occur in an accelerated fashion as compared to the much slower creation of fission product lanthanides in fresh fuel fabricated with clean uranium. Controlling FCCI in this system is even more important due to the potentially reduced lifetime of the fuel [4].

In order to extend fuel life while minimizing the potential occurrence of a cladding breach, some method of controlling FCCI is needed. Several methods are being investigated to decrease or prevent FCCI, such as barrier foils [5], coatings [6], and additive materials. Work in the alloy optimization area is focused on additive materials. In the additive approach, criteria were developed that identified a set of elements that could be promising additives to bind lanthanides as stable intermetallics [7]. From this list, Pd [7][8][9], Sn [10][11], Sb [12][13], and In [14] have been investigated, and have all shown promise as a fuel additive. Pd-Ln precipitates were found and characterized in a recent post-irradiation examination (PIE) [15] of a U-10Zr fuel irradiated in the Fast Flux Test Facility. The Pd is present as a fission product which creates precipitates with an average composition of 25Pd-75Ln, but not in a large enough concentration to bind all the lanthanides produced. These results are encouraging towards this method of controlling the lanthanides, especially considering that it naturally happens during irradiation.

Investigations of U-Zr alloys with the additives alone, and with the additives and a lanthanide mix, show that the additives can capture all lanthanides produced at up to 20 % burn-up [7]. The composition and ratio of lanthanides are based on elemental analysis of irradiated U-10Zr Experimental Breeder Reactor II (EBR-II) fuel pins [7], with the four most prevalent lanthanides included in the mix (referred to as either Ln mix, or simply Ln in alloy compositions). The ratio obtained from EBR-II fuel is 53Nd-25Ce-16Pr-6La, in wt. %. The starting concentrations of lanthanides in recycled fuel will have a slightly different elemental ratio, modified slightly from their fission product yields by the separation factors in the pyrometallurgical process.

This report contains four manuscripts (accepted versions) and one conference proceedings, all published in FY18, and are presented in their entirety. The only changes to these documents are that the Figure and Table labels now represent the appropriate Section within this document, and the references have been co-located in Section 7. In Section 2, the as-cast and annealed characterization of U-10Zr alloys containing the additive Sn are described. The conference proceedings in Section 3 continues that work, with results of a diffusion couple between U-10Zr-4.3Sn and the Ln mix. Section 4 details the investigation of the alloys U-10Zr-2Sn-2Sb and U-10Zr-2Sn-2Sb-4Ln. In this mixed additive system, the different reactivities of Sn and Sb towards Zr and the lanthanides are discussed. Sections 5 and 6 are investigations of Pd as an additive. In Section 5, the annealed alloys U-12Zr-4Pd and U-12Zr-4Pd-4.3Ln are characterized, while in Section 6, Pu has been added to the alloys containing Pd, to investigate the efficacy of using Pd in a transmutation fuel.

2. SEM CHARACTERIZATION OF TWO ADVANCED FUEL ALLOYS: U-10ZR-4.3SN AND U-10ZR-4.3SN-4.7LN

The full reference for the following manuscript is: M.T. Benson, J.A. King, R.D. Mariani, M.C. Marshall, “SEM characterization of two advanced fuel alloys: U-10Zr-4.3Sn and U-10Zr-4.3Sn-4.7Ln”, *J. Nucl. Mater.*, **2017**, *494*, 334-341.

2.1 Abstract

Tin is being investigated as a potential additive to metallic fuel to control fuel-cladding chemical interaction (FCCI). A primary cause of FCCI is the lanthanide fission products moving to the fuel periphery and interacting with the cladding. This interaction will lead to wastage of the cladding and eventually to a cladding breach. The current study is a scanning electron microscopy (SEM) characterization of as-cast and annealed U-10Zr-4.3Sn and U-10Zr-4.3Sn-4.7Ln, where Ln=53Nd-25Ce-16Pr-6La. The present study shows that tin preferentially binds the lanthanides, which will prevent lanthanide migration and interaction with the cladding.

2.2 Introduction

Fuel-cladding chemical interaction (FCCI) occurs when the nuclear fuel or fission products react with the cladding material. A major cause of FCCI in metallic fuels during irradiation is fission product lanthanides (Ln), which tend to migrate to the fuel periphery, coming in contact with the cladding. The result of this interaction is degradation of the cladding, and will eventually lead to rupture of the fuel assembly [1][2]. In order to extend fuel life, while making the fuel less likely to have a cladding breach, some method of controlling FCCI is needed. Several methods are being investigated to decrease or prevent FCCI, such as barrier foils, coatings, and additive materials [5][6][7][14]. In the additive approach, considering ways to bind lanthanides as stable intermetallics, criteria were developed that identified a set of elements that could be promising additives [7]. From this list, Pd [7][16][17] and In [14] have been investigated, and have both shown promise as a fuel additive.

The lanthanides can burn-in as fission products, or can be present in fuel produced with recycled uranium. A small amount of lanthanides are expected to remain with uranium after pyroprocessing, thus being incorporated into a fresh fuel [3]. In this case, as soon as the fuel contacts the cladding due to swelling, at roughly 1-2% burnup, there are already lanthanide impurities in the recycled fuel available to initiate FCCI. This early form of FCCI in a recycled fuel will occur in accelerated fashion in comparison to the much slower burn-in of fission product lanthanides in a fresh fuel fabricated with clean uranium. Controlling FCCI in this system is even more important due to the potentially reduced lifetime of the fuel [4].

The current study is the initial investigation using Sn as a fuel additive. There are multiple reports of Sn-U interactions, due to Sn being a minor component in Zr-based cladding [18][19][20] and also for the molten Sn process for reprocessing oxide and carbide fuels [21][22]. Tin was previously identified as a potential fuel additive [7], but to date has not been investigated as such. The current study examines U-Zr alloys with Sn and with both Sn and a mix of lanthanides. The composition and ratio of lanthanides are based on elemental analysis of irradiated U-10Zr EBR-II fuel pins [7], with the four most prevalent lanthanides included in the mix. The ratio obtained from EBR-II fuel is 53Nd-25Ce-16Pr-6La, in wt %. In the case of recycled fuel, the starting concentrations of lanthanides will have a slightly different elemental ratio; the ratio of lanthanides in recycled fuel will be modified slightly from their fission product yields by the separation factors in the pyrometallurgical process.

Pure Sn has a melting point (232°C) roughly 400°C below operating fuel temperatures, around 650°C. Free Sn could be highly detrimental to the fuel, with respect to possible unknown fission product transport issues or to possible liquid metal embrittlement of the cladding. Ruling out these concerns, along with investigating the as-cast and annealed microstructures is the motivation for this out-of-pile, separate-effects testing reported here.

2.3 Experimental Methods

Two alloys were cast, U-10Zr-4.3Sn wt% (71.2U-21.7Zr-7.2Sn at%) and U-10Zr-4.3Sn-4.7Ln (65.4U-21.1Zr-7.0Sn-6.5Ln at%), where Ln = 53Nd-25Ce-16Pr-6La wt% (52.3Nd-25.4Ce-16.2Pr-6.1La at%). All materials, except uranium, were obtained from Alfa Aesar and used as received. The lanthanides were obtained as rods, packaged in mylar under argon. Uranium was cleaned by submersion in nitric acid, followed by a water wash, then an ethanol wash.

All casting operations were carried out in an arc-melter within an argon atmosphere glovebox with high purity argon as a cover gas. After each addition step, the resulting button was flipped and re-melted 3 times to ensure homogeneity. To prepare U-10Zr-4.3Sn, the appropriate amount of Sn, Zr, and U were arc melted together in two steps. A button was prepared of U-Zr, followed by addition of Sn. To prepare 53Nd-25Ce-16Pr-6La, the appropriate amount of each lanthanide was arc melted together in one step. To prepare U-10Zr-4.3Sn-4.7Ln, the appropriate amount of the Ln alloy was added to a button of U-Zr-Sn, prepared as described for U-10Zr-4.3Sn. The buttons were cast into 5mm diameter pins.

Approximately 4mm from each pin was cut for annealing. The samples were wrapped in Ta foil, then sealed in quartz tubes under vacuum. The quartz tube was placed in a furnace at 650°C for 500 hours. After the heat treatment, the samples were quenched in water. The samples were cut to expose a fresh surface for analysis.

Scanning electron microscopy (SEM) was performed on a section of pin from each alloy for both as-cast and annealed. The samples were mounted in a 31.8 mm diameter phenolic metallographic (met) mount filled with epoxy. Samples were polished by grinding the surfaces flat with SiC grinding paper followed by polishing with polycrystalline diamond suspensions, starting with 9 µm, then 3 µm, and finally 1 µm. The polished samples were analyzed with a sputtered coating of approximately 15nm carbon to control charging of the metallographic mount.

The instrument used for this analysis was a JSM-7600f scanning electron microscope (SEM) manufactured by the Japan Electron Optics Laboratory (JEOL). The JSM-7600f is a hot field emission SEM equipped with an Oxford Instruments X-Max 20 silicon drift energy dispersive X-ray spectrometer (EDS). The X-ray spectrometer is controlled by Oxford INCA software (v. 4.15, part of the Oxford Microanalysis Suite Issue 18d + SP 4), which also provides image acquisition capabilities.

The SEM was operated at an accelerating voltage of 20kV and a nominal beam current of approximately 84nA (which can vary somewhat with column conditions) for these analyses. Prior to analysis, X-ray detector response was verified using a copper target. All of the X-ray spectra were accumulated for 75 live seconds. Spectra were collected over the energy range 0 – 20keV, which covers characteristic X-ray energies from all analytes.

Spectra were quantified using so-called “standardless” analysis, which uses a stored library of reference spectra to quantify unknown spectra rather than physical standards. This method is generally accurate to the 0.1 to 0.5 wt/wt% range, depending on sample and microscope (observation) conditions.

Phase transformation temperatures for U-10Zr-4Sn were measured using a Netzsch DSC 404C Differential Scanning Calorimeter (DSC). The sample was held in an alumina lined Pt-Rh crucible, with ultra-high purity argon as the cover gas at a flow rate of 50 mL/min after passing it through an Oxy-gon OG-120M oxygen gettering furnace. Oxygen impurity levels were in the sub ppb range based on the measured performance of the gettering furnace. The DSC was programmed to ramp to the target temperature of 1500°C at a rate of 10°C/min, holding at temperature for 10 minutes, then cooling to room temperature (also at 10°C/min).

2.4 Results and Discussion

Tin has a low melting point (231.9°C), but a high boiling point (2,603°C) with a relatively low vapor pressure at fuel processing and operating temperatures. There were no difficulties casting buttons and pins with Sn, and no apparent loss while casting. Multiple intermetallic compounds are possible between Sn with Zr and U, thus there is no loss of Sn, and should be no free Sn in the alloy.

Throughout this manuscript, specific phases are discussed. Phases in a U-Zr alloy, α-U and δ phase, have been characterized and are known. [23] Phases including Sn and/or lanthanides are inferred from EDS results. Crystallography is underway to confirm the phases, but is not included in this study.

2.4.1 U-10Zr-4.3Sn

Alloy U-10Zr-4.3Sn (wt%) represents a possible advanced fresh fuel alloy composition. The concentration of Sn was chosen based on a previous investigation using Pd as a fuel additive. [7] In that study, the highest Pd content, 3.86 wt%, was chosen to bind the lanthanides produced at roughly 20% burnup in a 1:1 compound. This concentration was used for Sn to keep continuity in the ongoing fuel additive research at Idaho National Laboratory.

SEM images, using backscattered electrons (BSE), of as-cast U-10Zr-4.3Sn are shown in Figure 2-1a and 2-1b. The outer region of the pin cross-section is shown in Figure 2-1a. The triangular dendritic structures were found to a depth of roughly 500 μm. At greater depths, the hexagonal structures shown in Figure 2-1b are the only remaining precipitates. The hexagonal precipitates and the triangular dendrites, shown in Figure 2-1a, are shown with a higher magnification in Figure 2-2, with accompanying EDS data listed in Table 2-1. A higher magnification view from Figure-1b, showing the hexagonal precipitates, is shown in Figure 2-3, with EDS data listed in Table 2-2.

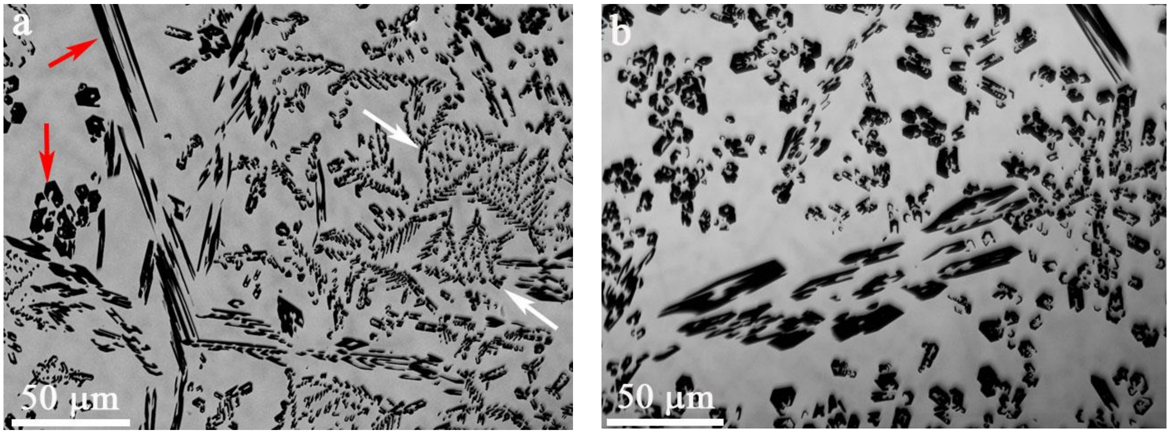

Figure 2-1. SEM BSE image for as-cast U-10Zr-4.3Sn. a. outer region of pin showing both hexagonal (red arrows) and triangular dendritic (white arrows) precipitates; b. central region of pin showing only hexagonal precipitates.

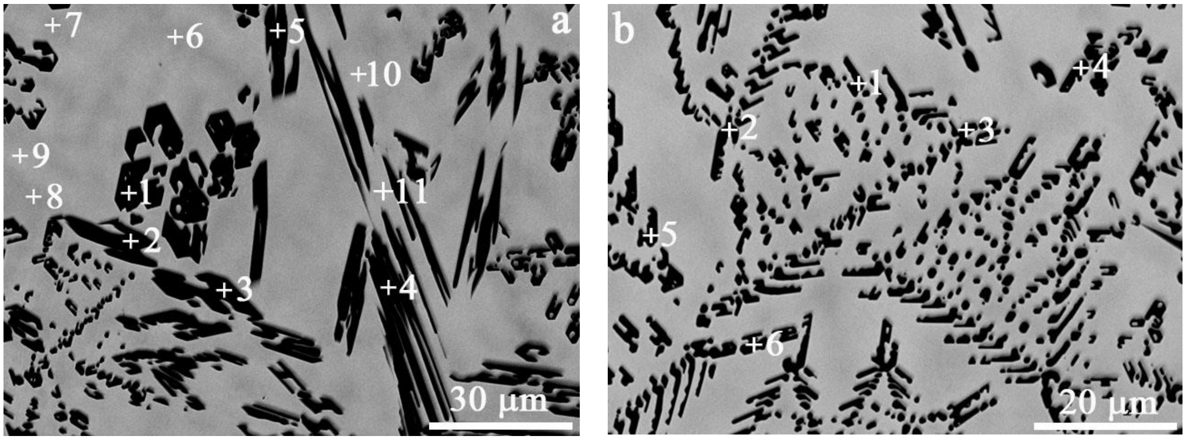

Figure 2-2. Higher magnification views of the image shown in Figure 2-1a. a. hexagonal precipitates, b. triangular dendrites. EDS data listed in Table 2-1.

Table 2-1. EDS data for points shown in Figure 2-2. Values in atomic %.

	U	Zr	Sn
Figure 2-2a			
1	1.9	61.5	36.6
2	2.8	61.1	36.1
3	2.4	61.1	36.5
4	2.9	61.2	35.9
5	2.3	61.2	36.5
6	80.8	17.8	1.4
7	81.5	17.0	1.5
8	81.6	16.7	1.7
9	88.7	10.1	1.2
10	88.2	10.7	1.1
11	87.4	11.3	1.4
Figure 2-2b			
1	10.1	56.6	33.3
2	10.6	57.1	32.3
3	9.6	57.3	33.1
4	9.3	57.4	33.3
5	6.3	59.5	34.3
6	8.2	58.1	33.6

The Zr/Sn ratio in the black precipitates varies only slightly for each set of data. The average ratio for the points shown in Figure 2-2a is 1.68, for Figure 2-2b it is 1.73, and for Figure 2-3 it is 1.62. These ratios are all practically the same, within experimental error for EDS. The data for Figure 2-2b is likely less reliable. Due to the small size of the precipitates, a significant amount of the surrounding matrix (in Figure 2-2b) was detected during analysis.

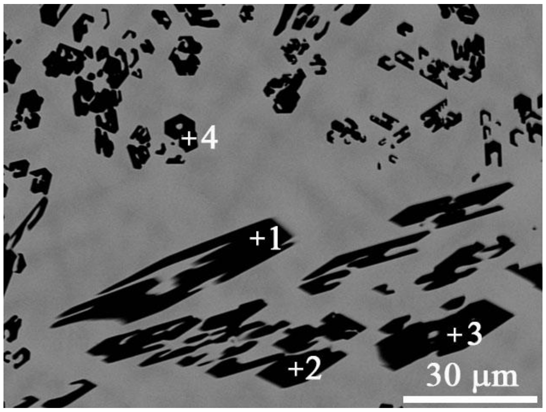

Figure 2-3. Higher magnification view of the image shown in Figure 2-1b. EDS data listed in Table 2-2.

Table 2-2. EDS data for points shown in Figure 2-3. Values in atomic %.

	U	**Zr**	**Sn**
1	1.9	60.6	37.5
2	2.0	60.5	37.5
3	2.2	60.3	37.6
4	4.0	59.7	36.3

The binary phase diagram for the Zr-Sn system is shown in Figure 2-4 [24]. For the Zr-Sn ratios that were observed (Tables 2-1 and 2-2), the relevant region is at a Sn concentration of 40 at %, with a composition of Zr_5Sn_3. This ratio appears consistent across the entire pin, although the precipitates at the outer region of the pin have a dendritic morphology compared to the hexagonal morphology predominating at the inner region of the pin. The hexagonal structure is visible in some of the larger areas at the points of the triangles, indicating the composition is likely the same throughout the precipitates. The visual differences are likely due to the rapid cooling at the periphery during the pin casting process, with the inner region cooling slower, allowing formation of the larger hexagonal structures.

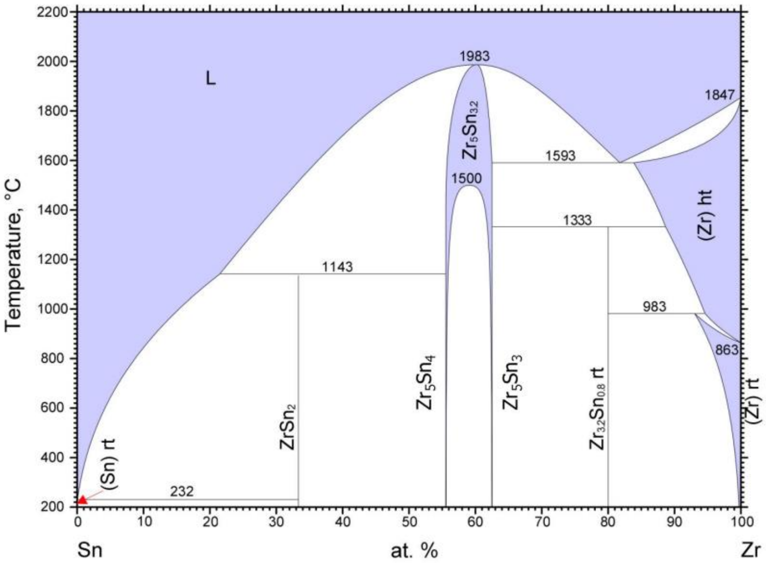

Figure 2-4. Zr-Sn binary phase diagram [24], with added annotations for Zr_5Sn_4 and Zr_5Sn_3.

The starting concentration in the alloy, 71.2U-21.7Zr-7.2Sn at%, corresponds to a normalized Zr-Sn ratio of 75.2Zr-24.8Sn at%. This ratio is not observed in the precipitates, though, due to some Zr remaining in the uranium matrix. EDS data listed for the points shown in Figures 2-2a indicates the Zr content varies from roughly 10.1 to 17.8 at% in the matrix. As observed in U-Zr alloys [25], there is a differentiation in the matrix, with lighter (low Zr) and darker (higher Zr) regions visible.

Figure 2-5 shows images for U-10Zr-4.3Sn after annealing at 650°C for 500 hours. Figure 2-5b is an increased magnification view of the inner pin region shown in Figure 2-5a, with EDS analysis points shown. EDS data is listed in Table 2-3. There is no noticeable change in the precipitates, along the outer region of the pin (not shown) or the inner region. The Zr/Sn ratio is roughly 1.68, indicating the composition is still Zr_5Sn_3. A change in either the appearance or composition of the precipitates was not expected given the high decomposition temperature for Zr_5Sn_3.

Upon annealing the matrix resolves into α-U and δ phase, evident by the light and dark regions present in the matrix. The U content in the δ phase, Table 2-3, points 1-3, is high, but the analyzed points are very small in size, so U from the surrounding α–U regions is included in the analysis. The amount of δ phase present is small, due to Zr being consumed in the Zr-Sn precipitates.

There is a small amount of Sn present in the U-rich regions before and after annealing (Table 2-1, points 9-11, and Table 2-3, points 4-6). The amount of Sn is very small, though, less than 2 at%. U_5Sn_4 is a possible intermetallic in the U-Sn system [26], but there is no EDS evidence to suggest an intermetallic is forming. Based on these observations, Sn clearly has a preference to bind to Zr in this fresh fuel composition. The small amount of Sn present in the U-rich regions could possibly arise from slightly enhanced solid solubility of Sn that derives from the presence of Zr in these regions.

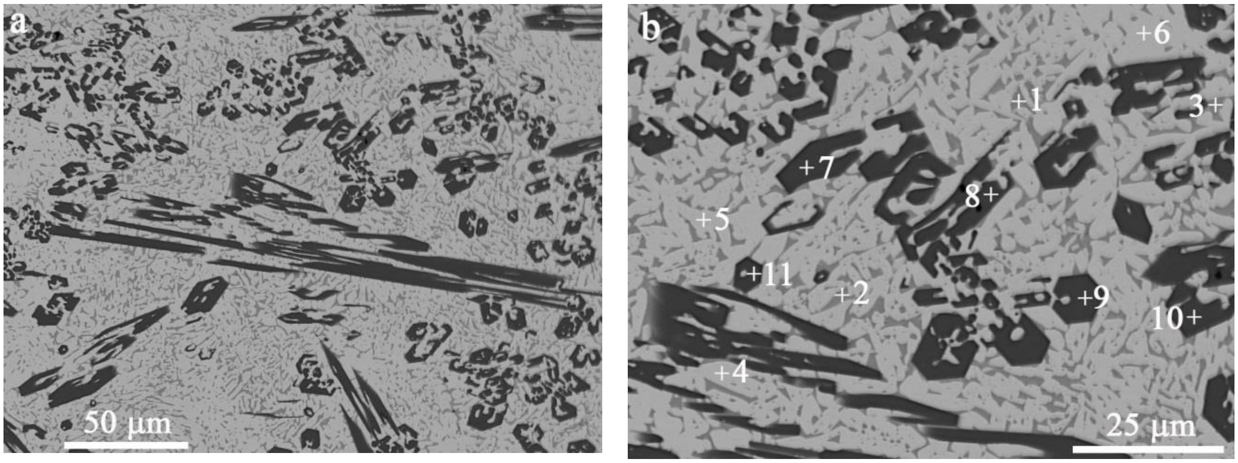

Figure 2-5. SEM BSE images for annealed U-10Zr-4Sn. a. central region of pin; b. higher magnification view showing EDS points. EDS data listed in Table 2-3.

Table 2-3. EDS data for points shown in Figure 2-5b. Values in atomic %.

	U	Zr	Sn
1	38.7	60.8	0.5
2	39.1	60.1	0.7
3	39.3	60.5	0.3
4	97.8	0.8	1.4
5	97.6	1.2	1.2

Table 2-3. (continued).

	U	Zr	Sn
6	96.9	1.3	1.8
7	2.0	61.5	36.6
8	1.9	61.6	36.5
9	2.0	61.5	36.5
10	1.9	61.3	36.8
11	2.1	61.2	36.7

The measured Zr/Sn ratio is very close to Zr_5Sn_3, with the small differences likely due to limitations in the method. The starting concentration of Sn in the alloy is 7.2 at%, which will require 12.0 at% Zr to completely consume the available Sn in forming Zr_5Sn_3, leaving 10.5 at% Zr for the matrix. For this concentration of Zr, the solidus temperature should be roughly 1175°C, based on the U-Zr phase diagram [27].

Differential Scanning Calorimetry (DSC) results for the as-cast alloy, shown in Figure 2-6, indicate a solidus of 1192°C which corresponds closely to the solidus estimated from the EDS results. DSC data are summarized in Table 2-4. Given this solidus temperature, the actual concentration of Zr in the matrix should be between 12 and 12.5 at%. This small difference in composition (10.5 compared to 12 at%) is close to the error inherent in EDS, and could also be accounted for in terms of the small amount of Sn observed by SEM in the matrix. A small amount of Sn in the matrix would yield less Zr_5Sn_3, and therefore a slightly higher Zr content available in the matrix to produce a slightly higher solidus as observed in the DSC. This simple analysis is based on the starting weights of the materials, though, and does not take into account possible losses or in homogeneities that can arise while arc melting. While high precision wet chemical analysis of the cast pins was not performed, the casting recipe and DSC results are reasonably consistent with each other.

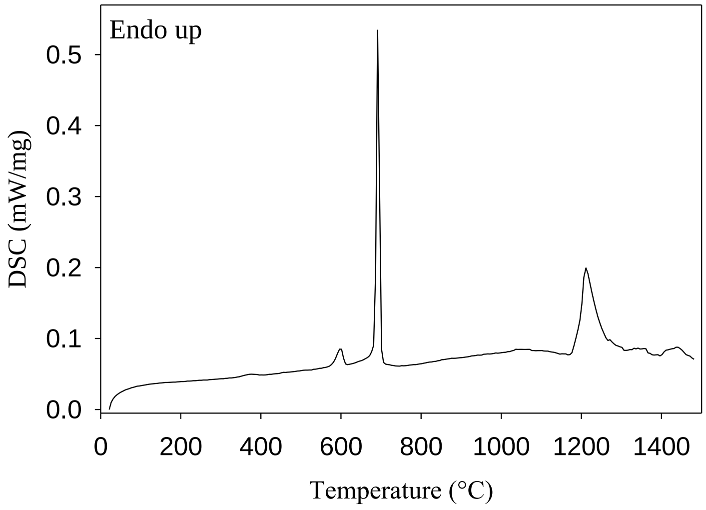

Figure 2-6. DSC curve for as-cast U-10Zr-4Sn.

Table 2-4. DSC data for as-cast U-10Zr-4Sn.

Peak Start (°C)	Peak (°C)	Peak End (°C)	Transition
578	599	610	$(\alpha,\delta)\rightarrow(\alpha,\gamma_2)$
685	693	700	$(\alpha,\gamma_2)\rightarrow(\alpha,\gamma_1)$
1192	1211	1256	liquidus

The DSC curve is essentially the same as for a U-Zr alloy, since the Zr-Sn precipitates decompose very close to, or above, the maximum temperature for this DSC. The upper temperature region (>1400°C), above the solidus/liquidus peak, may be the initial decomposition of Zr_5Sn_3. Given that the measured DSC curve does not include contributions from Sn, the peak assignments are based on the U-Zr phase diagram [27][28].

The decrease in Zr content in the matrix due to precipitate formation is important in the performance of a metallic fuel. The primary reason for adding Zr is to raise the solidus/liquidus temperatures, especially in the case of a transmutation fuel, due to the significant drop in solidus temperature upon addition of Pu [29]. To negate this drop, extra Zr will have to be added. Additions of non-fissile material to the fuel need to be kept at a minimum, though, in order to maintain fuel performance. The other fuel additives investigated, Pd and In, also deplete Zr from the matrix. Pd forms $PdZr_2$ [7], while the reported Zr/In ratio of 2.5 corresponds to Zr_5In_2 [14]. Of the additives investigated to date, Sn has the most advantageous Zr/Sn ratio (1.67), depleting the least amount of Zr from the matrix.

Surprisingly, no α-Zr precipitates were found in the alloy, before or after annealing, although it is commonly found in U-Zr alloys, with or without additives [7][30]. Based on the phase diagram [27], it should not exist, and is believed to be caused by small amounts of oxygen having a stabilizing effect on α-Zr [30]. The same U and Zr feedstocks and polishing procedures were used as for previous U-alloys and U-Zr-Pd alloys, all of which contained α-Zr precipitates. This indicates the lack of α-Zr in the U-Zr-Sn alloy is not due to fabrication or sample preparation. Since no additional steps were taken to exclude oxygen, the small amounts of oxygen are still present, and are likely associated with the Zr-Sn precipitates.

In both the as-cast and annealed microstructures, no precipitates of isolated Sn were observed. While expected from the phase diagrams, this result is important and favorable to demonstrate, because of the low melting point of Sn, and the possibility of liquid-metal embrittlement of the cladding. In this U-Zr-Sn alloy, all of the Sn appears to be bound at these concentrations, even though a small amount (<2 at%) was dissolved in the α-U and δ phases in the annealed structure and in the light and dark regions of the as-cast alloy. Based on the phase diagrams [24][26], there is no solubility of Sn in U, and only a small solubility of Sn in Zr. The low concentration of Sn found could arise from a slight solubility of Sn in the fuel matrix, made favorable by the presence of dissolved Zr, or δ phase. The low concentration of Sn could also be an artifact of the spot size overlapping nearby Zr-Sn precipitates, or due to a small amount of overlap of the X-rays peaks used in the EDS analysis for Sn and U. Regardless, there is no evidence of any liquid behavior in the annealed sample, ruling out the possibility of free Sn. Furthermore, any enhanced solid solubility of Sn in the fuel matrix that may arise from the presence of Zr indicates a lesser activity of Sn, i.e., its stabilization in the fuel matrix.

2.4.2 U-10Zr-4.3Sn-4.7Ln

The composition U-10Zr-4.3Sn-4.7Ln (65.4U-21.1Zr-7.0Sn-6.5Ln at%) was chosen to represent a fuel after roughly 16% burnup, similar to previous work with U-Zr-Pd alloys [7], based on lanthanide composition. This composition has a small molar excess of Sn, thus no free lanthanides should be present.

The microstructure of the alloy changes significantly upon addition of lanthanides, as shown in Figure 2-7. A representative large area BSE image of the alloy is shown in Figure 2-7a. Figure 2-7b shows a large precipitate within this alloy, with EDS analysis listed in Table 2-5. The alloy shows several distinct features. There are rough, random shaped precipitates, round precipitates, and black precipitates that appear to be Zr_5Sn_3, as observed in U-10Zr-4.3Sn. There is a slight molar excess of Sn in the alloy, relative to lanthanide content (65.4U-21.1Zr-7.0Sn-6.5Ln at%), so the presence of some Zr_5Sn_3 was expected. The uranium matrix is similar to that observed in U-10Zr, with light and dark regions, as was also observed for the U-Zr-Sn alloy described in the previous section.

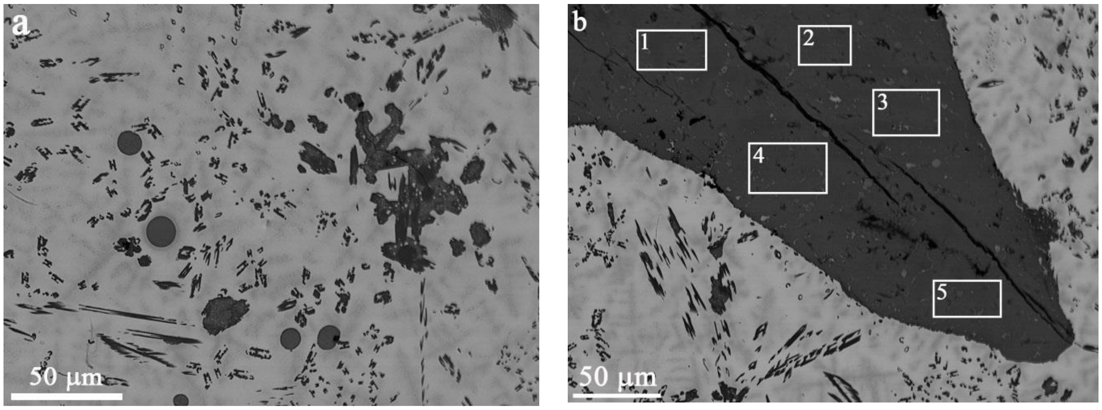

Figure 2-7. SEM BSE image for as-cast U-10Zr-4.3Sn-4.7Ln. a. representative region of pin; b. large precipitate. EDS data for b listed in Table 2-5.

Table 2-5. EDS data for areas shown in Figure 2-7b. Values in atomic %.

	U	Zr	Sn	Nd	Ce	Pr	La
1	2.0	15.5	32.1	26.1	12.2	8.5	3.6
2	2.1	14.7	32.3	26.2	12.5	8.4	3.8
3	1.8	11.5	34.6	27.3	12.5	8.5	3.8
4	2.0	13.7	32.9	26.4	12.6	8.5	3.9
5	2.0	14.1	33.0	26.1	12.5	8.4	4.0

The sample slice that was cut and analyzed happened to contain the large precipitate region shown in Figure 2-7b. Other samples cut from the pin did not contain large precipitates. The precipitate extended roughly 2 mm into the pin, and was also present at the periphery. From the EDS data collected, the ratio of lanthanides to Sn is roughly 1.56, putting the composition between Ln_5Sn_3 and Ln_5Sn_4. Given that Nd is the largest component of the lanthanide mix, the densities for Nd_5Sn_3 and Nd_5Sn_4 will be used for this discussion. The density is 7.17 and 7.26 g/cm^3 for Nd_5Sn_3 and Nd_5Sn_4, respectively [31][32], which are significantly lower than the density for U metal, 19.1 g/cm^3. Due to this density difference, it is believed the alloy was completely mixed during arc melting, and the separation occurred during the pin casting process. This separation has been observed in other uranium-additive alloys upon addition of lanthanides [33]. This should not adversely affect the analysis, since the lanthanides are still uniformly spread throughout the alloy, just in lower concentrations than would be observed if the large precipitate had not separated from the alloy. This result is unlikely to occur in a reactor, though, since the lanthanides will burn-in slowly. This result might be a concern when fuel is fabricated with recycled uranium, because a small amount of lanthanides could separate with Sn, causing an uneven distribution of fissile material throughout the fuel. In recycled fuel, however, with lanthanides present in minor quantities, the added Sn will be present in large excess, and the Sn should aid dispersal of the lanthanides, based on behavior of the U-Zr-Sn without lanthanides.

Increased magnification images from Figure 2-7a are shown in Figures 2-8a and 2-8b, with EDS data listed in Table 2-6. Analysis of the matrix region (points 1-3 in Figure 2-8a, Table 2-6) indicates the dark matrix regions contain significantly more Zr (>30 at%) than found in U-10Zr-4.3Sn (~17 at%). The light matrix regions are roughly the same between the alloys. The alloy was fabricated by adding lanthanides to a pre-alloy of U-Zr-Sn, thus the pre-alloy might be expected to look very similar to U-10Zr-4.3Sn, i.e., with a significant amount of Zr tied up in Zr-Sn precipitates. The increase in Zr content in the dark matrix regions clearly indicates Zr is being released back into the matrix, and that Sn has a preference to bind lanthanides.

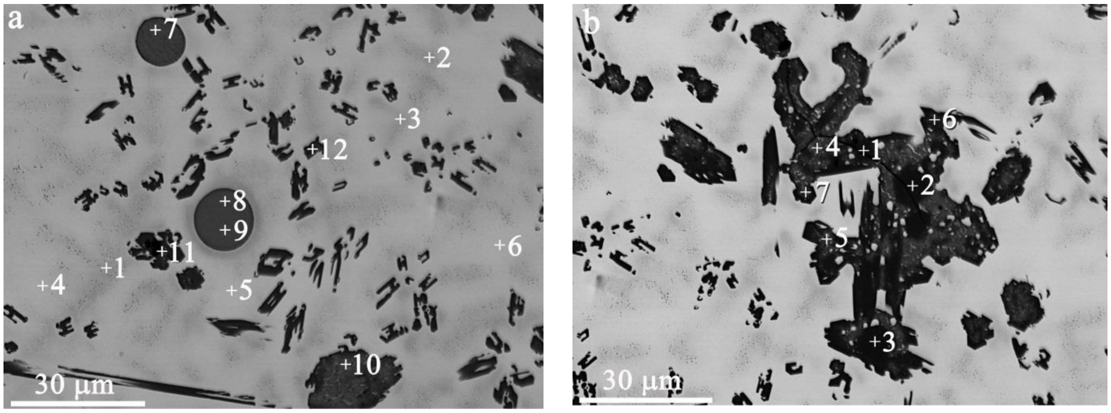

Figure 2-8. a. and b. higher magnification view of the image shown in Figure 2-7a. EDS data listed in Table 2-6.

Table 2-6. EDS data for points shown in Figure 2-8. Values in atomic %.

	U	Zr	Sn	Nd	Ce	Pr	La
Figure 2-8a							
1	65.1	32.9	1.6	0.0	0.2	0.2	0.0
2	61.9	35.5	2.3	0.0	0.3	0.0	0.0
3	67.5	30.3	1.5	0.0	0.4	0.2	0.1
4	86.7	11.5	1.2	0.0	0.2	0.4	0.0
5	88.7	9.4	1.0	0.0	0.5	0.5	0.0
6	89.2	9.0	1.3	0.0	0.3	0.2	0.0
7	2.6	15.9	35.0	22.5	13.4	7.7	2.9
8	1.5	11.8	36.5	23.4	15.6	8.4	2.9
9	1.6	12.0	36.8	23.0	15.5	8.3	2.8
10	4.2	21.5	33.3	20.0	12.0	6.8	2.2
11	1.3	63.4	32.4	2.0	0.4	0.5	0.0
12	3.7	52.9	35.6	4.2	1.8	1.3	0.4
Figure 2-8b							
1	1.7	59.9	36.6	1.0	0.3	0.3	0.2
2	1.8	61.5	36.5	0.0	0.1	0.0	0.1
3	2.1	61.3	36.5	0.0	0.0	0.0	0.0
4	6.0	15.9	34.2	21.8	10.9	7.2	4.0
5	10.3	15.9	31.5	21.3	10.4	7.0	3.7
6	2.3	23.2	36.1	19.5	9.6	6.0	3.3
7	4.8	22.7	32.8	20.1	9.7	6.6	3.4

The round precipitates (points 7–9 in Figure 2-8a, Table 2-6) are very similar in composition to the large precipitate shown in Figure 2-7b. The rough, random shaped precipitates are a mix of Zr, Sn, and lanthanides, although the composition varies from Zr_5Sn_3 to Ln_5Sn_3 with variable amounts of Zr. These precipitates appear to be frozen during the reaction converting Zr_5Sn_3 to Ln_5Sn_3. The process may be kinetically slow enough to not finish during arc melting, as the SEM results for the annealed sample, described below, indicate.

Figure 2-9a and 2-9b show representative images for U-10Zr-4.3Sn-4.7Ln after annealing at 650°C for 500 hours. Two types of precipitates remain after annealing, the Zr-Sn precipitates and the round Sn-Ln precipitates. The rough, random shaped precipitates shown in Figure 2-8b are no longer present, indicating the conversion of Zr_5Sn_3 to Ln_5Sn_3 is complete, or at least closer to completion. Higher magnification images with EDS points are shown in Figure 2-10. An expanded region from Figure 2-9a is shown in Figure 2-10a, while Figure 2-10b is an expanded region from Figure 2-9b. The matrix region (points –6 in Figure 2-10a, Table 2-7) shows the separation of the matrix into α-U and δ phase, as observed in Figure 2-5 for U-0Zr-4.3Sn. The alloy with Ln has substantially more δ phase (visual observation), though, due to Zr no longer being consumed in Zr-Sn precipitates. There are still Zr-Sn precipitates present, though (points 7–9, Figure 2-10a, Table 2-7), due to the small molar excess of Sn (in relation to the lanthanides).

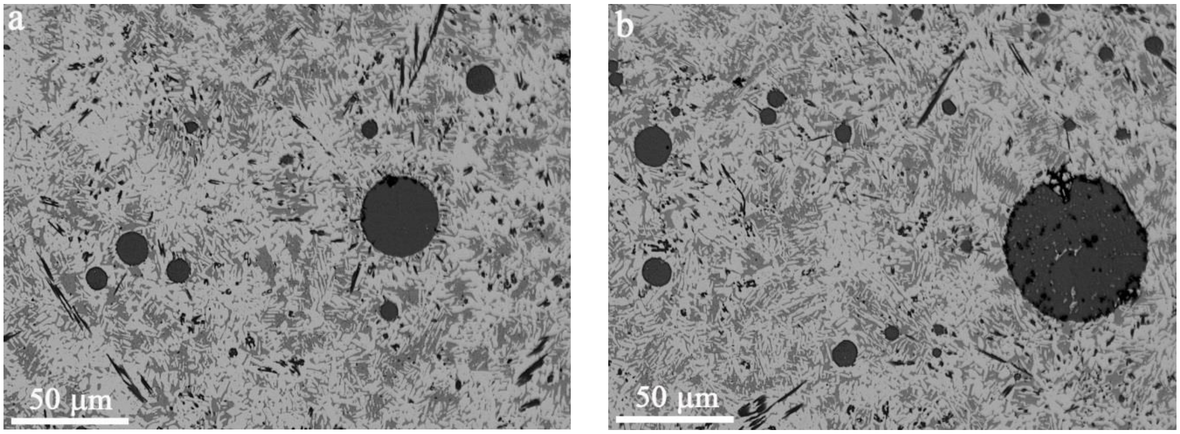

Figure 2-9. a. and b. SEM BSE images of annealed U-10Zr-4.3Sn-4.7Ln.

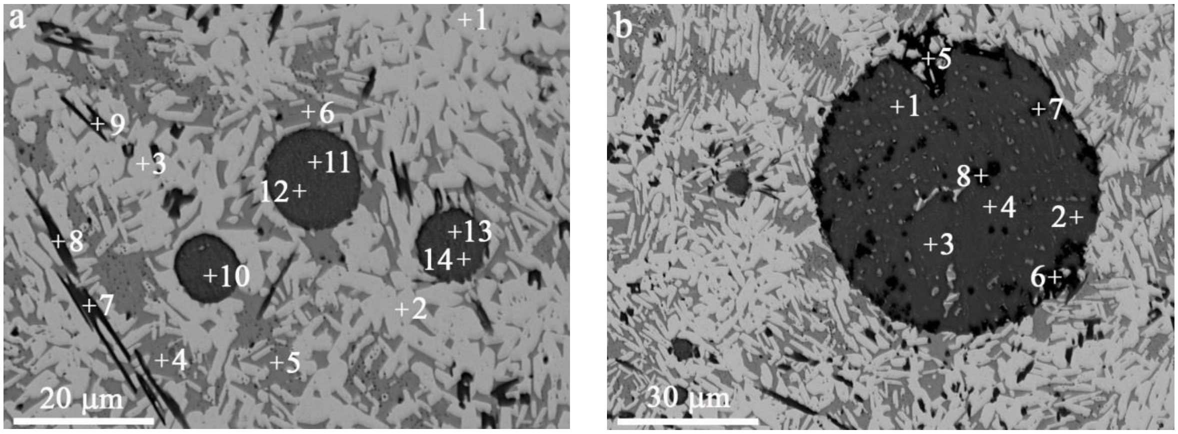

Figure 2-10. a. higher magnification region from image shown in Figure 2-9a; b. higher magnification region from image shown in Figure 2-9b. EDS data listed in Table 2-7.

Table 2-7. EDS data for points shown in Figure 2-10. Values in atomic %.

	U	Zr	Sn	Nd	Ce	Pr	La
Figure 2-10a							
1	96.9	0.7	1.5	0.0	0.2	0.6	0.0
2	97.9	0.6	1.2	0.0	0.1	0.2	0.0
3	97.3	0.7	1.7	0.0	0.0	0.3	0.0
4	38.3	60.0	0.8	0.0	0.5	0.2	0.3
5	37.5	59.9	2.0	0.0	0.4	0.1	0.1
6	38.5	59.8	1.1	0.0	0.3	0.1	0.1
7	3.8	59.4	34.4	1.6	0.5	0.3	0.0
8	5.9	58.7	32.9	1.6	0.4	0.4	0.0
9	6.0	58.5	32.7	1.4	0.7	0.6	0.1
10	1.9	11.5	36.2	22.0	18.4	8.3	1.8
11	1.8	15.1	36.2	21.6	15.7	7.7	1.9
12	1.9	15.9	35.5	21.7	15.5	7.7	1.9
13	2.2	15.0	36.3	21.4	15.7	7.7	1.7
14	2.2	14.9	35.7	21.1	16.5	7.8	1.7
Figure 2-10b							
1	1.6	9.5	36.8	24.6	16.1	8.6	2.7
2	2.4	11.3	36.3	24.7	14.6	8.3	2.5
3	1.6	10.0	37.1	25.8	14.6	8.8	2.1
4	1.9	10.4	37.0	25.8	14.2	8.5	2.2
5	3.5	95.4	0.6	0.1	0.2	0.1	0.1
6	1.6	96.0	1.2	0.7	0.3	0.3	0.0
7	1.6	89.5	4.5	2.0	1.5	0.7	0.2
8	1.4	93.2	2.9	1.3	0.7	0.5	0.1

In general, the smaller Sn-Ln precipitates, such as those shown in Figure 2-10a, are uniform in composition throughout, although a thin layer of Zr can be found around the periphery of the precipitate. EDS points 10–14 in Figure 2-10a and Table 2-7 are very consistent for 3 separate precipitates. The only measurable change is the variation in Zr and Ce. When Ce is slightly higher, Zr is slightly lower, as observed in point 10 in Figure 2-10a, Table 2-7, and point 1 in Figure 2-10b, Table 2-7. In all of the precipitates analyzed, roughly 10–15 at% Zr was present. Using points 10–14 in Figure 2-10a and points 1–4 in Figure 2-10b, Table 2-7, the Ln/Sn average ratio is 1.39, placing the composition between Ln_5Sn_4 and Ln_5Sn_3, but closer to Ln_5Sn_4. Including Zr with the lanthanides, the Ln + Zr/Sn average ratio is 1.70, very close to the Ln/Sn ratio of 1.67 for Ln_5Sn_3. The crystal structure for Zr_5Sn_3 is $P6_3$/mcm, prototype Mn_5Si_3. This is identical to the crystal structure for Nd5Sn3, and the high temperature crystal structures for Ce5Sn3, Pr5Sn3, and La_5Sn_3. [34][35][36] Zr may be substituting into the lattice, replacing a small number of lanthanide atoms to create $(Ln + Zr)_5Sn_3$. The transition from low temperature to high temperature structure, with a small amount of variation based on the lanthanide, occurs in the range of 400°C, so is easily accessible when arc melting during alloy fabrication. More importantly, this is below the operating temperature of a fast reactor, so if this substitution is taking place, it can occur under reactor conditions.

The role of Zr in the Ln-Sn precipitates is uncertain, but whether Zr is participating in the crystal structure or simply dissolved, the structures are lanthanide rich, even with a small molar excess of Sn in the alloy. The excess Sn is found primarily in Zr_5Sn_3 precipitates, with a small amount in the U-Zr matrix. Due to the favorable Ln/Sn molar ratio in the precipitates, there is a reserve of Sn available for higher Ln loadings. Based on the current alloy, 65.4U-21.1Zr-7.0Sn-6.5Ln at%, this amount of Sn could be expected to bind 11.6 at% Ln, without participation by Zr. The maximum Ln loading drops to 9.7 at% if Zr is included in the crystal structure. Using the lanthanide concentrations reported for 8% and 16% burn-up (2.8 and 5.6 at%, respectively) [3] and extrapolating, the current loading of Sn could bind all the lanthanides produced at a maximum burn-up of 33% (corresponding to 11.6 at% Ln).

Large precipitates, such as that shown in Figure 2-10b, have a mottled appearance. EDS analysis indicates the majority of the precipitate is Sn-Ln, while the black spots are Zr. The small white inclusions are likely trapped α-U. The concentration of Sn is roughly the same as for the small precipitates shown in Figure 2-10a, but the Zr content is slightly lower and the Ln content is slightly higher for each Ln constituent. The Ln+Zr/Sn ratio (average of points 1–4 in Figure 2-10b, Table 2-7) is 1.67, indicating the structure is still $(Ln+Zr)_5Sn_3$.

There is no direct correlation between the rough precipitate shown in Figure 2-8b and the precipitate shown in Figure 2-10b, due to the as-cast and annealed analysis being performed on different sections of the pin. The large annealed precipitate likely came from a similar precipitate as that shown in Figure 2-8b, though, based on physical appearance. The Zr and U inclusions could be trapped, or the sample may not have been annealed for a long enough time to allow migration out of the precipitate. A Zr rind is present, as it is in the 3 smaller precipitates shown in Figure 2-10a. Small Zr precipitates are present around the large Ln precipitates, separate from the precipitate but close, but not throughout the bulk of the alloy. It appears that excess Zr is migrating out of the precipitates and slowly dissolving into the U-Zr matrix. As previously discussed, the conversion from Zr_5Sn_3 to Ln_5Sn_3, or some variation of $(Ln + Zr)_5Sn_3$, must be kinetically slow, thus annealing for 500 hours was not sufficient for the process to finish.

2.5 Conclusions

The data presented indicates Sn is a viable and possibly very good additive to control FCCI in a metallic fuel. Sn has been investigated as a small component in fuel cladding, but this is the first investigation of Sn as an additive to the fuel. The following conclusions can be drawn from the data presented:

- There is a clear preference for Sn to bind the lanthanides, releasing Zr back into the U-Zr matrix. The alloy containing lanthanides was fabricated starting with a U-Zr-Sn pre-alloy and adding lanthanides, thus the Zr-Sn precipitates had to break apart in order to form the Ln-Sn precipitates.
- In the current investigation, there was a small molar excess of Sn over the lanthanides, but the thermodynamically most stable Sn-Ln intermetallics formed, Ln_5Sn_4 and Ln_5Sn_3, even though the lanthanides were the limiting reagent. Further work is needed to determine if Ln_5Sn_3 (or $(Ln+Zr)_5Sn_3$) is the predominant structure, or if there is a mix of intermetallics. That work is in progress, but regardless of the exact compound being formed, they are both Ln-rich. The significant consequence is that less Sn is required to bind the lanthanides than if a 1/1 compound or a Sn-rich compound was formed.
- When using a fuel additive, extra Zr will be needed to negate the removal of Zr from the matrix. Zr_5Sn_3 is the primary intermetallic being formed, possibly with some Zr_5Sn_4. Both compounds are Zr-rich, but the ratio of Zr to Sn is less than 2. Other additives, specifically In [6] and Pd [3], that have been investigated both have a Zr/additive ratio of 2 or more. The Zr/Pd ratio is 2, while the Zr/In ratio is 2.5, thus depleting a large amount of Zr from the U-Zr matrix. Of the 3 additives investigated, Sn will have the least impact on the fuel solidus and liquidus.

- Based on the above observations, Sn may be expected to outperform Pd, which outperforms Indium. Also, Sn is more abundant than In and Pd in the earth’s crust, so less expensive for large scale fabrication. Sn is therefore recommended for irradiation testing.

3. INVESTIGATION OF TIN AS A FUEL ADDITIVE TO CONTROL FCCI

The full reference for the following manuscript is: M.T. Benson, J.A. King, R.D. Mariani, "Investigation of tin as a fuel additive to control FCCI," Proceedings of The Minerals, Metals & Materials Society (TMS), Vol. F12, **2018**, 695–702.

3.1 Abstract

One method to control fuel-cladding chemical interaction (FCCI) in metallic fuel is through the use of an additive that inhibits FCCI. A primary cause of FCCI is the lanthanide fission products moving to the fuel periphery and interacting with the cladding. This interaction will lead to wastage of the cladding and eventually to a cladding breach. Tin is being investigated as a potential additive to control FCCI by reacting with the fission product lanthanides. The current study is a scanning electron microscopy (SEM) characterization of a diffusion couple between U-10Zr-4.3Sn (wt%) and the 4 most abundant lanthanide fission products. We find as the lanthanides move into the fuel, they are reacting with and breaking down the Zr_5Sn_3 precipitates that formed during fresh fuel fabrication. This reaction produced Ln-Sn precipitates and δ phase (UZr_2), which is conducive to normal fuel operation and increased burnups.

3.2 Introduction

Fuel-cladding chemical interaction (FCCI) occurs when the nuclear fuel or fission products react with the cladding material. A major cause of FCCI in metallic fuels during irradiation is fission product lanthanides (Ln), which tend to migrate to the fuel periphery, coming in contact with the cladding. The result of this interaction is degradation of the cladding, and will eventually lead to rupture of the fuel assembly [1][2]. In order to extend fuel life, while making the fuel less likely to have a cladding breach, some method of controlling FCCI is needed. Several methods are being investigated to decrease or prevent FCCI, such as barrier foils, coatings, and additive materials [5][6][7][10][14]. In the additive approach, considering ways to bind lanthanides as stable intermetallics, criteria were developed that identified a set of elements that could be promising additives [7]. From this list, Pd [7][16][17], In [14], and Sn [10] have been investigated, and each have shown promise as a fuel additive.

Ordinarily, the lanthanides can burn-in as fission products; however, in the case of recycled fuel, they will be present as minor impurities in recycled, as-fabricated fuel [3]. In this case, as soon as the fuel contacts the cladding due to swelling, at roughly 1-2% burnup, there are already lanthanide impurities in the recycled fuel available to initiate FCCI. This early form of FCCI in a recycled fuel will occur in accelerated fashion in comparison to the much slower burn-in of fission product lanthanides in a fresh fuel fabricated with clean uranium. Controlling FCCI in this system is even more important due to the potentially reduced lifetime of the fuel [4].

The diffusion couple described in this paper is a continuation of previous work [10] using Sn as a minor additive to control FCCI. In that report, the as-cast and annealed microstructures were investigated, with and without lanthanides present. That characterization was necessary in order to determine the structure of a fresh fuel, and is a good initial check of the efficacy of a particular additive, in terms of chemical bonding of the additive to the lanthanides over Zr. The drawback with this characterization is the high temperatures present in the arc melter during fabrication, which may generate high temperature phases that would not be present at reactor temperatures. A diffusion couple, performed at reactor temperature (650°C), between the fresh fuel and the lanthanides provides a more realistic out-of-pile test of the additive-lanthanide interactions.

3.3 Experimental Methods

The alloys, U-10Zr-4.3Sn wt% (71.2U-21.7Zr-7.2Sn at%) and 53Nd-25Ce-16Pr-6La wt% (52.3Nd-25.4Ce-16.2Pr-6.1La at%) were fabricated as previously reported [3], and cast into 5mm diameter pins. All materials, except uranium, were obtained from Alfa Aesar and used as received. The lanthanides were obtained as rods, packaged in Mylar under argon. Uranium was cleaned by submersion in nitric acid, followed by a water wash, then an ethanol wash.

Approximately 3mm from each pin was cut for the diffusion couple. To prepare the samples for the diffusion couple, the surface was ground flat using SiC grinding paper, followed by polishing with polycrystalline diamond suspensions, starting with 9 µm, then 3 µm, and finally 1 µm. This was performed in air. The samples were transferred into an argon glovebox, and hand polished with polycrystalline diamond suspension, starting with 3 μm, then 1 μm, to remove any oxide layer. The samples were placed together, with polished surfaces in contact and surrounded by Ta foil, in a previously described diffusion couple jig [16]. The jig was tightened to 50 in lbs. The jig was removed from the glovebox and sealed in a quartz tube under vacuum. The tube was heated at 650°C for 504 hours. After the heat treatment, the diffusion couple was quenched in water, then removed from the diffusion couple jig for analysis.

The sample was mounted in a 31.8 mm diameter phenolic metallographic (met) mount filled with epoxy. The diffusion couple interface was exposed by grinding roughly half the diameter away with SiC grinding paper. The sample was then polished with polycrystalline diamond suspensions, starting with 9 µm, then 3 µm, and finally 1 µm. The polished sample was analyzed with a sputtered coating of approximately 15nm carbon to control charging of the met mount in the scanning electron microscope (SEM).

The instrument used for this analysis was a JSM-7600f SEM manufactured by the Japan Electron Optics Laboratory (JEOL). The JSM-7600f is a hot field emission SEM equipped with an Oxford Instruments X-Max 20 silicon drift energy dispersive X-ray spectrometer (EDS). The X-ray spectrometer is controlled by Oxford INCA software (v. 4.15, part of the Oxford Microanalysis Suite Issue 18d + SP 4), which also provides image acquisition capabilities.

The SEM was operated at an accelerating voltage of 20kV and a nominal beam current of approximately 84nA (which can vary somewhat with column conditions) for these analyses. Prior to analysis, X-ray detector response was verified using a copper target. All of the X-ray spectra were accumulated for 75 live seconds. Spectra were collected over the energy range 0 – 20keV, which covers characteristic X-ray energies from all analytes.

Spectra were quantified using so-called “standardless” analysis, which uses a stored library of reference spectra to quantify unknown spectra rather than physical standards. This method is generally accurate to the 0.1 to 0.5 wt/wt% range, depending on sample and microscope (observation) conditions.

3.4 Results and Discussion

Figure 3-1 shows representative images of the interface between U-10Zr-4.3Sn and the lanthanides. The locations of the higher magnification images shown in Figures 3-2 and 3-3 are indicated by the red rectangles. Several features are readily apparent in the large area scans. There is obvious penetration of the lanthanides into the fuel, with only a small amount of fuel moving into the lanthanides. The Zr rind, common to U-Zr fuels, may be hindering the fuel moving into the lanthanides. Also apparent is the different zones present in the fuel matrix, extending roughly 100 μm into the fuel. Each of these features is discussed in more detail below.

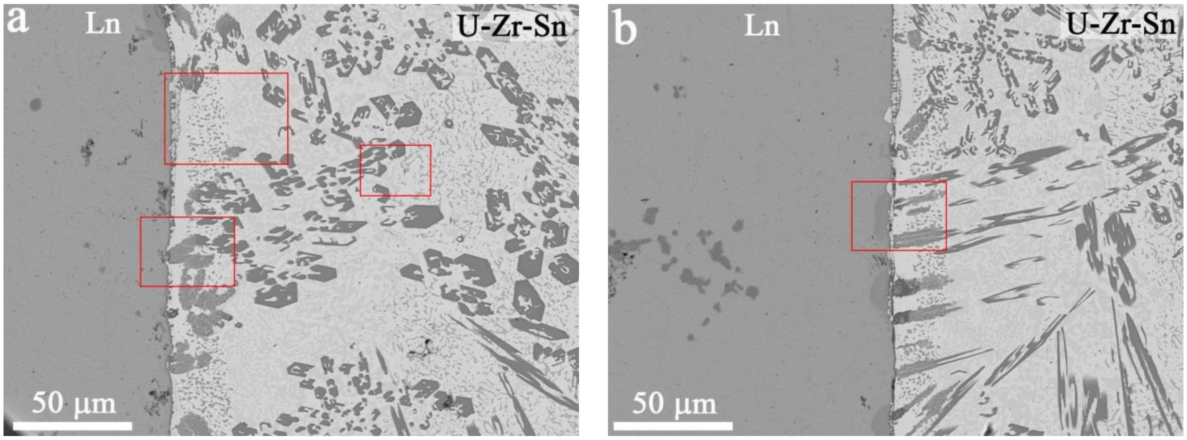

Figure 3-1. a. and b. SEM BSE images of diffusion zone. The red rectangles indicate the locations for the higher magnification images shown in Figures 3-2 and 3-3.

Figure 3-2 shows magnified images of the interaction zone. Figure 3-2a clearly shows the penetration of the lanthanides into the fuel, specifically along the Zr-Sn precipitates. The precipitate has a mottled appearance, with a range of small inclusions present (based on visual inspection). Most of the inclusions through the bulk of the precipitate are small, on the order of 1 mm, so were not analyzed by EDS due to the small size. The small inclusions and mottled appearance likely indicate that the reactions taking place are not complete, and the diffusion couple was quenched too soon. With that stated, there is still useful information in the EDS analysis. Points 1–3 (Figure 3-2a, Table 3-1) are the UZr_2 δ phase, inside what was once a Sn-Zr precipitate. Bands of δ phase are visible in all of the precipitates within the interaction zone. In the Zr_5Sn_3 precipitates (points 11 and 12), there is only residual amounts of U present, thus U is moving into the precipitate to bind the Zr released from Zr_5Sn_3.

Points 4 through 7, Figure 3-2a, are primarily Sn and lanthanides, with some Zr and a small amount of U. The Ln/Sn ratio is very close to Ln_5Sn_3, without including Zr. As previously discussed [10], Zr may be substituting into the crystal lattice, creating a $[Zr + Ln]_5Sn_3$ compound. Including Zr into the Ln/Sn ratio in points 5 through 7 indicates a composition of roughly $[Zr + Ln]_2Sn$. While not impossible, a 2 to 1 compound is unlikely since there are no known 2 to 1 compounds between the constituent lanthanides (Nd, Ce, Pr, La) and Sn, based on the binary phase diagrams. Other precipitates in the interaction zone that were analyzed (not shown) have a range of Zr present, from roughly 4 at % to above 12 at %. This could be due to Zr having a high solid solubility in Ln_5Sn_3, or perhaps Zr has not had enough time to migrate out of the precipitate.

Figure 3-2b shows a region of the interaction zone where constituents in the fuel diffused into the lanthanides. These regions were not present along the entire interaction zone, but were scattered throughout. Curiously, the composition of these regions was very consistent, with a representative example shown in Figure 3-2b. The amount of Sn is low, roughly 5 at%, with a small amount of Zr. The Zr rind is likely hindering diffusion of Sn into the lanthanides. In areas where Sn broke through, diffusion may be kinetically limited, given that the Sn concentration was always roughly 5 at%. This should be apparent after running a longer diffusion couple.

The lanthanide composition is also very consistent between these regions. Removing the small amounts of U, Zr, and Sn from the EDS points, and normalizing for the lanthanides yields a composition of 70.5Nd-18.9Ce-8.2La-2.4Pr in at %. This is significantly different from the starting lanthanide concentration, 52.3Nd-25.4Ce-16.2Pr-6.1La at%. This could indicate a preference for Sn to bind Nd, or could be due to the higher mobility of Ce, Pr, and La due to lower melting points. If the latter were true, a Nd rich region would be expected near the interface on the lanthanide side, with Ln_5Sn_3 precipitates on the fuel side containing a lower concentration of Nd. This is not the case, though. EDS points 13–15 in Figure 3-2a, and 5-7 in Figure 3-2b, are roughly the same compositions, and are very close to the cast composition of the lanthanides. The Nd content in the Ln_5Sn_3 precipitates on the fuel side also do not support the idea of higher mobility of Ce, Pr, and La over Nd. Normalizing the lanthanide content in points 4–7 (Figure 3-2a), and averaging the 4 data points yields a lanthanide content of 57.9Nd-22.8Ce-15.4La-3.9Pr, slightly high in Nd, and a little low in Ce and Pr. Although this is not conclusive, the trend indicates Sn is preferentially binding Nd over the other lanthanides present. A longer reaction time may help clarify this issue.

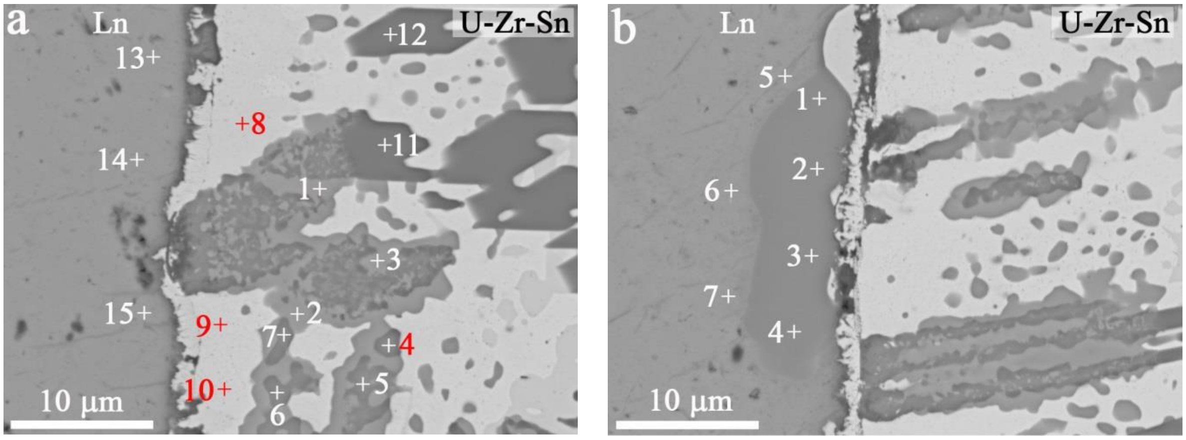

Figure 3-2. SEM BSE images of diffusion zone. Magnified region from red rectangle shown in Figure 3-1a; b. Magnified region from red rectangle shown in Figure 3-1b. EDS points listed in Table 3-1.

Table 3-1. EDS data for points shown in Figure 3-2. Values in atomic %.

	U	Zr	Sn	Nd	Ce	Pr	La
Figure 3-2a							
1	33.6	60.5	1.4	1.0	2.3	0.4	0.7
2	34.9	61.4	0.6	0.6	1.5	0.4	0.7
3	31.2	59.5	2.9	1.8	3.0	0.6	0.9
4	6.1	5.5	34.7	31.5	12.0	1.8	8.4
5	2.5	11.1	33.6	30.4	12.2	2.1	8.1
6	4.1	10.8	32.9	30.1	12.2	2.0	8.0
7	7.5	10.0	31.2	29.6	11.6	2.3	7.8
8	95.3	3.0	0.0	0.0	1.1	0.2	0.5
9	98.1	0.8	0.0	0.4	0.3	0.4	0.0
10	98.1	0.7	0.0	0.4	0.4	0.3	0.1
11	2.4	60.3	37.0	0.0	0.1	0.1	0.1
12	2.4	60.6	37.0	0.0	0.0	0.0	0.0
13	0.1	0.4	0.2	51.4	27.0	3.6	17.2
14	0.1	0.2	0.0	51.5	27.2	3.8	17.2
15	0.0	0.3	0.1	50.8	27.3	4.0	17.3
Figure 3-2b							
1	0.3	3.4	4.8	64.5	17.3	2.2	7.5
2	0.4	3.2	6.5	63.6	16.8	2.0	7.6

Table 3-1. (continued).

	U	Zr	Sn	Nd	Ce	Pr	La
3	0.3	3.0	6.3	63.9	16.9	2.2	7.4
4	0.1	2.9	5.5	64.7	17.3	2.1	7.4
5	0.0	0.4	0.0	50.9	27.4	3.6	17.6
6	0.0	0.2	0.2	51.6	27.2	3.4	17.4
7	0.0	0.2	0.1	51.3	27.3	3.7	17.4

Figure 3-3 shows images of the fuel matrix near the interface. In Figure 3-3a, there is an obvious change in the matrix at roughly 20 μm from the interface, corresponding to the depth of lanthanide diffusion into the fuel. The dark, globular precipitates stop abruptly, with a 2 phase, open matrix structure extending for roughly 75 μm. EDS points 1–4 in Figure 3-3a show the globular precipitates to be high in U and Zr, with residual lanthanides present, and no Sn. The structure is δ phase, either with dissolved U or U picked up in the EDS analysis from the surrounding matrix, which is primarily α-U (see EDS points 9 and 10, Figure 3-2a, Table 3-2).

The second region, the 2 phase open structure, is very low in Zr. The darker areas are a mix of α-U and δ phase, although there is significantly more α-U than δ phase, while the lighter areas are α-U. This zone is likely due to uranium moving into the region, and not a depletion of Zr. Uranium and the lanthanides are immiscible solids, so it appears the movement of lanthanides into the fuel is pushing some of the uranium out of the interaction zone.

The end of this middle zone is shown in Figure 3-3b. EDS analysis indicates the same composition throughout this area (points 5–8 in Figure 5-3a, and points 1–3 in Figure 3-3b). At the end of this zone, the matrix has the same appearance as the matrix area in the previously characterized U-10Zr-4.3Sn after annealing [10]. The EDS analysis (points 4–6) shows a slightly elevated concentration of U. This was observed previously, and attributed to the small size of the δ phase inclusions, due to depletion of Zr from the matrix, and limitations in the EDS method. The δ phase areas shown in Figure 3-3b are on the order of 1 μm, so this explanation is the likely the reason for the high U content.

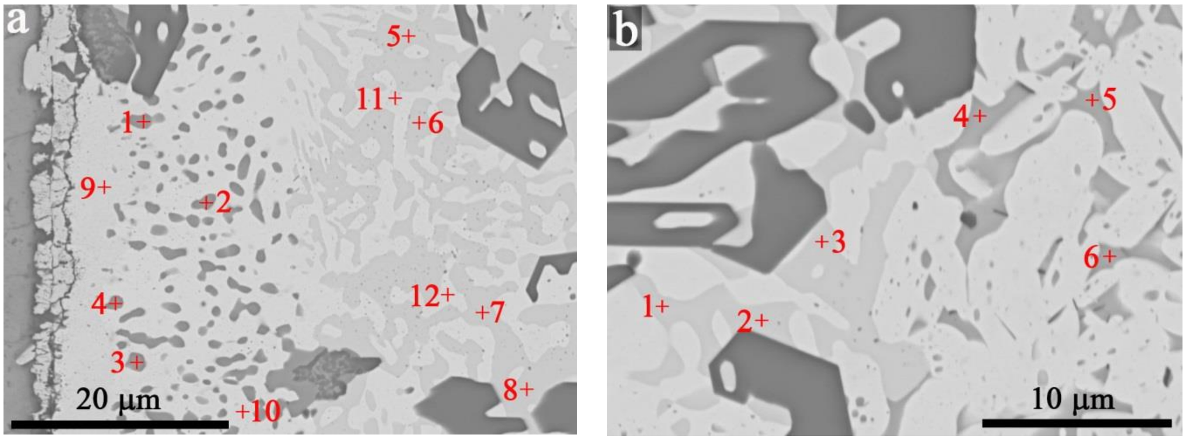

Figure 3-3. a. and b. SEM BSE images of extended interaction zone in the fuel. Magnified regions from red rectangles shown in Figure 3-1a. EDS points listed in Table 3-2.

Table 3-2. EDS data for points shown in Figure 3-3. Values in atomic %.

	U	Zr	Sn	Nd	Ce	Pr	La
Figure 3-3a							
1	40.7	57.9	0.0	0.0	0.9	0.3	0.3
2	44.1	54.4	0.0	0.0	0.9	0.3	0.4
3	39.4	58.5	0.0	0.0	1.5	0.4	0.2
4	42.9	55.2	0.0	0.0	1.1	0.5	0.3
5	73.9	25.3	0.0	0.0	0.4	0.1	0.3
6	72.6	25.9	0.0	0.0	0.7	0.4	0.4
7	73.8	25.6	0.0	0.0	0.3	0.3	0.0
8	73.8	25.4	0.0	0.0	0.4	0.3	0.1
9	94.8	2.9	0.0	0.0	1.3	0.6	0.4
10	98.0	1.0	0.0	0.0	0.4	0.3	0.3
11	95.5	4.3	0.0	0.0	0.1	0.1	0.0
12	98.5	1.0	0.0	0.0	0.3	0.2	0.1
Figure 3-3b							
1	72.5	26.4	0.0	0.0	0.5	0.4	0.1
2	72.4	27.0	0.0	0.0	0.4	0.1	0.1
3	72.6	26.8	0.0	0.0	0.3	0.3	0.0
4	40.1	59.4	0.0	0.0	0.3	0.1	0.1
5	40.8	59.0	0.0	0.0	0.1	0.0	0.0
6	41.2	58.5	0.0	0.0	0.1	0.1	0.0

3.5 Conclusions

The diffusion couple between U-10Zr-4.3Sn (wt%) and a mix of lanthanides (53Nd-25Ce-16Pr-6La wt%) has been analyzed by SEM. Although a longer reaction time may be needed to fully understand the diffusion, several conclusions are apparent from this investigation.

- The lanthanides aggressively attack the Sn-Zr precipitates. Sn-Zr is breaking apart in order to form Ln-Sn compounds.
- Uranium is moving into the precipitate to react with the released Zr, forming δ-phase, UZr_2.
- Uranium appears to be moving away from the interface, due to the movement of lanthanides into the fuel, and the immiscibility between the lanthanides and uranium.
- Tin moved into the lanthanides, but only in very small amounts. This could be due to the Zr rind that is prevalent in U-Zr fuels, or due to the lack of mobility of Sn while in Sn-Zr compounds. In other words, the Sn is inhibited from crossing the reaction front presented by the Sn-Zr compounds.

4. CHARACTERIZATION OF U-10ZR-2SN-2SB AND U-10ZR-2SN-2SB-4LN TO ASSESS SN+SB AS A MIXED ADDITIVE SYSTEM TO CONTROL FCCI

The full reference for the following manuscript is: M.T. Benson,Y. Xie, J.A. King, K.R. Tolman, R.D. Mariani, I. Charit, J. Zhang, M.P. Short, S. Choudhury, R. Khanal, N. Jerred, "Characterization of U-10Zr-2Sn-2Sb and U-10Zr-2Sn-2Sb-4Ln to assess Sn+Sb as a mixed additive system to control FCCI," *J. Nucl. Mater.*, **2018**, *510*, 210-218.

4.1 Abstract

Tin and antimony are being investigated as potential additives to metallic fuel to control fuel-cladding chemical interaction (FCCI). A primary cause of FCCI is lanthanide fission products moving to the fuel periphery and interacting with the cladding. This interaction can lead to wastage of the cladding and, given enough time or burn-up, eventually to a cladding breach. The current study involves a microstructural characterization of as-cast and annealed U-10Zr-2Sn-2Sb and U-10Zr-2Sn-2Sb-4Ln, where Ln=53Nd-25Ce-16Pr-6La, all in wt %, as alloys which could prevent FCCI. Scanning electron microscopy (SEM) analysis and X-ray powder diffraction indicates the additive-Zr compound in U-10Zr-2Sn-2Sb is $Zr_5(Sn,Sb)_3$, while the additive-Ln compound being formed in U-10Zr-2Sn-2Sb-4Ln is $Ln_5(Sn,Sb)_4$, with significantly more Sb than Sn (37 at. % versus 6 at. %, respectively). The bulk of the Sn, with a small amount of Sb, remained as $Zr_5(Sn,Sb)_3$ precipitates. The potential benefits of a mixed additive system, along with relative stabilities of the intermetallic compounds, are discussed.

4.2 Introduction

Fuel-cladding chemical interaction (FCCI) occurs when the nuclear fuel or fission products react with the cladding material. A major cause of FCCI in metallic fuels during irradiation is fission product lanthanides (Ln), which tend to migrate to the fuel periphery, coming in contact with the cladding. The result of this interaction is degradation of the cladding, and can eventually lead to rupture of the fuel assembly [1][2].

The lanthanides can be created as fission products, or can be present in fuel produced with recycled uranium. A small amount of lanthanides is expected to remain with uranium after pyroprocessing, thus being incorporated into fresh fuel [3]. In this case, as soon as the fuel contacts the cladding due to swelling, at roughly 1–2% burnup, there are already lanthanide impurities in the recycled fuel available to initiate FCCI. This early form of FCCI in recycled fuel will occur in an accelerated fashion in compared to the much slower creation of fission product lanthanides in fresh fuel fabricated with clean uranium. Controlling FCCI in this system is even more important due to the potentially reduced lifetime of the fuel [4].

In order to extend fuel life while minimizing the potential occurrence of a cladding breach, some method of controlling FCCI is needed. Several methods are being investigated to decrease or prevent FCCI, such as barrier foils [5], coatings [6], and additive materials. In the additive approach, criteria were developed that identified a set of elements that could be promising additives to bind lanthanides as stable intermetallics [7]. From this list, Pd [8][7], Sn [10], Sb [12][13], and In [14] have been investigated, and have all shown promise as a fuel additive. Pd-Ln precipitates were found and characterized in a recent post irradiation examination (PIE) [15] of a U-10Zr fuel irradiated in the Fast Flux Test Facility. The Pd is present as a fission product which creates precipitates with an average composition of 25Pd-75Ln, but not in a large enough concentration to bind all the lanthanides produced. These results are encouraging towards this method of controlling the lanthanides, especially considering that it naturally happens during irradiation.

Investigations of U-Zr alloys with the additives alone, and with the additives and a lanthanide mix, show that the additives can capture all lanthanides produced at up to 20 % burn-up [7]. The composition and ratio of lanthanides are based on elemental analysis of irradiated U-10Zr EBR-II fuel pins [7], with the four most prevalent lanthanides included in the mix. The ratio obtained from EBR-II fuel is 53Nd-25Ce-16Pr-6La, in wt. %. The starting concentrations of lanthanides in recycled fuel will have a slightly different elemental ratio, modified slightly from their fission product yields by the separation factors in the pyrometallurgical process.

This study presents an initial, out-of-pile investigation using Sn and Sb as a mixed fuel additive system. Recent investigations of Sn [10] and Sb [12] as individual additives have shown them to be promising candidates to reduce or mitigate FCCI. Both additives bind Zr in the fresh fuel and lanthanides following burn-up (in a simulated, out-of-pile experiment), subsequently releasing Zr back into the U-Zr matrix. We present a comparative study between these additives in terms of compound stabilities. Although the results are qualitative, they progress beyond those available in the literature. In addition to compound stabilities and the potentially competitive nature of two additives in the fuel, there is also the possibility of a synergistic effect between the additives. Both Sn and Sb have a range of oxidation states, but the primary oxidation states differ between the two elements (+2, +4 for Sn, and +3, +5 for Sb). There is the possibility of different reactivities towards Nd and Ce, which constitute the majority of lanthanides produced as fission products [7], and they do not have identical reactivities. If an additive has a preference towards Nd or Ce, a mixed additive system could be beneficial in preventing FCCI.

4.3 Experimental Methods

Two alloys were cast, U-10Zr-2Sn-2Sb wt. % (71.7U-21.7Zr-3.3Sn-3.3Sb at. %) and U-10Zr-2Sn-2Sb-4Ln wt. % (66.8U-21.3Zr-3.3Sn-3.3Sb-5.5Ln at. %), where Ln = 53Nd-25Ce-16Pr-6La wt. % (52.3Nd-25.4Ce-16.2Pr-6.1La at. %). All materials except uranium were obtained from Alfa Aesar as rods, packaged in mylar under argon, and used as received. Uranium was cleaned by submersion in nitric acid, followed by water and then ethanol washes.

All casting operations were carried out in an arc melter within an argon atmosphere glovebox with high purity argon as a cover gas. After each additive step, the resulting cast button was flipped and re-melted three times to ensure homogeneity. To prepare U-10Zr-2Sn-2Sb, the appropriate amounts of Sn, Sb, Zr, and U were arc melted together in two steps. A button of U-Zr was first prepared, followed by addition of Sn and Sb. The lanthanides mix, 53Nd-25Ce-16Pr-6La, was prepared by arc melting the appropriate amounts of each lanthanide together in one step. To prepare U-10Zr-2Sn-2Sb-4Ln, the appropriate amount of the Ln alloy was added to a pre-alloy button of U-Zr-Sn-Sb, prepared as described for U-10Zr-2Sn-2Sb. The buttons were cast into 5mm diameter pins. Details concerning the fabrication and analysis of U-10Zr-4Sb can be found in Reference [12].

Approximately 4mm from each pin was cut for annealing. The samples were wrapped in Ta foil, then sealed in quartz tubes under vacuum. The quartz tube was placed in a furnace at 650°C for 500 hours, based on a typical fuel operating temperature in a fast reactor. This is on the higher end of, but still within, the normal temperature range expected of fuel. After the heat treatment, the samples were quenched in water. The samples were then cut to expose a fresh surface for analysis.

Scanning electron microscopy (SEM) was performed on a section of pin from each alloy for both the as-cast and annealed forms. The samples were mounted in a 31.8 mm diameter phenolic metallographic (met) mount filled with epoxy. Samples were polished by grinding the surfaces flat with SiC grinding paper followed by polishing with polycrystalline diamond suspensions, starting with 9 µm, then 3 µm, and finally 1 µm. The polished samples were analyzed with a sputtered coating of approximately 15nm carbon to minimize charging of the metallographic mount.

A JEOL JSM-7600F scanning electron microscope (SEM) equipped with an Oxford Instruments X-Max 20 silicon drift energy dispersive X-ray spectrometer (EDS) and wavelength-dispersive X-ray spectrometer (WDS) was used for analysis. The X-ray spectrometer is controlled by Oxford INCA software (v. 4.15, part of the Oxford Microanalysis Suite Issue 18d + SP 4), which also provides image acquisition capabilities. The SEM was operated at an accelerating voltage of 20kV and a nominal beam current of approximately 84nA (which can vary somewhat with column conditions) for these analyses. Prior to analysis, X-ray detector response was verified using a copper target. All of the X-ray spectra were accumulated for 75 live seconds. Spectra were collected over an energy range of 0 – 20keV, which covers characteristic X ray energies from all analytes. Spectra were quantified using so-called “standardless” analysis, which uses a stored library of reference spectra to quantify unknown spectra rather than physical standards. This method is generally accurate to the 0.1 to 0.5 wt/wt. % range, depending on sample and microscope (observation) conditions.

XRD (model: PANalytical X’Pert Powder) was used for phase identification. Data were collected with the X’Pert Data Collector software. The scan rate was 0.06 degree/s, and the step size was 0.2 degree/ step. In addition to the lattice constants, the non-structural parameters, including background, peak shape, zero-point, and instrument line profile were also refined. The instrument line profile was characterized as the convolution of both equatorial and axial profiles. Equatorial divergence was refined using the receiving-slit width and the fixed-divergence slit angle parameters, while axial divergence was modeled using the Finger et al [37]. asymmetry correction. Background was fitted with a fourth-order Chebychev polynomial.

4.4 Results and Discussion

Tin has a low melting point (231.9°C), but a high boiling point (2,603°C) with a relatively low vapor pressure at fuel processing and operating temperatures. In previous work [10], there were no difficulties casting buttons and pins with Sn, and no apparent loss while casting. Antimony has a higher melting point (630.6°C) than Sn, but a lower boiling point (1587°C). In previous investigations with Sb as a fuel additive [12], some loss was observed due to boiling. A small amount of boiling was observed while casting these alloys, primarily during drop-casting of the pins. Some superheat is necessary when drop-casting to ensure the alloy drops as a single pulse into the hearth. During this process, some boiling was observed on the surface of the button, prior to dropping.

Both alloys were annealed at 650ºC for 500 hours. The temperature is based on the operating temperature of a fast reactor. This is on the higher end of the normal temperature range, but is within the normal range. No weight loss was observed in the samples after the heat treatment. After annealing the samples for 500 hours, the samples were analyzed, and the only difference in U-10Zr-2Sn-2Sb was the separation of the matrix into α-U and δ-UZr_2 phases. Given the high melting temperatures for the precipitates in these alloys, no change was expected in the precipitates. This assumption proved to be correct for U-10Zr-2Sn-2Sb, *vide infra*, and only minor changes occurred in U-10Zr-2Sn-2S-4Ln, as described in Section 4.4.2.

4.4.1 U-10Zr-2Sn-2Sb

The as-cast and annealed microstructures of the U-10Zr-2Sn-2Sb alloy are shown in Figure 4-1, with corresponding EDS data listed in Table 4-1. The only change between the as-cast and annealed structures is the separation of the matrix, i.e., α-U and δ-UZr_2 phases. The precipitates have essentially identical structures before or after the heat treatment. Given the high melting temperatures for the precipitates in these alloys, no change was expected in the precipitates. This assumption proved to be correct for U-10Zr-2Sn-2Sb, *vide infra*, and only minor changes occurred in U-10Zr-2Sn-2Sb-4Ln, as described in Section 4.4.2.

Visually, the precipitates are very similar to both U-10Zr-4Sn [10] and U-10Zr-4Sb [12], with triangular, dendritic precipitates, and large, hexagonal precipitates, although the large, round Zr_2Sb precipitates present in U-10Zr-Sb alloys [12] were not found by SEM in the current alloy. Based on the Zr-Sn binary phase diagram [24], there is no Zr_2Sn phase, which likely accounts for the lack of an observed 2-1 compound in the U-10Zr-2Sn-2Sb alloy.

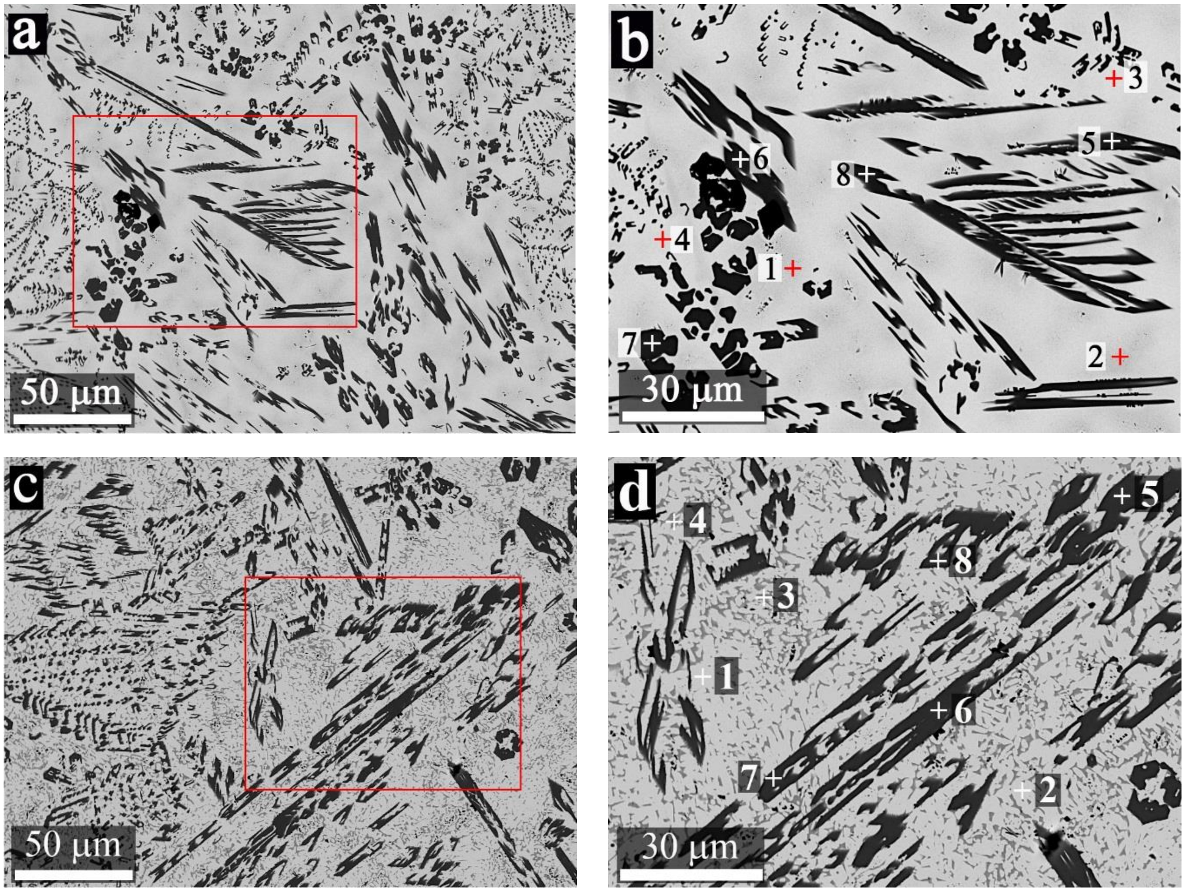

Figure 4-1. SEM BSE images for as-cast and annealed U-10Zr-2Sn-2Sb. a. As-cast large area view, b. Magnified region of as-cast alloy, taken from the center region of 4.1a, indicated with red rectangle, c. Annealed large area view, d. Magnified region of annealed alloy, taken from the center region of 4-1c, indicated with red rectangle. Corresponding EDS data are listed in Table 4.1.

Table 4-1. EDS data for points shown in Figure 4-1. Values in atom %.

	U	**Zr**	**Sn**	**Sb**	**Phase**[a]
Figure 4-1b					
1	75.9	23.5	0.6	0.0	—
2	77.0	22.2	0.7	0.2	—
3	92.7	6.1	1.1	0.1	—
4	90.3	8.2	1.2	0.3	—
5	3.6	59.6	18.1	18.6	$Zr_5(Sn,Sb)_3$
6	4.0	59.2	19.6	17.2	$Zr_5(Sn,Sb)_3$
7	2.9	60.0	20.9	16.3	$Zr_5(Sn,Sb)_3$
8	3.1	59.8	19.4	17.8	$Zr_5(Sn,Sb)_3$

Table 4-1. (continued).

	U	Zr	Sn	Sb	Phase[a]
Figure 4-1d					
1	98.1	1.2	0.7	0.0	α-U
2	98.4	0.9	0.7	0.0	α-U
3	37.9	61.4	0.3	0.4	δ-UZr$_2$
4	36.6	63.2	0.0	0.2	δ-UZr$_2$
5	2.8	60.0	20.2	17.0	Zr$_5$(Sn,Sb)$_3$
6	4.1	59.0	20.7	16.3	Zr$_5$(Sn,Sb)$_3$
7	3.6	59.4	19.3	17.8	Zr$_5$(Sn,Sb)$_3$
8	3.5	59.6	18.6	18.4	Zr$_5$(Sn,Sb)$_3$

a. Suggested phase based on EDS analysis.

As noted above, some boiling was observed when dropping the buttons into pins, accounting for the loss of Sb apparent in the precipitates. There is roughly 20 at. % Sn in the precipitates, but only around 17.5 at. % Sb. This does not appear to alter the phases present, but it does alter the ratio of Sn to Sb. In the precipitates, the ratio of Zr to Sn+Sb is very close to Zr$_5$(Sn,Sb)$_3$. This is the same Zr to additive ratio (Zr$_5$Sn$_3$) as found in U-10Zr-4Sn [12]. An SEM image of U-10Zr-4Sb is shown in Figure 4.2, with corresponding EDS data listed in Table 4-2. The dendritic and hexagonal precipitates in U-10Zr-Sb [12] were assumed to be Zr$_2$Sb, based on the EDS analysis. Although points 1, 2, and 3 clearly indicate a Zr$_2$Sb stoichiometry, Zr$_5$Sb$_3$ can exist with the off-stoichiometry of Zr$_2$Sb [38]. This would account for the hexagonal appearance of the precipitates, identical to those found for Zr$_5$Sn$_3$.

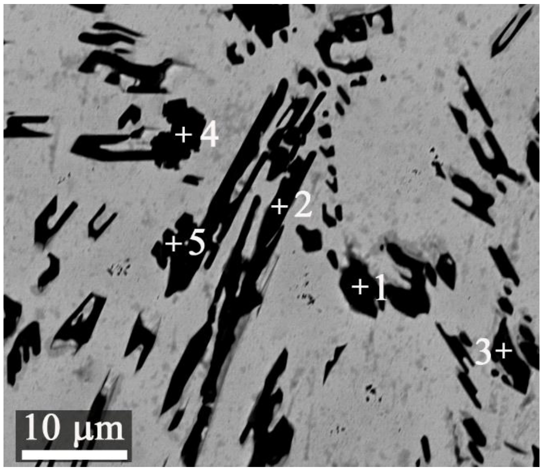

Figure 4-2. SEM BSE image of U-10Zr-4Sb. Corresponding EDS data listed in Table 4-2.

Table 4-2. EDS data for points shown in Figure 4-2. Values in atom %.

	U	Zr	Sb	Phase[a]
1	5.0	62.6	32.4	Zr$_2$Sb or Zr$_5$Sb$_3$
2	4.5	64.1	31.4	Zr$_2$Sb or Zr$_5$Sb$_3$
3	5.6	62.0	32.4	Zr$_2$Sb or Zr$_5$Sb$_3$
4	0.8	99.0	0.2	α-Zr
5	1.4	98.3	0.3	α-Zr

a. Suggested phase based on EDS analysis.

Points 4 and 5 in Figure 4-2 and Table 4-2 correspond to Zr precipitates in the U-10Zr-4Sb alloy. In similar U-Zr based alloys, these precipitates have been identified as α-Zr [7][30], or in the case of a quenched alloy, β-Zr [9]. It has been postulated these precipitates are stabilized by oxygen or nitrogen [30], even though the U-Zr binary phase diagram [27] indicates they should not exist. Precipitates of Zr are present when Pd is used as a metallic fuel additive [8][7], and are clearly present in U-10Zr-4Sb, as shown in Figure 4 2. Precipitates of Zr were not found in U-10Zr-4Sn [10], and are not found in this study. As much as 15 at. % Zr was found in the Sn-Ln precipitates [10]. It is not known if this was due to the solubility of Zr or the existence of a possible ternary compound. In the analysis of Sb-Ce precipitates [12], only residual amounts (<2 at. %) of Zr were found. The lack of Zr precipitates in alloys containing Sn, and the presence of Zr in the Sn-lanthanide precipitates, indicate that Zr has a stronger affinity for Sn than for Sb.

No free additives were observed in previous additive studies with Sn [10] and Sb [12], which is also the case in the alloys in this study, nor were compounds observed between Sn and Sb. Based on the Sn-Sb phase diagram [39], all of the compounds between Sn and Sb, as well as the metals themselves, have a liquidus temperature significantly below the operating temperature of a fast reactor. If any precipitates of the additives were present, or compounds of the additives in the U-10Zr-2Sn-2Sb alloy, a melted region within the annealed alloy would be an obvious indicator. The disadvantages of the additive binding Zr in the fresh fuel have been discussed [10][12], i.e., lowering the solidus temperature of the alloy. The obvious advantage, especially when the additive(s) have a low melting point, is to prevent the additive from melting prior to the lanthanides burning into the fuel during irradiation.

To confirm the phase assignments made in the SEM analysis, XRD was performed on the sample. Figure 4-3 shows the XRD spectrum with peak assignments shown, with corresponding crystal data listed in Table 4-3. Six phases were identified. The first two, α-U and δ-UZr_2, account for the bulk of the sample. UO_2 was identified, and is due to oxidation occurring during sample prep and while running the XRD. Fabrication in the arc melter occurs under flowing high purity argon, using clean uranium. Although a small amount of oxidation may occur during fabrication, the UO_2 identified by XRD is likely due to surface oxidation. The remaining three phases identified correspond to additive-Zr compounds. Zr_5Sn_3 is shown in Figure 4-3 as the identified phase, although based on the SEM analysis, the structure is the substitutional compound $Zr_5(Sn,Sb)_3$. Based on the Zr-Sb phase diagram [40], Zr_5Sb_3 is a known compound. Due to the excess of Zr present, as compared to Sn + Sb, the next Zr-rich compound in the Zr-Sn phase diagram [24], $Zr_{3.2}Sn_{0.8}$, and Zr-Sb phase diagram [40], Zr_2Sb, were also identified. Neither of these compounds are miscible with $Zr_5(Sn,Sb)_3$, though, so should be separate precipitates in the alloy. These compounds were not found in the SEM analysis, and are likely minor constituents.

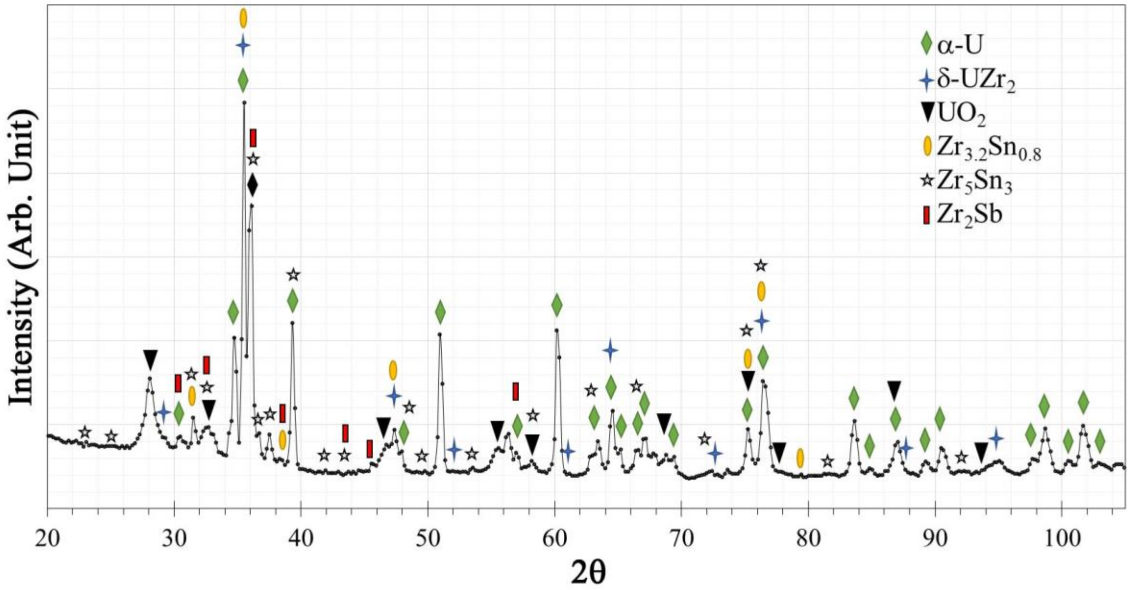

Figure 4-3. XRD spectrum for U-10Zr-2Sn-2Sb with peak assignments shown.

Table 4-3. Crystal data for phases identified in U-10Zr-2Sn-2Sb.

Phase	a (Å)	b (Å)	c (Å)	Volume (Å^3)	Space Group	JCPDS
α-U	2.8647(10)	5.8578(19)	4.9746(15)	83.479(47)	*Cmcm*	04-004-5443
δ-UZr$_2$	4.9928(28)	4.9928(28)	3.0314(20)	65.443(85)	*P6/mmm*	04-004-9102
UO$_2$	5.4817(27)	5.4817(27)	5.4817(27)	164.72(25)	*Fm-3m*	01-073-2293
Zr$_{3.2}$Sn$_{0.8}$	5.6650(17)	5.6650(17)	5.6650(17)	181.80(16)	*Pm-3n*	04-004-2315
Zr$_5$Sn$_3$	8.458(12)	8.458(12)	5.7922(86)	358.9(11)	*P6$_3$/mcm*	00-018-1393
Zr$_2$Sb	4.1289(98)	4.1289(98)	15.788(81)	269.2(19)	*I4/mmm*	00-045-0948

4.4.2 U-10Zr-2Sn-2Sb-4Ln

The lanthanides were added to a pre-alloy of U-Zr-Sn-Sb, fabricated via the same method as described for the U-10Zr-2Sn-2Sb alloy. The U-Zr-Sn-Sb pre-alloy should have a similar microstructure as U-10Zr-2Sn-2Sb; thus in order for additive-lanthanide compounds to form, additive-Zr compounds must decompose. Previous studies with Sn [10] and Sb [12] as additives have indicated the relative stability of the additive-lanthanide compound is greater than the additive-Zr compound. In the case of Sn [10], small amounts of Zr are present in the Sn-Ln precipitates, roughly 11-15 at. %. The reason for the Zr being present, whether due to high solubility of Zr or possibly a ternary phase between Sn, Zr, and Ln, is unclear. This was not observed in the Sb-Ln precipitates [12], which contained only residual amounts, i.e., < 1.5 at. %, of Zr. As with the Zr precipitates discussed above, this result indicates a higher stability of Zr-Sn compounds compared to Zr-Sb compounds.

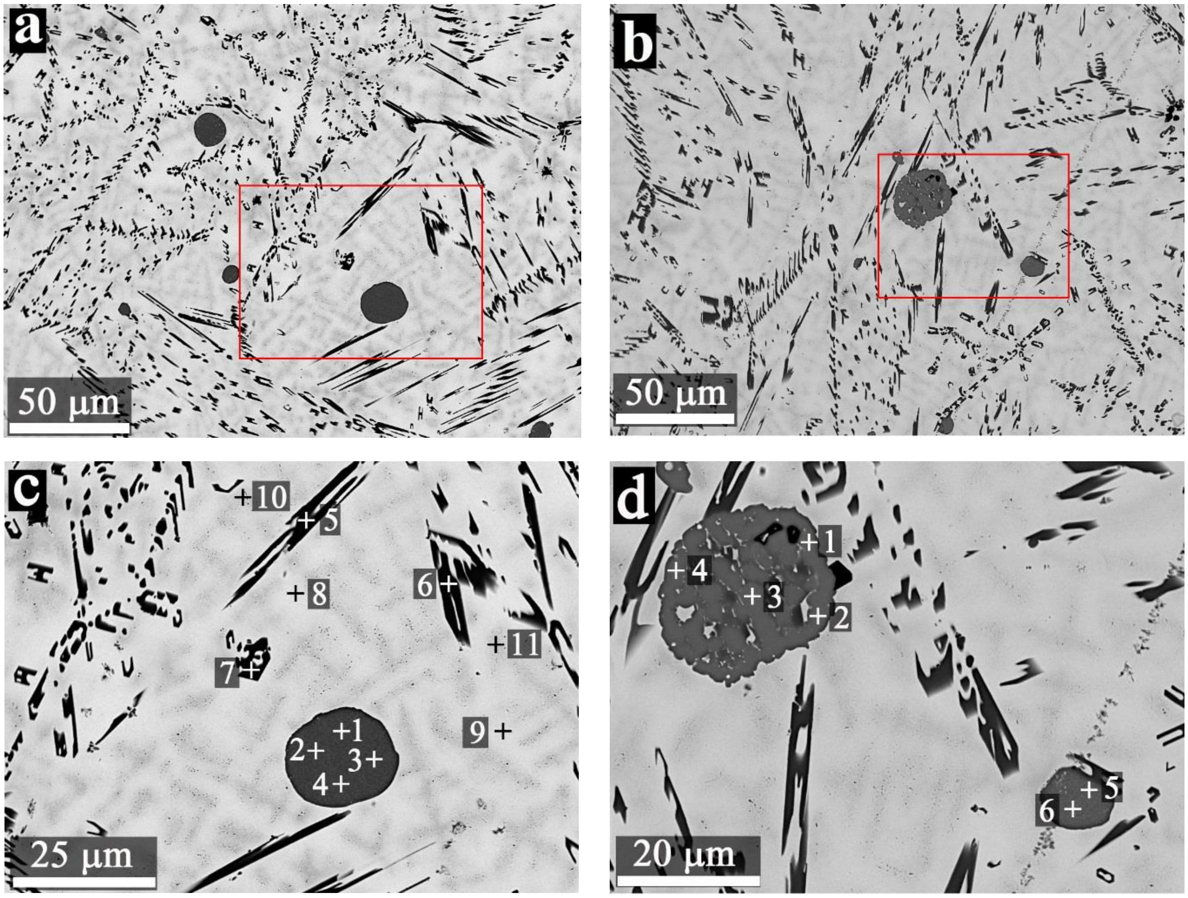

Figure 4-4. SEM BSE images for as-cast U-10Zr-2Sn-2Sb-4Ln. a. and b. Large area images, c. Magnified region of 4-4a, indicated by the red rectangle, d. Magnified region of 4-4b, indicated by the red rectangle. Corresponding EDS data are listed in Table 4-4.

Table 4-4. EDS data for points shown in Figure 4-4. Values in atom %.

	U	Zr	Sn	Sb	Nd	Ce	Pr	La	Phase[a]
Figure 4-4c									
1	1.6	7.8	7.2	31.8	24.8	18.4	3.5	4.9	$Ln_5(Sn,Sb)_4$
2	2.1	10.0	7.0	30.5	25.2	17.4	3.2	4.5	$Ln_5(Sn,Sb)_4$
3	1.6	7.0	7.2	32.4	25.0	18.7	3.3	4.7	$Ln_5(Sn,Sb)_4$
4	1.8	7.4	6.8	31.9	25.0	18.8	3.3	5.1	$Ln_5(Sn,Sb)_4$
5	11.8	56.1	19.3	11.2	1.0	0.4	0.1	0.0	$Zr_5(Sn,Sb)_3$
6	7.0	56.8	22.1	12.1	1.3	0.5	0.1	0.1	$Zr_5(Sn,Sb)_3$
7	6.7	57.2	21.7	12.6	1.3	0.5	0.1	0.0	$Zr_5(Sn,Sb)_3$
8	87.0	11.6	1.1	0.1	0.0	0.0	0.0	0.0	—
9	84.5	14.0	0.9	0.0	0.0	0.1	0.4	0.0	—
10	70.2	28.6	0.7	0.0	0.0	0.1	0.3	0.0	—
11	69.1	28.9	1.3	0.3	0.0	0.2	0.1	0.1	—

	U	Zr	Sn	Sb	Nd	Ce	Pr	La	Phase[a]
Figure 4-4d									
1	2.7	1.8	4.8	37.8	25.2	19.0	3.3	5.4	$Ln_5(Sn,Sb)_4$
2	1.9	1.1	4.5	38.9	24.9	19.8	3.5	5.5	$Ln_5(Sn,Sb)_4$
3	1.6	1.0	4.1	40.0	24.7	19.9	3.4	5.3	$Ln_5(Sn,Sb)_4$
4	2.5	2.5	4.6	37.8	24.8	19.4	3.5	5.0	$Ln_5(Sn,Sb)_4$
5	1.8	6.6	7.5	32.3	25.3	17.9	3.6	5.0	$Ln_5(Sn,Sb)_4$
6	2.4	9.8	7.1	31.3	24.3	17.1	3.4	4.7	$Ln_5(Sn,Sb)_4$

a. Suggested phase based on EDS analysis.

In the as-cast microstructure for U-10Zr-2Sn-2Sb-4Ln, shown in Figure 4-4, the additive-Ln precipitates appear either homogeneous or speckled, with U and Zr trapped in the precipitate. The homogeneous precipitate shown in Figure 4-4c, with EDS data listed in Table 4.4, contains a higher amount of Zr and Sn than the speckled precipitate shown in Figure 4d. Higher amounts of Sn, ~7 at. % in the precipitate shown in Figure 4-4c versus ~4.5 at. % Sn in the speckled precipitate shown in Figure 4-4d, allows the Zr to remain in the precipitate. When the Sn concentration drops, Zr falls out of solution, forming black inclusions inside the precipitate. The Sb content is above 30 at. % in both precipitates. The ratio of lanthanides to the additives (Sn+Sb), indicates that the precipitates are $Ln_5(Sn,Sb)_4$. EDS analysis also indicates there is more Sn remaining in the Zr-additive precipitates than Sb. In the EDS analysis for the as-cast alloy, Figure 4-4c and Table 4-4, there is roughly a 2 to 1 ratio of Sb to Sn. This drops to a ratio of 1.7 in the annealed structure, shown later in Figure 4-6b and Table 4-5.

In the annealed microstructure, shown in Figures 4-5 and 4-6, the additive-Ln precipitates contain large inclusions. EDS analysis, points 9 and 10 in Figure 4-6a and Table 4-5, indicates the inclusion is a mix of U, Zr, and Sn. This is likely the result of annealing a precipitate such as the speckled one shown in Figure 4-4d. The Sn and Sb in the precipitates are composed of roughly 6 at. % Sn and 37 at. % Sb. As with the as-cast precipitates, the ratio of Ln to additives indicates the structure is $Ln_5(Sn,Sb)_4$. This is in contrast to the precipitates identified between Sb and Ce [12], which were identified as Ce_4Sb_3 and Ce_2Sb. Identification of the precipitates in the Sn system was more ambiguous, depending on whether Zr is part of the structure [10]. Without including Zr, the ratio of Ln to Sn is closer to Ln_5Sn_4, but when Zr is included the precipitate appears to be $Ln_5(Sn,Zr)_3$.

Based on the relevant binary phase diagrams between Sb and the lanthanides [41][42], the 5-4 compound, i.e., Ln_5Sb_4, is not a known phase between Sb and any of the lanthanides present. The small amount of Sn present, around 6 at. %, may be stabilizing this phase, or this may be a possibly unidentified phase between Sb and the lanthanides. Based on the Sn-Nd binary phase diagram [41], the Nd_5Sn_4 and Nd_5Sn_3 phases are both very stable. Removing Sn from the phase makes the Ln to Sb ratio close to Ln_3Sb_2. This is also not a known phase between Sb and the lanthanides, making a Sn-stabilized $Ln_5(Sn,Sb)_4$ phase the most likely possibility. The U-10Zr-2Sn-2Sb-4Ln alloy has a molar excess of additive (Sn + Sb). It may be possible to push the phase to $Ln_5(Sn,Sb)_3$ if the amount of lanthanides were to be increased. This is a known phase between Sb and Nd, and is a known phase between Sn and the lanthanides. The precipitate would then have a more advantageous ratio of lanthanides to additives, i.e., more lanthanides consumed per mole of additive.

As with the U-10Zr-2Sn-2Sb alloy, XRD was performed on U-10Zr-2Sn-2Sb-4Ln to identify phases present, shown in Figure 4.7, with corresponding crystal data listed in Table 4-6. The bulk of the alloy is comprised of α-U and δ–UZr_2, with some UO_2 present. As discussed previously in Section 4.4.1, UO_2 is present as surface oxidation due to exposure during sample prep and during the XRD run. The lanthanide-additive phase identified corresponds to Nd_5Sn_4. Nd was used for structure identification since it is the highest concentration lanthanide in the Ln mix. As previously stated, Nd_5Sb_4 is not a known structure, based on the Nd-Sb phase diagram [41]. Likely Ln-Sb compounds, such as Nd_2Sb, Nd_5Sb_3, Nd_4Sb_3, and NdSb, were not identified in the XRD spectrum. Only one lanthanide-additive compound was identified, making $Ln_5(Sn,Sb)_4$ the correct phase, although it is not known whether this is a Sn-stabilized phase, or if Nd_5Sb_4 is a stable, but unknown phase.

There is a small molar excess of the additives (Sn+Sb) over the lanthanides, which accounts for the $Zr_5(Sn,Sb)_3$ dendritic and hexagonal precipitates present in both the as-cast (Figure 4-4), and the annealed (Figures 4-5 and 4-6), microstructures for U-10Zr-2Sn-2Sb-4Ln. The precipitates are considerably smaller than those found in U-10Zr-2Sn-2Sb alloy and include significantly more U. Due to the small size of the precipitates, U from the surrounding matrix is likely contributing to the EDS results, artificially raising the measured concentration of U. For example, points 1-4 in Figure 4-6b and Table 4-5 indicate 17-22 at. % U in the precipitates. This is a significant increase over the 2-4 at. % U found in the precipitates shown in Figure 4-1 and Table 4-1 for U-10Zr-2Sn-2Sb. These EDS values are suspect for the $Zr_5(Sn,Sb)_3$ precipitates in U-10Zr-2Sn-2Sb-4Ln, but the trend in Sn and Sb content is very consistent. This phase assignment is confirmed by XRD, as shown in Figure 4-7. Zr_5Sn_3 was identified, although, as with the previous alloy, this will be the substitutional compound $Zr_5(Sn,Sb)_3$. Based on SEM analysis, the ratio of Sn to Sb is significantly different, although the phase is still the same. The other compounds, $Zr_{3.2}Sn_{0.8}$ and Zr_2Sb, were not identified. That could be due to these phases no longer being present, or the concentration could be below the detection limits of the XRD.

The relative stability of the Sn-Ln interaction versus the Sb-Ln interaction is uncertain based on this investigation. The large excess of Sb present in $Ln_5(Sn,Sb)_4$ may indicate a stronger interaction between Sb and the lanthanides, but the strong Sn-Zr interaction may be the cause of this excess. Due to the molar excess of Sn + Sb over the lanthanides, some of the additive present has to remain with Zr. If the relative stabilities of the Sn-Ln and Sb-Ln interactions are similar, the strong Sn-Zr interaction will determine the Sn and Sb content in both $Zr_5(Sn,Sb)_3$ and $Ln_5(Sn,Sb)_4$. The excess additive remaining with Zr will be Sn, while most of the Sb will be present in the lanthanide precipitates.

As suggested in the introduction, a mixed additive system could be beneficial if the additives had different reactivities towards Nd and Ce. That has not been clearly demonstrated in this study. There does appear to be a slightly higher concentration of Ce in the $Ln_5(Sn,Sb)_4$ precipitates, based on the idealized lanthanide ratio of 53Nd-25Ce-16Pr-6La. Without a chemical analysis to confirm the Ln ratio, the increase in Ce is not conclusive. There could be a difference in reactivity between the additives and Nd and Ce, but the chemical stability differences between the additives and Zr, and likely also the additives and the lanthanides in general, are potentially masking any reactivity differences between the additives and Nd and Ce individually.

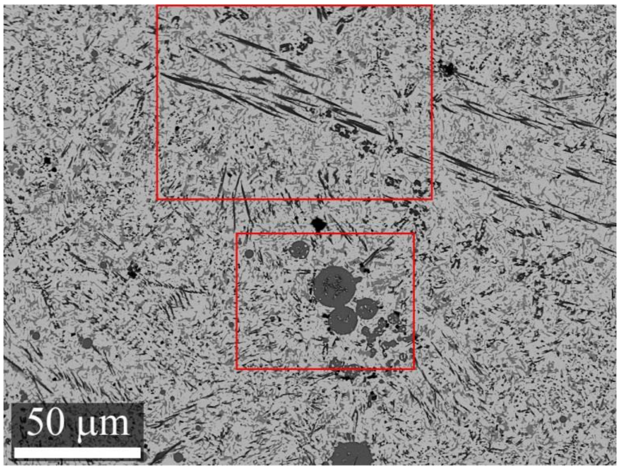

Figure 4-5. SEM BSE large area image of annealed U-10Zr-2Sn-2Sb-4Ln. Red rectangles correspond to high magnification images shown in Figure 4-6.

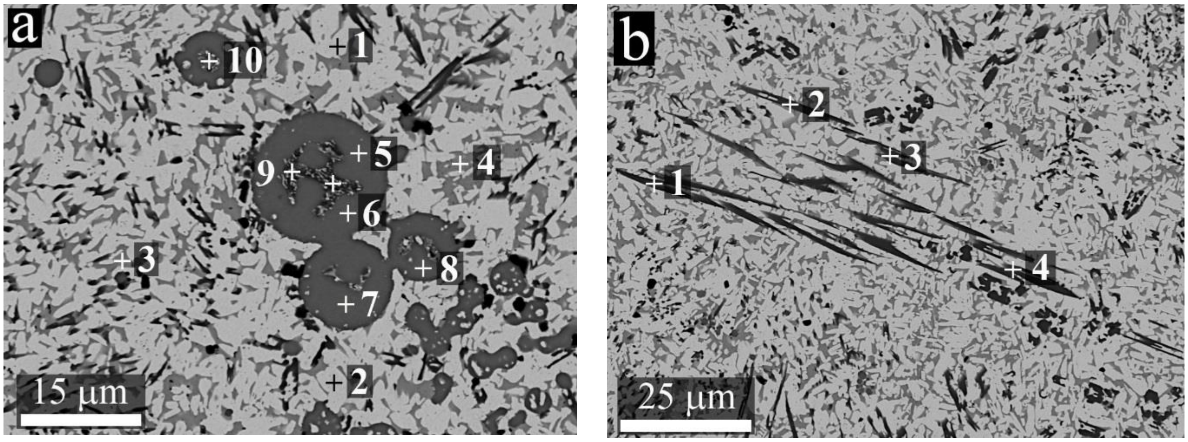

Figure 4-6. a. and b. SEM BSE images of annealed U-10Zr-2Sn-2Sb-4Ln. Location of images correspond to red rectangles shown in Figure 4-5. Corresponding EDS data are listed in Table 4-5.

Table 4-5. EDS data for points shown in Figure 4-6. Values in atom %.

	U	Zr	Sn	Sb	Nd	Ce	Pr	La	Phase[a]
Figure 4-6a									
1	97.3	1.4	0.8	0.2	0.0	0.1	0.2	0.0	α-U
2	97.4	1.0	0.9	0.2	0.0	0.1	0.2	0.0	α-U
3	34.3	65.3	0.1	0.1	0.0	0.1	0.1	0.0	δ-UZr_2
4	34.6	64.5	0.5	0.4	0.0	0.0	0.1	0.0	δ-UZr_2
5	1.6	1.2	6.3	37.2	25.9	18.8	3.0	6.0	$Ln_5(Sn,Sb)_4$
6	1.5	1.0	6.1	37.3	26.1	18.7	3.3	6.0	$Ln_5(Sn,Sb)_4$
7	1.5	1.2	6.7	36.5	26.0	18.9	3.4	5.9	$Ln_5(Sn,Sb)_4$
8	1.6	1.2	6.2	36.7	26.0	19.1	3.3	5.9	$Ln_5(Sn,Sb)_4$
9	18.4	56.3	14.7	4.0	3.5	2.1	0.4	0.5	—
10	15.9	62.8	15.9	3.4	1.1	0.6	0.2	0.1	—

	U	Zr	Sn	Sb	Nd	Ce	Pr	La	Phase[a]
Figure 4-6b									
1	17.5	56.3	15.5	9.2	0.8	0.5	0.2	0.1	$Zr_5(Sn,Sb)_3$
2	17.5	61.2	12.3	7.3	0.6	0.7	0.2	0.2	$Zr_5(Sn,Sb)_3$
3	22.3	59.6	10.7	6.3	0.6	0.4	0.1	0.0	$Zr_5(Sn,Sb)_3$
4	17.1	55.5	16.7	9.3	0.9	0.4	0.1	0.0	$Zr_5(Sn,Sb)_3$

a. Suggested phase based on EDS analysis.

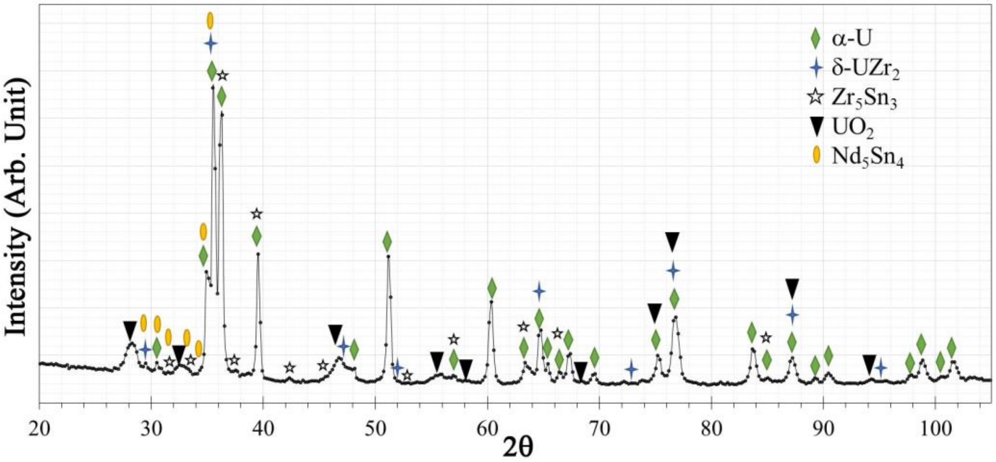

Figure 4-7. XRD spectrum for U-10Zr-2Sn-2Sb-4Ln with peak assignments shown.

Table 4-6. Crystal data for phases identified in U-10Zr-2Sn-2Sb-4Ln.

Phase	a (Å)	b (Å)	c (Å)	Volume ($Å^3$)	Space Group	JCPDS
α-U	2.85696(65)	5.8729(13)	4.9700(12)	83.391(33)	*Cmcm*	04-004-5443
δ-UZr_2	4.9835(67)	4.9835(67)	3.0408(62)	65.40(22)	*P6/mmm*	04-004-9102
UO_2	5.4969(30)	5.4969(30)	5.4969(30)	166.10(28)	*Fm*-3*m*	01-073-2293
Zr_5Sn_3	8.5800(27)	8.5800(27)	5.7783(33)	368.39(31)	$P6_3/mcm$	00-018-1393
Nd_5Sn_4	8.016(11)	15.828(26)	8.423(11)	1068.7(27)	*Pnma*	04-012-8061

The X-ray peak energies for Sn and Sb are very close, with L_α = 3.443 keV for Sn and 3.604 keV for Sb. Software deconvolution of the peaks can certainly affect the results. Using WDS with elemental standards would be ideal for generating accurate chemical analysis data, but standards were not available for these samples. WDS without standards cannot confirm the analysis results, but can confirm qualitatively if the trends are correct. To this end, a WDS line scan was performed, as shown in Figure 4-8. The red arrow indicates the path of the line and the direction of the scan. The line crosses the matrix, both α-U and δ-UZr_2, the $Zr_5(Sn,Sb)_3$ precipitates, and a $Ln_5(Sn,Sb)_4$ precipitate.

The α-U phase, with some δ-UZr_2, is obvious in the U map at 5-10 μm, ~14 μm, and ~25-30 μm. The δ-UZr_2 areas are small, but are obvious in the Zr map. The peaks at 7, 25, and 28 μm correspond to δ-UZr_2. The $Zr_5(Sn,Sb)_3$ precipitates are obvious in both the Sn and Sb maps. All of the peaks in these maps, except for the large region at 15 mm to 25 mm, corresponds to $Zr_5(Sn,Sb)_3$ precipitates. The peaks in the Sn map are roughly double the peaks in the Sb map, indicating a significantly higher amount of Sn than Sb in the $Zr_5(Sn,Sb)_3$ precipitates. The average values obtained from EDS analysis indicate the Sn/Sb ratio is 1.8/1.0 (average of peaks 9-12 in Table 4.4) for the as-cast sample, and 1.7/1.0 (average of peaks 1-4 in Table 4.5) for the annealed sample. The large precipitate in the center of the line scan, from 15 μm to 25 μm, corresponds to Ln$_5$(Sn,Sb)$_4$. The Sn and Sb maps indicate roughly three times as much Sb as Sn in the precipitate. The Sn/Sb ratio determined by EDS analysis is 0.2 for both the as-cast and annealed samples (using points 1–4 in Table 4.4 for the as-cast material and points 7-11 in Table 4-5 for the annealed material). The WDS maps indicate more Sn present in the precipitates that the EDS data, but the trend is clear, i.e., there is significantly more Sb in the Ln$_5$(Sn,Sb)$_4$ precipitates than Sn.

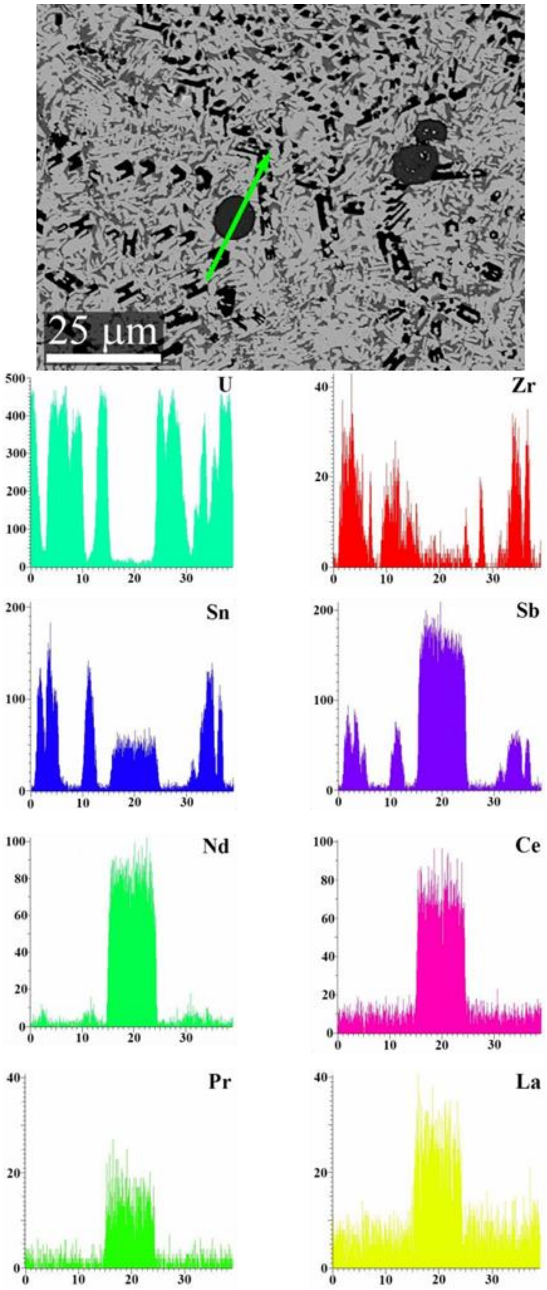

Figure 4-8. SEM BSE image of U-10Zr-2Sn-2Sb-4Ln with WDS line scan maps. The green arrow in the SEM image indicates the line and the direction of the scan. x-axis in micrometers, y axis is relative intensity.

4.5 Conclusions

In this investigation, the as-cast and annealed microstructures of U-10Zr-2Sn-2Sb wt. % (71.7U-21.7Zr-3.3Sn-3.3Sb at. %) and U-10Zr-2Sn-2Sb-4Ln wt. % (66.8U-21.3Zr-3.3Sn-3.3Sb-5.5Ln at. %) were analyzed by SEM and XRD. The following conclusions can be drawn from the data presented:

- Upon addition of lanthanides, most of the Sb present in $Zr_5(Sn,Sb)_3$ releases Zr to bind the lanthanides, while Sn primarily remains with Zr. Previous work with Sn [10] indicates Sn will release Zr and bind the lanthanides, but in this competitive additive system, Sn remains with Zr. Based on these observations, the Sn-Zr interaction is stronger than the Sb-Zr interaction.
- A mixed additive system, with each additive having a binding preference to a different lanthanide, Nd or Ce, would be beneficial towards binding lanthanide fission products. The greater chemical stability differences between Sn and Sb towards Zr, and possibly towards the lanthanides in general, overshadowed any possible difference in reactivity towards individual lanthanides (Nd or Ce).
- The lanthanide-additive phase identified by SEM and XRD is $Ln_5(Sn,Sb)_4$. The primary additive in the precipitates is Sb, present in ~ 37 at. %, with a small amount of Sn present, ~6 at. %. This stoichiometry is not a known phase between the lanthanides and Sb, although it is a known phase between the lanthanides and Sn. The phase is likely stabilized by the addition of Sn.

5. MICROSTRUCTURAL CHARACTERIZATION OF ANNEALED U-12ZR-4PD AND U-12ZR-4PD-5LN: INVESTIGATING PD AS A METALLIC FUEL ADDITIVE

The full reference for the following manuscript is: M.T. Benson, L. He, J.A. King, R.D. Mariani, “Microstructural characterization of annealed U-12Zr-4Pd and U-12Zr-4Pd-5Ln: Investigating Pd as a metallic fuel additive,” *J. Nucl. Mater.*, **2018**, *502*, 106-112.

5.1 Abstract

Palladium is being investigated as a potential additive to metallic fuel to control fuel-cladding chemical interaction (FCCI). A primary cause of FCCI is the lanthanide fission products moving to the fuel periphery and interacting with the cladding. This interaction will lead to wastage of the cladding and, given enough time or burn-up, eventually to a cladding breach. The current study is a scanning electron microscopy (SEM) and transmission electron microscopy (TEM) characterization of annealed U-12Zr-4Pd and U-12Zr-4Pd-5Ln, where Ln=53Nd-25Ce-16Pr-6La. The present study shows that Pd preferentially binds the lanthanides over other fuel constituents, which may prevent lanthanide migration and interaction with the cladding during irradiation. The SEM analysis indicates the 1:1 Pd-Ln compound is being formed, while the TEM analysis, due to higher resolution, found the 1:1 compound, as well as Pd-rich compounds Pd_2Ln and Pd_3Ln_2.

5.2 Introduction

Fission product lanthanides (Ln) are a major cause of fuel-cladding chemical interaction (FCCI) in metal fuels during [15]. Lanthanides tend to migrate to the fuel periphery, coming in contact with the cladding. The result of this interaction is degradation of the cladding, and will eventually lead to rupture of a fuel pin [1][2]. Several methods are being investigated to decrease or prevent FCCI, such as barrier foils and coatings as well as additive materials [5][6][7][10][12][14]. After considering ways to bind lanthanides as stable intermetallics, a set of criteria were developed that identified Pd as a promising additive, especially since it is already a fission product. Recent work using Pd as an additive has shown promising results [7][16][17]. Diffusion couples between Ln (where Ln=Nd, Ce, Pr) and iron show no interaction when Pd is present at 700°C, whereas in the absence of Pd, all three lanthanides interact extensively with Fe at 700°C. [16][17]

Palladium is being investigated as an additive to control FCCI in metallic fuels specifically due to lanthanides. The lanthanide content arises in two possible ways: they can burn-in as fission products, and they can be present in the fresh fuel produced with recycled uranium. Regarding recycled uranium, a small amount of lanthanides are expected to remain with uranium after pyroprocessing, thus being incorporated into a “fresh,” recycled fuel [3]. Controlling FCCI in this system is even more important due to the potentially premature FCCI resulting in reduced lifetime of the fuel [4]. In this case, as soon as the fuel contacts the cladding due to swelling, at roughly 1-2% burnup, there are already lanthanides available to initiate FCCI. The potential for premature FCCI in recycled fuel contrasts with the much slower burn-in of fission product lanthanides in a fuel fabricated with clean uranium.

The current study continues investigating Pd as a fuel additive. A previous study [7] examined the as-cast microstructures for U-Zr-Pd and U-Zr-Pd-Ln alloys. In this investigation, the annealed microstructures, characterized with both scanning electron microscopy (SEM) and transmission electron microscopy (TEM), are discussed for U-12Zr-4Pd and U-12Zr-4Pd-5Ln. Investigating the annealed structures has two benefits. First, understanding how the alloys behave with palladium incorporated at reactor temperature is an important part of understanding how the alloys will behave as a fuel. The anneal temperature (650ºC) is within the normal operating temperature of a fast reactor. In addition, TEM lamella can be cut thin enough for diffraction analysis. This is not always possible with as-cast alloys, due to internal stresses.

The composition and ratio of lanthanides used in the alloys are based on elemental analysis of irradiated U-10Zr EBR- fuel pins [7], with the four most prevalent lanthanides included in the mix. The ratio obtained from elemental analysis is 53Nd-25Ce-16Pr-6La, in wt %. The amount of lanthanides used in these alloys, 6.6 at%, corresponds to the amount of lanthanides produced at roughly 18% burn-up for U-10Zr fuel in the EBR-II reactor [7]. The Pd content, 4 wt%, is the concentration needed to bind all of the lanthanides present in a 1:1 compound, with a small excess to remain on the Pd-rich side of the phase diagram. This burn-up, and corresponding Ln and Pd concentrations, is much higher than what was previously qualified (10% burn-up) by U.S. DOE. This content is somewhat arbitrarily investigated to reflect higher burn-ups desired plus lanthanide carryover in recycled fuel. Of course the actual lanthanide content in recycled fuel is yet to be established, as well as the ratios of one lanthanide to another. These investigations are roughly based on having less than 1 wt% lanthanides in the recycled fuel [3]. Considering previous diffusion couple work [16][17], varying the concentration of lanthanides present should not decrease the efficacy of Pd in binding the lanthanides.

5.3 Experimental Methods

Two alloys were cast, U-12Zr-4Pd wt% (67.6U-25.2Zr-7.2Pd at%) and U-12Zr-4Pd-5Ln (61.9U-24.5Zr-7.0Pd-6.6Ln at%), where Ln = 53Nd-25Ce-16Pr-6La wt% (52.3Nd-25.4Ce-16.2Pr-6.1La at%). All materials, except uranium, were obtained from Alfa Aesar and used as received. The lanthanides were obtained as rods, packaged in mylar under argon. Uranium was cleaned by submersion in nitric acid, followed by a water wash, then an ethanol wash.

Alloy fabrications were carried out in an arc melter, with high purity argon as a cover gas, located in an argon atmosphere glovebox. After each addition step in the arc melter, the resulting button was flipped and re-melted 3 times to ensure homogeneity. To prepare U-12Zr-4Pd, the appropriate amount of Pd, Zr, and U were arc melted together in two steps. Pd and Zr were melted together first, followed by addition of U. To prepare 53Nd-25Ce-16Pr-6La, the appropriate amount of each lanthanide was arc melted together in one step. To prepare U-12Zr-4Pd-5Ln, the appropriate amount of the Ln alloy was added to a pre-alloy of U-Zr-Pd, prepared by adding U and Zr first, followed by Pd. The buttons were cast into 5mm diameter pins.

To anneal the samples, sections from each alloy were wrapped in Ta foil, then sealed in a quartz tube under vacuum. The quartz tube was placed in a furnace at 650°C for 500 hours. After the heat treatment, the samples were quenched by breaking the quartz in water. The samples were cut to expose a fresh surface for analysis. Scanning electron microscopy (SEM) was performed on a 2 mm section of the pin mounted in a 31.8 mm diameter phenolic metallographic (met) mount filled with epoxy. Samples were polished by grinding the surfaces flat with SiC grinding paper followed by polishing with polycrystalline diamond suspensions, starting with 9 µm, then 3 µm, and finally 1 µm. The polished sample was analyzed with a sputtered coating of approximately 15 nm carbon to control charging of the met mount.

The SEM instrument used for sample analysis was a JSM-7600F SEM manufactured by the Japan Electron Optics Laboratory (JEOL). The JSM-7600F is a hot field emission SEM equipped with an Oxford Instruments X-Max 20 silicon drift energy dispersive X-ray spectrometer (EDS). The X-ray spectrometers are controlled by Oxford INCA software (v. 4.15, part of the Oxford Microanalysis Suite Issue 18d + SP 4), which also provides image acquisition capabilities. The SEM was operated at an accelerating voltage of 20 kV and a nominal beam current of approximately 75 nA (which can vary somewhat with column conditions) for these analyses. Prior to analysis, X-ray detector response was verified using a copper target. All of the X-ray spectra were accumulated for 100 live seconds. Spectra were collected over the energy range 0 – 20 keV, which covers characteristic X-ray energies from all analytes.

Spectra were quantified using so-called “standardless” analysis, which uses a stored library of reference spectra to quantify unknown spectra rather than physical standards. This method is generally accurate to the 0.1 to 0.5 wt/wt% range, depending on sample and microscope (observation) conditions. Quantification was not performed using wavelength dispersive spectroscopy (WDS) because suitable standards are not available for radiological samples.

TEM samples were prepared by a dual-beam focused ion beam (FIB, Quanta 3D FEG, FEI Company) system at the Center for Advanced Energy Studies. Platinum coating was deposited to protect the surface before cutting. TEM lamellas were created by coarse trenching 20 × 15 × 15 μm samples using the FIB. Samples were thinned down in the FIB during a final milling step of 5 kV at 77 pA ion emission current until small perforations were observed. FIB damage was cleaned with a final polish using 2 kV at 27 pA ion emission current. A 300 kV Tecnai TF30 scanning transmission electron microscope (STEM) equipped with a high-angle annular dark-field (HAADF) detector and an EDS detector was used for structure and composition analysis.

5.4 Results and Discussion

5.4.1 U-12Zr-4Pd

Figure 5-1 shows SEM images for U-12Zr-4Pd, both as-cast and annealed. The as-cast structure has been previously reported, and is shown for comparison [43]. Another U-Zr-Pd alloy (U-15Zr-3.86Pd) has also been previously reported [7], fabricated by adding U and Zr first, followed by Pd. In that alloy, the Pd-Zr precipitates deposit along the grain boundaries, whereas in the current system, shown in Figure 5-1a, that is not the case. The change in addition order is pointed out for completeness, and is not part of this investigation. The small changes in visual appearance caused by addition order do not affect the results of this study.

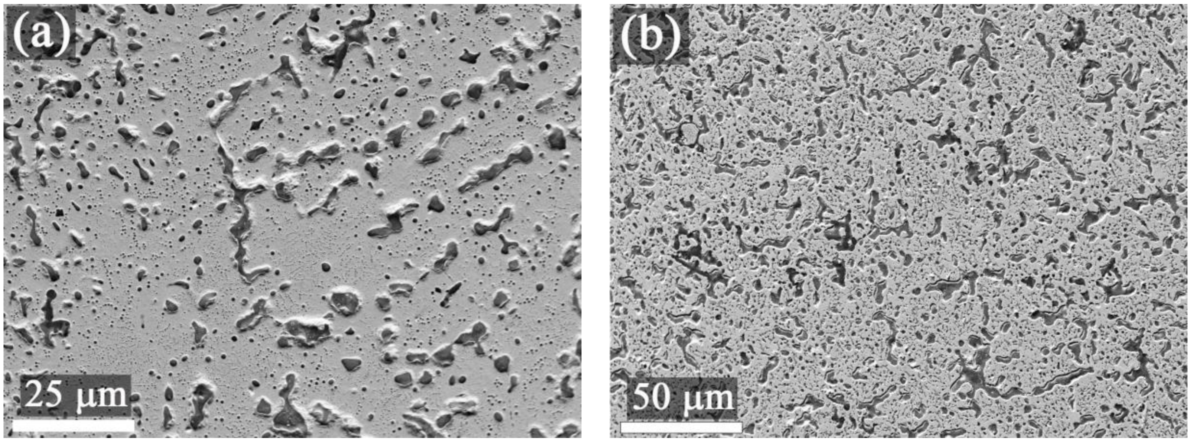

Figure 5-1. a. SEM BSE image for as-cast U-12Zr-4Pd, reported in Ref. [7]. A large area EDS scan of the as-cast alloy shows the composition to be 82.6U-12.8Zr-4.6Pd (wt%). b. SEM BSE image after annealing.

The microstructure of the as-cast alloy, shown in Figure 5-1a, has several obvious features. The black precipitates are high in Zr, the grey precipitates are Zr and Pd, and the light grey matrix areas are high in U with some Zr. The matrix is nondescript, although in backscattered electron (BSE) mode the light and dark matrix areas are visible, as previously reported [7]. The δ-UZr_2 phase cannot be detected with SEM or XRD in an as-cast, U-rich alloy [25], thus there is no differentiation in the matrix region between α-U and δ-UZr_2. The dark matrix areas have a higher Zr content, as has been discussed in the literature for U-Zr based alloys [10][25][43]. The matrix is essentially the same in this alloy as for a U-rich U-Zr alloy, because the Pd is tied up in precipitates with Zr. Upon heating, the phases separate and become clearly distinguishable, as shown in Figures 5-1b and 5-2. It is important to note that the phase discussions based on SEM are inferred from the EDS analysis. TEM analysis, described below, confirms the phase assignments.

Only one annealing time was investigated for these alloys. The only obvious change in the alloys between the as-cast [7] and annealed microstructures was the separation of the matrix into α-U and δ-UZr_2. The precipitates are essentially the same between the as-cast microstructures [7] and the annealed microstructures discussed in this study, within the limitations of the SEM EDS measurements.

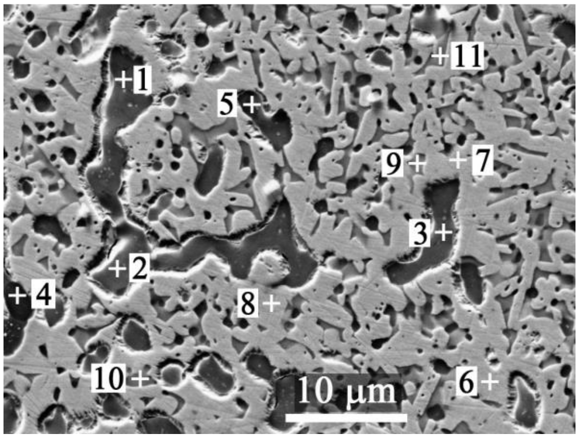

Figure 5-2. SEM BSE image for annealed U-12Zr-3.86Pd. Corresponding EDS data are listed in Table 5-1.

Table 5-1. EDS data for points shown in Figure 5-2. Values in atomic %.

	U	**Zr**	**Pd**	**Phase**[a]
1	1.1	65.6	33.3	$PdZr_2$
2	2.7	64.6	32.7	$PdZr_2$
3	3.2	64.7	32.1	$PdZr_2$
4	2.7	96.7	0.6	α or β-Zr
5	10.2	85.1	4.6	α or β-Zr
6	97.0	1.2	1.8	α-U
7	96.9	1.3	1.8	α-U
8	97.3	1.1	1.6	α-U
9	42.3	56.0	1.7	δ-UZr_2
10	40.5	57.6	1.9	δ-UZr_2
11	42.7	53.6	3.7	δ-UZr_2

a. Suggested phase based on EDS analysis.

The locations of the EDS analysis points are shown in Figure 5-2, with the data listed in Table 5-1. Based on the EDS data, there are 4 phases present in this system post-annealing; α-U, δ-UZr_2, α or β-Zr, and $PdZr_2$. As discussed below, the β phase of Zr is preserved due to quenching the sample. On the other hand, the higher temperature phases of U (β or γ) are not preserved when quenching in a U-10Zr alloy [44][45]. Two of the points shown, 4 and 5, are Zr precipitates. Although the U-Zr phase diagram [27] indicates these precipitates should not exist, they are a common feature and have been well documented [30].

In Figure 5-2, the EDS points 9-11 are for the δ phase, UZr_2. The values shown in Table 5-1 for these points do not show the correct composition for UZr_2, but have an excess of U. This is likely due to the small δ phase regions and the inaccuracy of SEM EDS, i.e. some of the surrounding U has been included in the composition. As previously reported [43], additives can potentially deplete Zr from the matrix, besides binding lanthanides. Starting with 7.2 at% Pd and forming $PdZr_2$ will require 14.4 at% Zr, making the effective U-Zr matrix composition 89.2U-10.8Zr in at%. This is the maximum Zr available after $PdZr_2$ precipitation, not taking into account Zr-rich precipitates that will further deplete the available Zr. Based on the U-Zr binary phase diagram [27], the solidus/liquidus temperatures will be 1175/1245°C. Using U-10Zr in wt% (U-22.5Zr at%) as the standard, the solidus/liquidus is decreased by 70/110°C. This is the trade-off using an additive in a metallic fuel. If enough Zr is added to maintain the solidus/liquidus temperatures, there is a decrease in the amount of fissionable material. Otherwise, there is a decrease in the solidus liquidus temperatures. The current study is an out-of-pile microstructural investigation, thus the optimal loading of Zr to balance the solidus/liquidus temperatures and concentration of fissionable material is outside the scope of this work. This relationship is pointed out since it is present anytime a non-fissile additive is added into a fuel.

The current alloys have 12 wt% Zr to help negate this Zr depletion, so the solidus/liquidus temperatures are higher than they would be in a 10wt% Zr alloy. If the alloy was U-10Zr-4Pd (U-21.6Zr-7.4Pd at%), the nominal matrix composition after depletion by $PdZr_2$ would be U-7.3Zr (at%), with solidus/liquidus temperatures of 1160/1215°C. That’s a solidus temperature only 25°C above the U melting point. Raising the Zr content more will certainly increase the solidus/liquidus temperatures, but at the cost of fissionable material in the fuel. In the previously reported U-15Zr-3.86Pd alloy [7], the high Zr content was to ensure enough Zr remained in the matrix to keep the solidus/liquidus temperatures close to U-10Zr.

In the previous report characterizing U-15Zr-3.86Pd [7], there were ambiguities in the measured compositions, and possible ternary phases were suggested. There is no phase diagram information available for the ternary U-Zr-Pd system, thus there is no data to confirm or deny the suggestions. There may be ternary intermetallics, or perhaps a two component phase has a high solubility for the third component. To help answer these questions, the annealed alloys were investigated with TEM. While the prior publication gave results for as-cast samples, only annealed alloys underwent TEM examination, especially since as-cast microstructure and metastable phases are not expected to survive reactor conditions.

Figure 4-3a shows the surface of U-12Zr-4Pd, with the lamella location marked with the platinum deposit. The finished lamella is shown in Figure 4.3b. The lamella has a mottled appearance due to multiple insoluble phases, as expected from the SEM image of the surface shown in Figure 4-2. Figure 4-4 shows HAADF-STEM images of the lamella with the location of the EDS points collected, with EDS data provided in Table 4-2. Figure 4-4a is the entire lamella, while 4.4b is an expanded view of the left side of the lamella (indicated by the red square shown in Figure 4-4a).

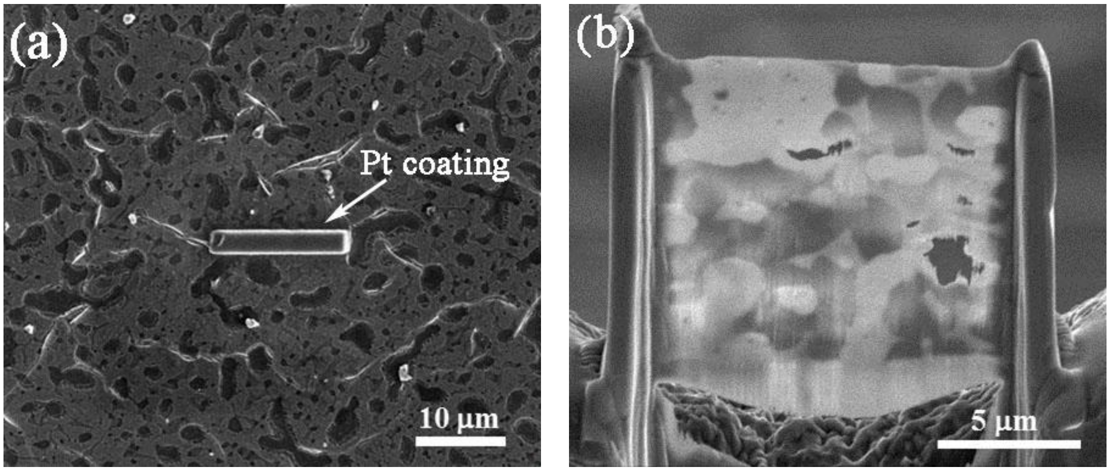

Figure 5-3. SEM images of U-12Zr-4Pd showing (a) the location of FIB lift-out and (b) the prepared TEM lamella.

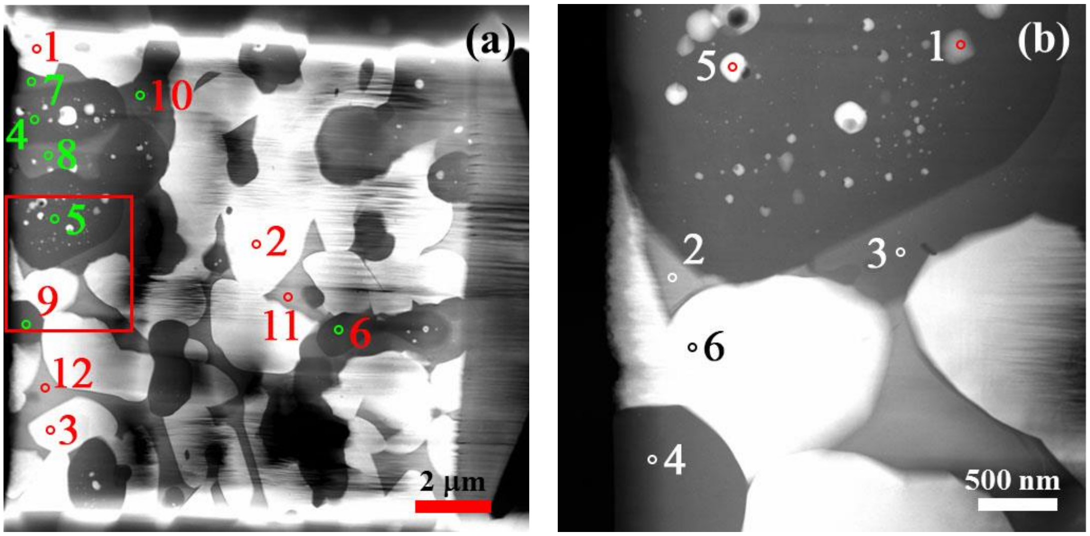

Figure 5-4. a and b. STEM images of annealed U-12Zr-4Pd lamella. The red square in (a) indicates the magnified region shown in (b). Corresponding data are listed in Table 5-2.

Table 5-2. EDS data for points shown in Figure 5-4. Values in atomic %.

	U	Zr	Pd	Phase[a]
Figure 5.4a				
1	100	0	0	α-U
2	100	0	0	α-U
3	100	0	0	α-U
4	0	100	0	α or β-Zr
5	0.6	99.4	0	α or β-Zr
6	0	100	0	α or β-Zr
7	0.6	64.8	34.6	$PdZr_2$

Table 5-2. (continued).

	U	Zr	Pd	Phase[a]
Figure 5.4a				
8	0	64.8	35.2	$PdZr_2$
9	0.5	62.3	37.2	$PdZr_2$
10	0.3	62.3	37.4	$PdZr_2$
11	30.9	69.0	0.1	δ-UZr_2
12	31.9	68.1	0	δ-UZr_2
Figure 5.4b				
1	34.0	66.0	0	δ-UZr_2
2	38.0	62.0	0	δ-UZr_2
3	0	62.4	37.6	$PdZr_2$
4	0	61.8	38.2	$PdZr_2$
5	100	0	0	α-U
6	100	0	0	α-U

a. Suggested phase based on EDS analysis.

The binary phase diagram for Zr and Pd indicates a variety of intermetallic compounds are possible, from $PdZr_2$ on the Zr-rich side to $ZrPd_3$ on the Pd-rich side. Normalizing the amount of Zr and Pd present to a binary composition yields 78Zr-22Pd at%, making $PdZr_2$ the likely intermetallic. The binary phase diagram for U and Pd shows UPd_3 as the only possible intermetallic, based on the alloy being U-rich (90U-10Pd at%). No evidence has been found to suggest this is forming, indicating the preference for Pd to bind Zr. This analysis is supported by the EDS data collected, by both SEM and TEM.

There are small discrepancies in the EDS data, Table 5-2, likely arising from solid solubilities. For example, a slightly high concentration of Pd is found in $PdZr_2$. This is due to Pd having some amount of solid solubility in $PdZr_2$. The analysis points for δ-UZr_2 also contain slightly high concentrations of either U or Zr, also indicating a solid solubility for U or Zr in δ-UZr_2. No evidence was found to support ternary structures, either by diffraction analysis or EDS analysis.

Selected area electron diffraction (SAED) was performed at six locations in the lamella, with the diffraction patterns shown in Figure 5-5. In Figure 5-5, (a) through (f) were collected at points corresponding to EDS points in Figure 5-4a, specifically points 1, 7, 4, 8, 5, and 12, respectively. The parameters used to index the phases are listed in Table 5-3. The diffraction data confirms the assignments made based on the EDS analysis. The phases present are α-U, δ–UZr_2, $PdZr_2$, and β-Zr. While the β–Zr is preserved by water-quenching the sample, the high temperature U phases are not.

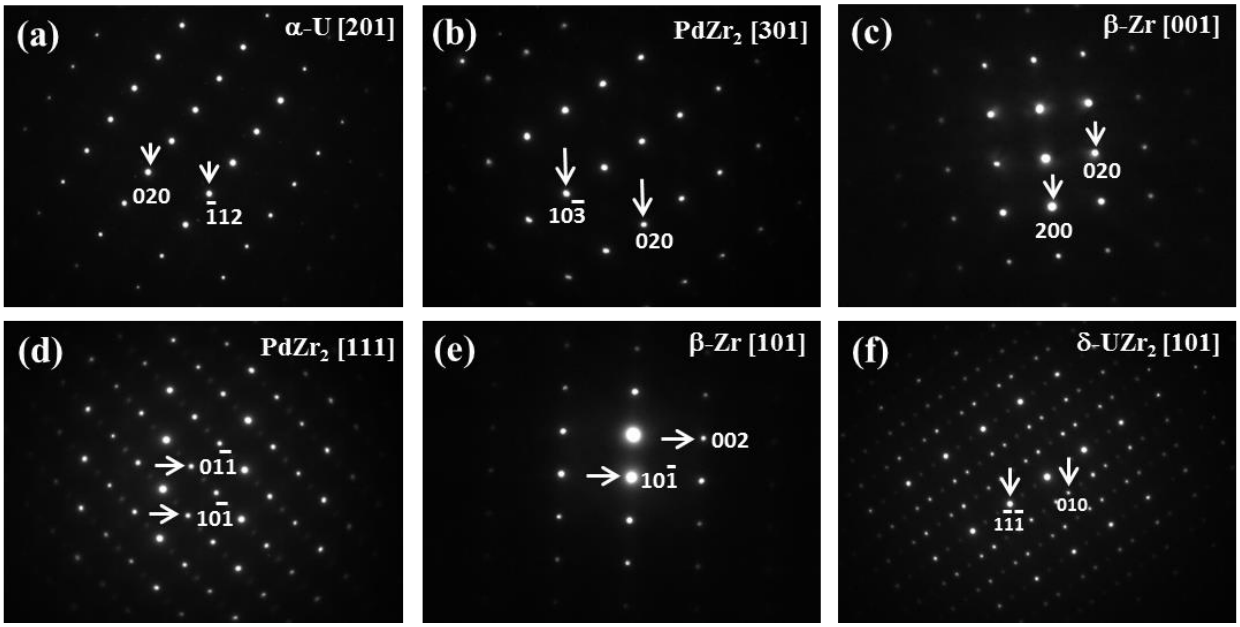

Figure 5-5. SAED patterns of (a) α-U [201], (b) $PdZr_2$ [301], (c) β-Zr [001], (d) $PdZr_2$ [101], β-Zr [101], and (f) δ-UZr_2 [101] in U-12Zr-4Pd TEM lamella. The location of the collected diffraction patterns of (a), (b), (c), (d), (e), and (f) corresponds to points 1, 7, 4, 8, 5, and 12, respectively, in Figure 5-4a.

Table 5-3. Space group and cell parameters of α-U, β-Zr, $PdZr_2$, and δ-UZr_2 phases used for indexing diffraction patterns.

Phase	Space group	Cell parameters	References
α-U	Cmcm (63)	a = 0.28536 nm b = 0.58698 nm c = 0.49555 nm α = β = γ = 90°	[46]
β-Zr	Fm-3m (225)	a = b = c = 0.453 nm α = β = γ = 90°	[47]
$PdZr_2$	I4/mmm (139)	a = b = 0.3306 c = 1.0832 nm α = β = γ = 90°	[48]
δ-UZr_2	P6/mmm (191)	a = b = 0.503 c = 0.308 nm α = β = 90° γ = 120°	[49]

5.4.2 U-12Zr-4Pd-5Ln

Figure 5-6 shows images of the as-cast and annealed microstructures for U-12Zr-4Pd-5Ln, with a magnified image of the annealed microstructure shown in Figure 5-7. This alloy was fabricated by adding U and Zr first, followed by Pd and then lanthanides when arc melting. As previously reported for U-15Zr-3.86Pd [7], there is precipitation of $PdZr_2$ along the grain boundaries in the as-cast microstructure. This feature is carried over from the U-Zr-Pd alloy when adding the lanthanides, as shown in Figure 5-6a.

Based on a visual inspection of the annealed microstructure for U-12Zr-4Pd-5Ln, shown in Figure 5-7, and the annealed microstructure for U-12Zr-4Pd, shown in Figure 5-2, there is significantly more Zr in the matrix in U-12Zr-4Pd-5Ln. Since Pd effectively binds the lanthanides, less Pd is available for binding Zr, and more Zr is therefore present in the U-Zr matrix in comparison to the matrix for U-12Zr-4Pd described above. This qualitative assessment is based on a simple, visual exam of the annealed microstructures, although it is supported by the analysis described below.

The high magnification image of the annealed microstructure is shown in Figure 5-7 with points indicating the locations of the collected EDS spectra, with the data listed in Table 5-4. Points 1–4 were taken within the large, round precipitates. The ratio is very close to the 1:1 Pd-Nd compound, with a slight excess of Pd. The other phases present correspond to phases found in U-12Zr-4Pd, i.e., UZr_2, Zr, and α-U, with the exception of $PdZr_2$, which is not found. Even though there is a slight excess of Pd, $PdZr_2$ was not found in the SEM analysis. Instead, the excess Pd is distributed throughout the other phases. This distribution of Pd is advantageous in that Pd is available to bind the lanthanides as they burn-in throughout the entire fuel, as opposed to only being available from randomly distributed Pd-Zr precipitates.

The precipitates shown in Figure 5-7 are similar to those observed in the post-irradiation examination (PIE) of a U-10Zr fuel [15]. In the PIE results, stable Pd-Ln precipitates have been characterized by EDS analysis. The lanthanide composition differs in the PIE results, as would be expected between a simplified out-of-pile experiment and a precipitate comprised of fission products, and there is less Pd, since only fission product Pd is available. Even with these obvious differences, the existence of Pd-Ln precipitates in spent fuel supports the idea of using a fuel additive to control the lanthanides, and also helps to validate using out-of-pile experiments to understand the interactions between Pd and the lanthanides.

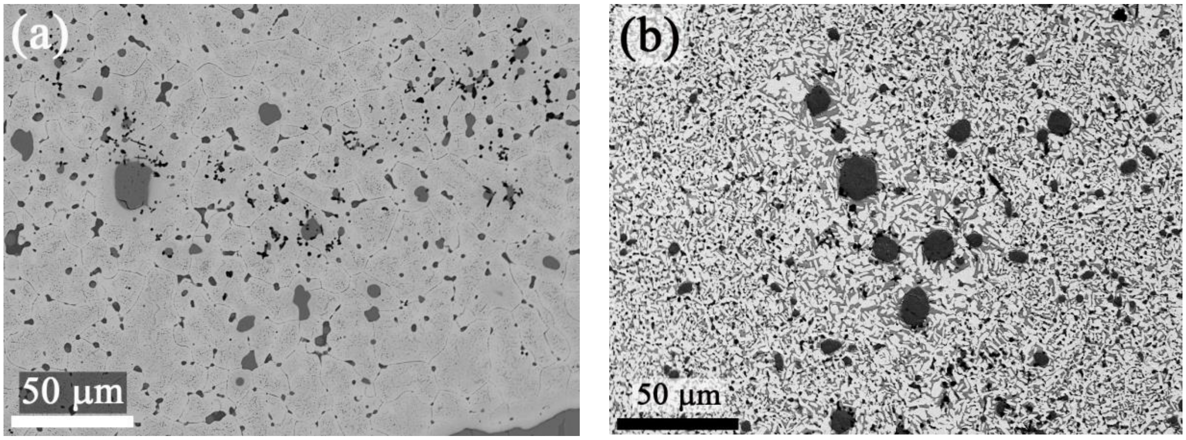

Figure 5-6. a. SEM BSE image of as-cast U-12Zr-4Pd-5Ln. A large area scan of the as-cast alloy indicates the composition is 79.2U-11.7Zr-4.3Pd-4.8Ln (wt%). b. SEM BSE image of annealed alloy.

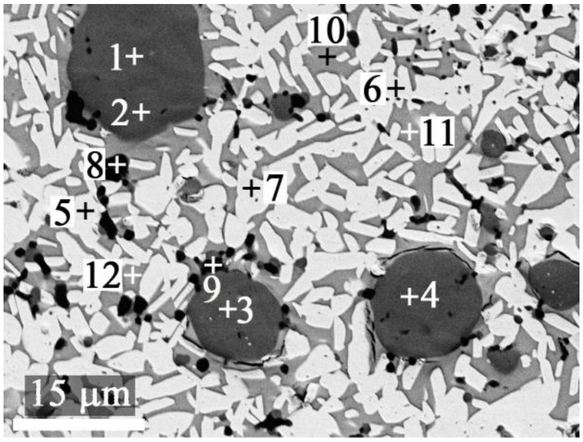

Figure 5-7. SEM BSE image of annealed U-12Zr-4Pd-5Ln. Corresponding EDS data are listed in

Table 5-4. EDS results for points shown in Figure 5-7. Values in atomic%.

	U	Zr	Pd	Nd	Ce	Pr	La	Phase[a]
1	0.6	0.8	51.9	26.2	10.2	7.5	2.8	LnPd
2	0.5	0.7	52.2	27.1	9.6	7.4	2.5	LnPd
3	0.5	0.3	51.8	23.6	12.5	8.1	3.3	LnPd
4	0.4	0.3	52.1	23.7	11.8	7.9	3.7	LnPd
5	97.3	0.8	1.6	0.0	0.1	0.2	0.0	α-U
6	96.8	0.8	1.6	0.0	0.4	0.4	0.0	α-U
7	97.0	0.8	1.5	0.0	0.3	0.3	0.1	α-U
8	3.9	94.9	0.9	0.2	0.1	0.0	0.0	α or β-Zr
9	0.8	88.4	6.1	2.4	1.4	0.7	0.2	α or β-Zr
10	38.3	59.7	1.7	0.0	0.1	0.1	0.0	δ-UZr2
11	36.2	61.7	1.8	0.0	0.2	0.1	0.0	δ-UZr2
12	35.5	62.4	1.7	0.0	0.2	0.1	0.1	δ-UZr2

a. Suggested phase based on EDS analysis.

TEM analysis was also performed on the annealed U-12Zr-4Pd-5Ln alloy. Figure 5-8 shows SEM images of the lamella location and the finished lamella. Figure 5-9 shows the HAADF-STEM images of the lamella, with EDS analysis indicated, and the data listed in Table 5-5. SAED data were collected at points 1, 4, 7, and 10 in Figure 5-9a and is shown in Figure 5-10. Based on the SAED patterns, the phases identified are β-Zr, δ-UZr_2, and α-U, although in some cases that is not obvious from the EDS data. Point 7 is clearly δ-UZr_2, but the EDS data indicates a 1:3 U to Zr ratio. There is a significant amount of dissolved Zr at that location. Likewise, point 3 in Figure 5-9a also has a significant amount of dissolved Zr. The higher concentrations of Zr in some of the points analyzed may be due to the proximity to the Pd-Ln precipitate. As $PdZr_2$ decomposes to form the more stable PdLn compounds, there should be a localized increase of Zr. It seems reasonable the anneal time was not long enough to allow the system to reach equilibration, thus Zr is dissolved in the phases present around the Pd-Ln precipitate.

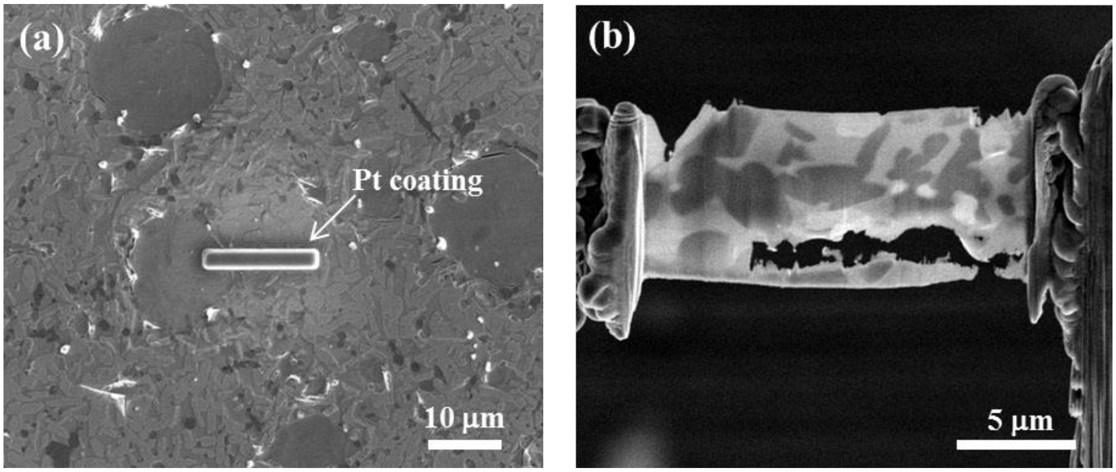

Figure 5-8. SEM images of U-12Zr-4Pd-5Ln showing (a) the location of FIB lift-out and (b) the prepared TEM lamella.

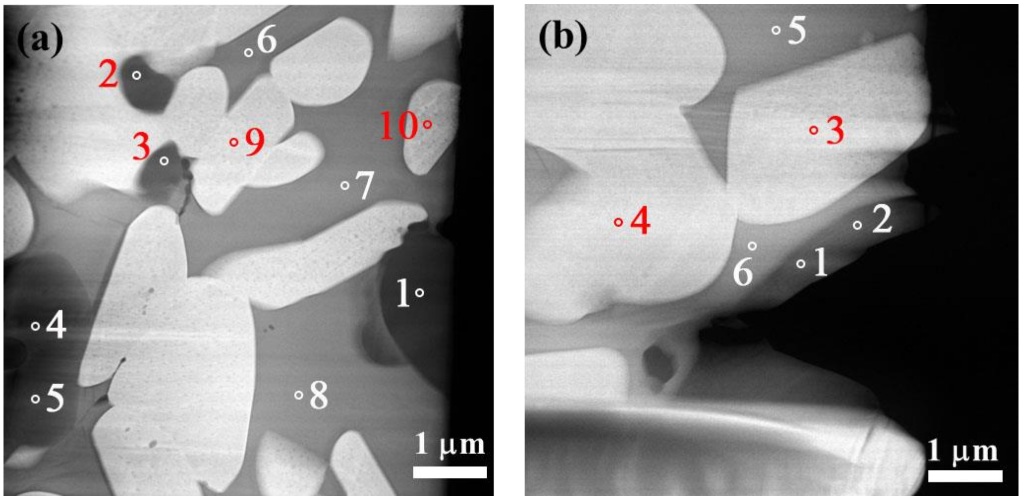

Figure 5-9. (a) and (b) STEM images of U-12Zr-4Pd-5Ln lamella. Corresponding EDS data are listed in Table 5-5.

Table 5-5. EDS data for points shown in Figure 5-9. Values in atomic%.

	U	Zr	Pd	Nd	Ce	Pr	La	Phase[a]
Figure 5-9a								
1	0	99.4	0.3	0	0	0.2	0.1	α or β-Zr
2	1.6	66.9	31.4	0	0.1	0	0	$PdZr_2$
3	2.1	70.1	27.9	0	0	0	0	$PdZr_2$
4	0.1	0.2	66.7	16.2	13.1	3.3	0.4	Pd_2Ln
5	1.2	1.9	58.4	22.2	10.7	3.0	2.7	Pd_3Ln_2
6	36.0	64.0	0	0	0	0	0	δ-UZr_2
7	26.7	72.4	0	0	0.9	0	0	δ-UZr_2
8	35.7	63.8	0.5	0	0	0	0	δ-UZr_2

	U	Zr	Pd	Nd	Ce	Pr	La	Phase[a]
Figure 5-9a								
9	99.1	0	0	0	0.6	0.3	0	α-U
10	98.2	0	1.8	0	0	0	0	α-U
Figure 5-9b								
1	0	0.4	62.8	22.1	7.4	5.7	1.6	Pd_2Ln/Pd_3Ln_2
2	0	0	51.2	27.8	6.9	11.1	2.8	LnPd
3	98.4	0	1.6	0	0	0	0	α-U
4	99.4	0	0.6	0	0	0	0	α-U
5	38.5	60.6	0.8	0.1	0	0	0	δ-UZr_2
6	35.2	63.3	1.5	0	0	0	0	δ-UZr_2

a. Suggested phase based on EDS analysis.

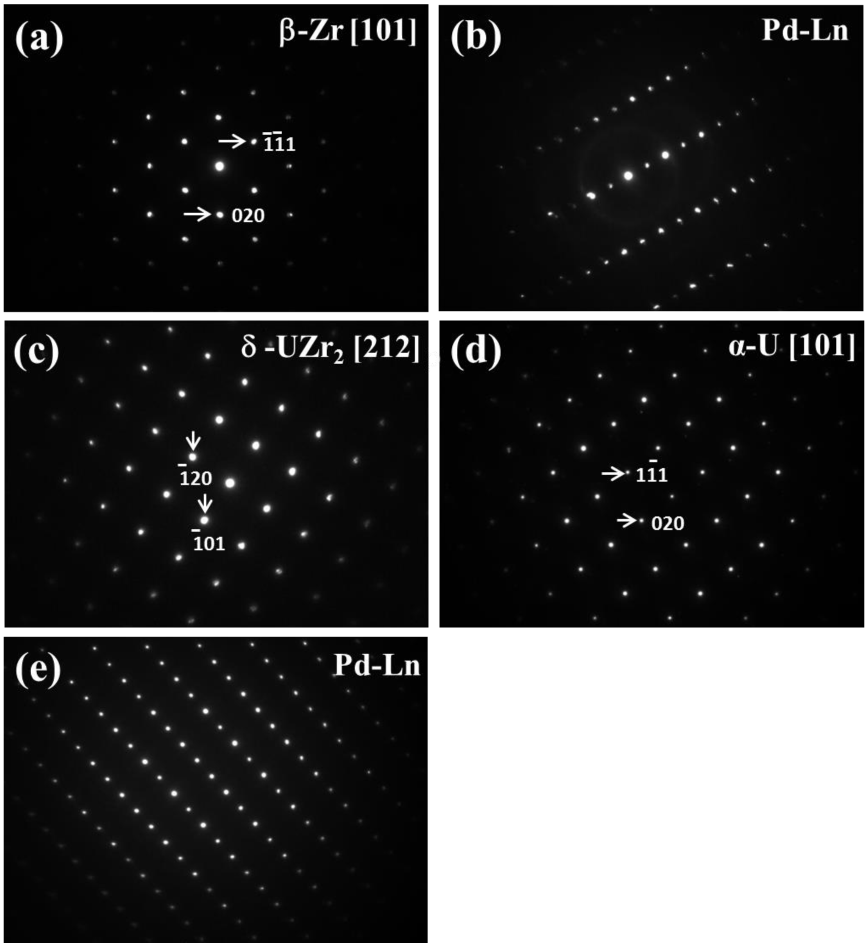

Figure 5-10. SAED patterns of (a) β-Zr [101], (b) Pd-Ln, (c) δ-UZr_2 [212] and (d) α-U [101], and (e) Pd-Ln in U-12Zr-4Pd-5Ln TEM lamella. The location of the collected diffraction patterns of (a), (b), (c), and (d) corresponds to points 1, 4, 7, and 10, respectively in Fig. 5.9a. (e) corresponds to point 1 in Figure 5-9b.

As stated above, $PdZr_2$ was not found in the SEM, but was located in the TEM analysis (Figure 5-9a, points 2 and 3). As evident in Figure 5-9a, these precipitates are sub-micron size, so are too small to analyze by EDS in the SEM. The roughly even distribution of Pd in the α-U, β-Zr, and δ-UZr_2 phases may be caused by the EDS analysis picking up these small $PdZr_2$ precipitates. In any case, the uniform distribution of Pd in these phases suggests rapid kinetics for the binding of lanthanides as they are further produced with increased fission.

The TEM analysis of the Pd-Ln precipitates is not as simple as it was in the SEM. Only one of the points (Figure 5-9b, point 2) corresponds to the 1:1 Pd-Ln compound. Point 4 in Figure 5-9a has the correct ratio for Pd_2Ln, point 5 in Figure 5-9a has the correct ratio for Pd_3Ln_2, and point 1 in Figure 5-9b has a ratio half way between these two phases, indicating a mixture of the two phases.

The SAED patterns shown in Figure 5-10b and 5-10e are for point 4 in Figure 5-9a and point 1 in Figure 5-9b, respectively. Diffraction data is not known for Pd_2Ln and Pd_3Ln_2 (where Ln = any of the four lanthanides, Nd, Ce, Pr, or La), thus indexing and identification of this diffraction pattern was not possible. Experiments are underway to characterize these Pd-rich phases.

Figure 5-10 shows the measured SAED patterns for β–Zr (Figure 5-10a), δ–UZr2 (Figure 5-10c), and α–U (Figure 5-10d). These phases were indexed using the data shown in Table 5-3. Although $PdZr_2$ was found in the TEM EDS analysis, the SAED pattern was not collected on any of these precipitates.

Of the binary phase diagrams for the constituents of Pd-Ln, the only complete diagram is the Pd-Nd phase diagram [50] (Figure 5-11); therefore, it will be used for this discussion. Note that the available data shown in the other binary phase diagrams for the Pd-Ln constituents are very similar to the Pd-Nd diagram, thus this diagram appears to be representative for all of them. The measured (by SEM) composition of the U-Zr-Pd-Ln alloy is 79.2U-11.7Zr-4.3Pd-4.8Ln in wt% (62.2U-24.0Zr-7.6Pd 6.3Ln in at%). Based on this composition, Pd is present with a molar excess of 20% compared to lanthanides. Removing the U and Zr from the composition and normalizing for Pd and Ln yields 54.6Pd-45.4Ln, making NdPd and Nd_3Pd_4 the expected phases. These stoichiometries conform to the SEM analysis, which found a 1:1 Pd to Ln ratio in the annealed microstructure, with the excess spread throughout the alloy. The previously reported characterization of as-cast U-15Zr-3.86Pd-4.3Ln in wt% (U-29.7Zr-6.5Pd-5.6Ln in at%) [7], also with a slight excess of Pd, found only the 1:1 Pd to Ln ratio, with excess Pd remaining primarily in Pd-Zr precipitates.

The discrepancy found between the SEM and the TEM data, i.e. different Ln-Pd phases detected, and $PdZr_2$ detected in the TEM, but not the SEM, can be explained by the resolution difference between TEM and SEM. The TEM EDS spot size is very small, and the data points collected, shown in Figure 5-9a and 5-9b, are roughly a micron apart. A composition change in an area this small cannot be differentiated in the SEM, resulting in an average of the phases present. This may account for the slightly elevated Pd content in the SEM EDS analysis. The spot size is large enough that Pd-rich phases are included in the measurement, but the 1:1 compound is likely the primary phase present.

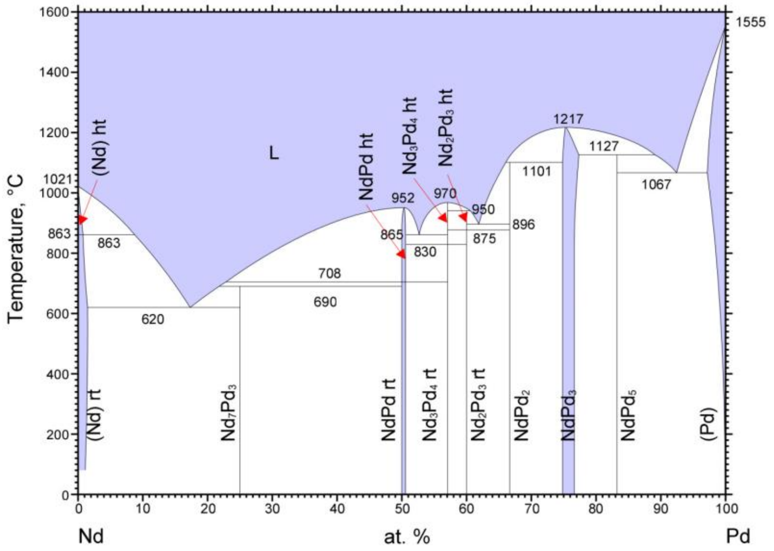

Figure 5-11. Pd-Nd binary phase diagram [50].

In a fuel during irradiation, the 1:1 Pd compound would be ideal for this system. The 1:1 compound has a high enough melting point (952°C) to be safe under reactor conditions, and the Pd is binding the maximum amount of fission product lanthanides (while maintaining a safe melt temperature). A Ln-rich compound is available (Ln_7Pd_3), but is not ideal based on the low melting eutectic temperature (620ºC, based on Pd-Nd binary phase diagram [50]). This compound was not observed in this study, although it is the likely phase present in the Ln-Pd precipitates characterized in the U-10Zr spent fuel [15]. In that system, Pd is only present as a fission product, thus not enough Pd is present to bind all the lanthanides produced, or to bind them in a 1:1 compound. The Pd-rich compounds have melt temperatures high enough to be safe in a reactor, but their presence indicates the available Pd is not being used efficiently. This assessment raises the following question: As the lanthanides burn-in, the Pd-rich compounds will likely form first, but are they thermodynamically stable enough to persist, or will they decompose to form the 1:1 compound? Exploring the thermodynamic stability of these compounds, as well as obtaining the structural parameters for the Pd-rich compounds, is underway.

5.5 Conclusions

In this investigation, the annealed microstructures of U-12Zr-4Pd wt% (67.6U-25.2Zr-7.2Pd at%) and U-12Zr-4Pd-5Ln (61.9U-24.5Zr-7.0Pd-6.6Ln at%) were analyzed by SEM and TEM. TEM was utilized to help resolve ambiguities in the previously characterized, as-cast U-Zr-Pd and U-Zr-Pd-Ln alloys [6], and to confirm phase assignments. The following conclusions can be drawn from the data presented:

- In both alloys investigated, α-U, α-Zr (β-Zr in this case due to quenching), and δ–UZr_2 are the phases present in the matrix. SEM EDS analysis indicates some solubility of Pd in the matrix, while the TEM shows very little, if any, Pd in the matrix. $PdZr_2$ was characterized in both alloys, although observation of this intermetallic in U-12Zr-4Pd-5Ln was limited to the TEM. Limitations in the SEM analysis (spot size, peak overlap) account for these differences.
- In the annealed microstructure, no evidence of a ternary phase between U, Zr, and Pd was observed, as was previously suggested [7]. The data presented does not rule out a metastable phase present in the as-cast system, but if this is the case, it will not survive in the reactor at temperature.

- There is a clear preference for Pd to bind the lanthanides, although the phases observed depend on the resolution of the analysis method. SEM indicates LnPd (1:1) is the only phase present, while TEM indicates LnPd, Pd_2Ln and Pd_3Ln_2 are formed. The Pd-rich compounds appear to be minor components of the Pd-Ln precipitates, but they indicate the Pd is not being utilized efficiently. The thermodynamic stability of the Pd-rich compounds versus the 1:1 compound is needed to fully understand the likely intermetallics formed, i.e. as the lanthanides burn-in, will Pd-rich Pd-Ln compounds react with the extra lanthanides to form the 1:1 Pd-Ln, or are the Pd-rich compounds stable enough to persist?

6. Microstructural characterization of as-cast U-20Pu-10Zr-3.86Pd and U-20Pu-10Zr-3.86Pd-4.3Ln

The full reference for the following manuscript is: M.T. Benson, L. He, J.A. King, R.D. Mariani, A. Winston, J. Madden, “Microstructural characterization of as-cast U-20Pu-10Zr-3.86Pd and U-20Pu-10Zr-3.86Pd-4.3Ln,” *J. Nuc. Mater.*, **2018**, *508*, 310-318.

6.1 Abstract

Palladium is being investigated as a potential additive to metallic fuel to bind fission product lanthanides, with the goal of reducing or preventing fuel-cladding chemical interactions (FCCI). A primary cause of FCCI is the lanthanide fission products moving to the fuel periphery and interacting with the cladding. This interaction will lead to wastage of the cladding and eventually to a cladding breach. The current study is a scanning electron microscopy (SEM) and transmission electron microscopy (TEM) investigation of as-cast U-20Pu-10Zr-3.86Pd and U-20Pu-10Zr-3.86Pd-4.3Ln in wt. %, where Ln = 53Nd-25Ce-16Pr-6La. In U-20Pu-10Zr-3.86Pd, $PdZr_2$ is forming, along with a possible ternary phase between Pu, Zr, and Pd. Pu is also present in the Pd-Ln precipitates formed in U-20Pu-10Zr-3.86Pd-4.3Ln. In the LnPd phase, Pu appears to be substitutional, forming (Ln,Pu)Pd. The other prominent phase, which appears to be Ln_7Pd_3, has a fine, lamellar structure. The lanthanides remain essentially constant across this fine structure, but Pu and Pd alternate as to which has the higher concentration.

6.2 Introduction

The goal of fuel development for advanced fast reactors is to create a nuclear fuel system that performs at high burnup while supporting the use of recycled actinides [51]. Based on the experience gained during the operation of Experimental Breeder Reactor-II (EBR-II) and the Fast Flux Test Facility (FFTF), metallic fuel alloys are of specific interest. Operation in these reactors demonstrated that metal fuels are capable of high burnup, are easy to fabricate, have high thermal conductivity, and significant safety benefits [52][53]. The metallic fuel alloy U-20Pu-10Zr was selected as the baseline fuel for the Integral Fast Reactor program based on steady-state and off-normal performance characteristics as well as compatibility with recycling technologies [54]. Experimentation in EBR-II showed U-Pu-Zr alloys had similar life limiting characteristics, such as fuel-cladding chemical interactions (FCCI), as compared to other fuel alloys [52]. One of the ways FCCI limits fuel lifetime is the fission product lanthanides (Ln) interaction with cladding. During irradiation the lanthanides tend to migrate to the periphery and cause the formation of intermetallics which lead to the weakening of the cladding and ultimately can lead to fuel rod failure. A variety of cladding materials have been tested with U-Zr and U-Pu-Zr fuels, including stainless steel (316SS), D9, and ferritic-martensitic alloys (HT-9), with HT-9 emerging as the most promising cladding, due to its resistance to radiation damage and FCCI [55]. All of these fuel/cladding combinations, even HT-9, have FCCI, thus methods to reduce FCCI are needed to allow higher burn-up.

Several methods are currently being evaluated to mitigate FCCI. Interior cladding coatings and barrier foils have been suggested to prevent diffusion of detrimental elements to and from the cladding [5][6][56]. Another approach is the addition of metals to bind Ln fission products. Several groups have reported initial success with additions of Sn [10], In [14], Sb [12][13], and Pd [4][7][8] to the fuel matrix.

The current study continues investigating Pd as a fuel additive. Previous investigations focused on U-Zr fuels [7][8], whereas this study is looking at the microstructural effects Pd has on a U-Pu-Zr fuel, with and without lanthanides present. Recent post-irradiation examination (PIE) results for a U-10Zr fuel pin irradiated in the Fast Flux Test Reactor [15] and U-Pu-Zr fuel pin part of the METAPHIX-2 experiment [57] found Pd-lanthanide precipitates. Palladium was present only as a fission product, thus there is not enough Pd to bind all of the lanthanides produced. The existence of Pd-lanthanide precipitates in an irradiated fuel indicates this method of controlling the lanthanides, i.e., an additive to bind the lanthanides, is already occurring naturally. This investigation is exploring the microstructural changes caused by adding Pd into the fuel to build upon what is already occurring naturally. The goal is to bind more of the lanthanides, which will allow higher fuel burn-up without significant FCCI.

The as-cast microstructures of U-20Pu-10Zr-3.86Pd and U-20Pu-10Zr-3.86Pd-4.3Ln are characterized with both scanning electron microscopy (SEM) and transmission electron microscopy (TEM). The specific amount of Pd used in these alloys corresponds to the amount of Pd needed to bind all the lanthanides at 20% burn-up (extrapolated from the chemical analysis of an EBR-II fuel pin at 8% burn-up [7]). This is also the amount of Pd used in the original journal article [7] discussing Pd as a fuel additive, thus providing continuity in the fuel-additive research program at Idaho National Laboratory. The composition and ratio of lanthanides are based on elemental analysis of irradiated U-10Zr EBR-II fuel pins [7], with the four most prevalent lanthanides included in the mix. The ratio obtained from elemental analysis is 53Nd-25Ce-16Pr-6La, in wt. %. The amount of lanthanides used in these alloys, 4.3 wt. %, corresponds to the amount of lanthanides produced at roughly 18% burn-up for U-10Zr fuel in the EBR-II reactor [7]. This lanthanide content is much higher than what was previously qualified (10% burn-up) by U.S. DOE. This content is somewhat arbitrarily investigated to reflect higher burn-ups desired plus lanthanide carryover in recycled fuel.

6.3 Experimental Methods

Two alloys were cast, U-20Pu-10Zr-3.86Pd in wt. % (54.9U-16.2Pu-21.7Zr-7.2Pd in at. %) and U-20Pu-10Zr-3.86Pd-4.3Ln wt. % (50.2U-15.8Pu-21.2Zr-7.0Pd-5.8Ln in at. %), where Ln=53Nd-25Ce-15Pr-6La in wt. % (52.3Nd-25.4Ce-16.2Pr-6.1La at. %). Palladium and the lanthanides were obtained from Alfa Aesar and used as received. The lanthanides were obtained as rods, packaged in mylar under argon.

All casting operations were carried out in an arc-melter within an argon atmosphere glovebox with high purity argon as a cover gas. When casting the alloys, after each addition step the button was flipped and re-melted 3 times to ensure homogeneity. To cast U-20Pu-10Zr-3.86Pd, the appropriate amount of U, Pu, Zr, and Pd were arc melted together in three steps. The first step was melting U and Pd together, followed by addition of Zr, and finally Pu. The specific addition order is not important. The elements were added separately to help ensure complete incorporation of each element prior to adding the next. The lanthanide mix was prepared by melting all 4 lanthanides together in one step. To cast U-20Pu-10Zr-3.86Pd-4.3Ln, the appropriate amount of the Ln alloy was mixed with the U-Pu-Zr-Pd pre-alloy, prepared with the same addition order as for U-20Pu-10Zr-3.86Pd. The buttons were cast into 5 mm diameter pins using a drop casting technique, and sectioned for analysis.

Scanning electron microscopy (SEM) was performed on a 2.5 mm section of the pin mounted in a 31.8 mm diameter phenolic metallographic (met) mount filled with epoxy. Samples were polished by grinding the surfaces flat with SiC grinding paper followed by polishing with polycrystalline diamond suspensions, starting with 9 µm, then 3 µm, and finally 1 µm. A gold coating was applied to reduce charging in the SEM.

The instrument used for this analysis was a JSM-7000f SEM manufactured by the Japan Electron Optics Laboratory (JEOL). The JSM-7000F is a hot field emission SEM equipped with energy dispersive X-ray spectrometer (EDS). The SEM was operated at an accelerating voltage of 20kV. Prior to analysis, X-ray detector response was verified using a copper target.

Transmission electron microscopy (TEM) samples were prepared by a FEI Quanta 3D field emission gun (FEG) dual beam focused ion beam (FIB) system. Platinum coating was deposited to protect the surface before cutting. TEM lamellas were created by coarse trenching 20 × 15 × 15 µm samples using the FIB. Samples were thinned down in the FIB during a final milling step of 5 kV at 77 pA ion emission current until small perforations were observed. Ga ion beam damage was cleaned with a final polish using 2 kV at 27 pA ion emission current. A 200 kV JEOL JEM-2010 TEM and a 200 kV Titan Themis scanning transmission electron microscopes (STEM) equipped with super-X EDS system were used for structure and composition analysis. TEM data for U-20Pu-10Zr-3.86Pd were collected on the JEOL JEM-2010 TEM, while data for U-20Pu-10Zr-3.86Pd-4.3Ln were collected on the Titan Themis STEM.

Chemical analysis was carried out on both alloys to confirm elemental composition. Concentrations of U, Pu (Pu-239 through Pu-242), Zr, Pd, Nd, Ce, Pr, and La were measured using inductively coupled plasma mass spectrometry (ICP-MS).

6.4 Results and Discussion

6.4.1 U-20Pu-10Zr-3.86Pd

Chemical analysis of U-20Pu-10Zr-3.86Pd indicates the composition is U-20.8Pu-9.8Zr-3.4Pd wt. % (U-20.5Pu-25.8Zr-7.7Pd at. %). The measured composition is very close to the target composition (U-20Pu-10Zr-3.86Pd in wt. %). The alloy will be referred to by the target composition (in wt. %) throughout the text.

A representative backscattered electron (BSE) image of U-20Pu-10Zr-3.86Pd is shown in Figure 6-1. This large area view appears very similar to as-cast U-10Zr-3.86Pd [7], i.e., the precipitates run along grain boundaries, with no large precipitates present.

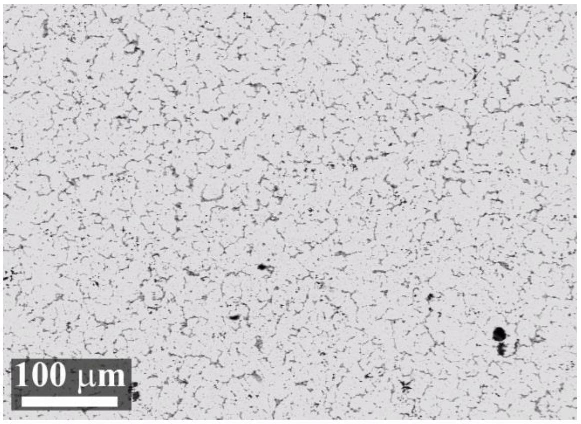

Figure 6-1. Low magnification BSE image for U-20Pu-10Zr-3.86Pd.

The higher magnification image shown in Figure 6.2 shows the light and dark regions in the matrix, with EDS data listed in Table 6-1. There are several differences in the light and dark regions of the matrix. There is an increase in the amount of Zr, from ~17-19 at. % in the light areas (points 1–4, Figure 6-2a, Table 6-1) to ~25-30 at. % in the dark areas (points 5-8), and a decrease in the amount of Pu, from ~17-19 at. % in the light areas to ~15 at. % in the dark areas. The amount of Pd increases, from ~1.5 at. % in the light areas to ~ 3.5 at. % in the dark areas. Using an extrapolated ternary phase diagram for U-Pu-Zr [4], the phases present should be δ-UZr_2, α-U, and ζ-(U,Pu). With only a small amount of Pd present in the matrix (1-3 at. %), this is likely an accurate description, although the phases cannot be differentiated in the as-cast alloy. In similar U-Zr-Pu systems [58][59], a heat treatment was required to separate the phases. This has also been observed in the as-cast microstructures in U-10Zr fuels. The δ-UZr_2 phase comes out of a partially ordered ω-UZr_2 phase upon heating [60]. This is likely the reason the phases cannot be differentiated in this related U-Pu-Zr system. Due to this, no phases are suggested in Table 6-1 for the matrix areas.

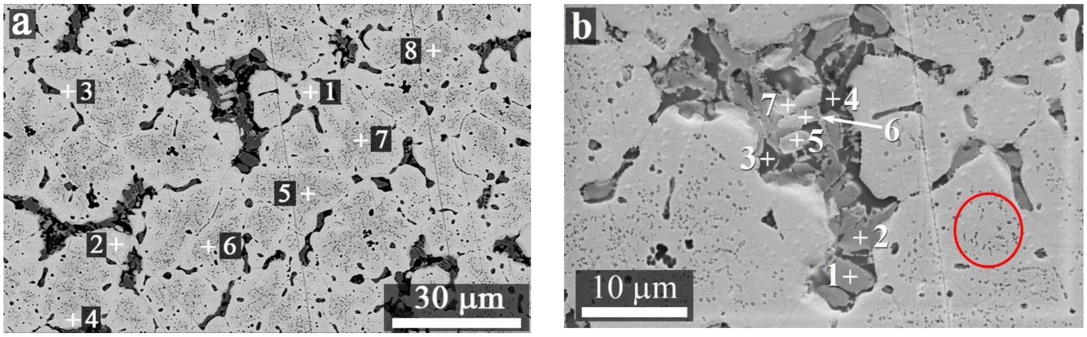

Figure 6-2. a. and b. BSE for U-20Pu-10Zr-3.86Pd showing EDS points. The red circle in 6-2b highlights sub-micron inclusions, discussed below in the TEM analysis. Corresponding EDS data are listed in Table 6-1.

Table 6-1. EDS data for points shown in Figure 6-2. Values in atomic %.

	U	Pu	Zr	Pd	Phase[a]
Figure 6-2a					
1	63.4	17.6	17.6	1.4	—
2	60.3	19.6	17.5	2.6	—
3	60.6	18.0	19.8	1.6	—
4	64.5	18.1	16.2	1.2	—
5	55.6	14.5	26.6	3.3	—
6	56.6	15.0	24.9	3.5	—
7	53.0	14.8	28.0	4.2	—
8	51.2	15.1	30.2	3.6	—
Figure 6-2b					
1	1.3	19.2	33.1	46.5	—
2	0.9	19.8	32.9	46.5	—
3	1.4	3.8	62.9	31.9	$PdZr_2$
4	1.0	3.7	64.1	31.2	$PdZr_2$
5	50.9	22.2	25.2	1.7	—
6	44.1	23.5	30.3	2.2	—
7	52.3	22.2	23.9	1.5	—

a. Suggested phase based on EDS analysis.

The larger structures, with an example shown in Figure 6-2a with a magnified view in Figure 6-2b, appear to have multiple phases present. This structure has a ternary eutectic microstructure, but for simplicity will be referred to as a precipitate. The dark grey regions (EDS points 1 and 2 in Figure 6-2b and Table 6-1) have a rough composition of 20Pu-33Zr-47Pd, with very little U. There is no ternary phase data available for Pu, Zr, and Pd, thus possible ternary phases are unknown. The EDS analysis indicates the black areas (EDS points 3 and 4 in Figure 6-2b and Table 6-1) are $PdZr_2$, with a small amount of U and Pu, although the U and Pu values may be an artifact due to the spatial resolution of SEM EDS. The third phase present in the precipitates is a light grey area (EDS points 5-7 in Figure 6-2b and Table 6-1). These areas appear to be matrix trapped in the precipitate. The composition is close to the dark matrix regions, with slightly lower U content and higher Pu content, although the composition doesn't match either the light or dark matrix areas.

The different phases present in the precipitate are all generally small in size, making EDS analysis by SEM less reliable. To better characterize the precipitate shown in Figure 6-2b, a lamella was removed with the FIB for TEM analysis. Due to the strain present in the as-cast alloy, the lamella was not able to be thinned for electron diffraction analysis in TEM. When thinning, the lamella would curl upon themselves, thus preventing removal of lamella thin enough for electron diffraction analysis. Figure 6-3a shows an image of the same precipitate presented in Figure 6-2b, with the platinum deposit indicating the location of the lamella. The finished lamella is shown in Figure 6-3b. The STEM image of the lamella (rotated and inverted based on the image shown in Figure 6-3b) is shown in Figure 6-4, with the location of EDS analysis shown. Corresponding EDS data is listed in Table 6-2. In the STEM image, the greyscale is reversed from the SEM images shown in Figure 6-2. The black precipitates in Figure 6-2b now appear as the light colored areas, while the matrix is dark.

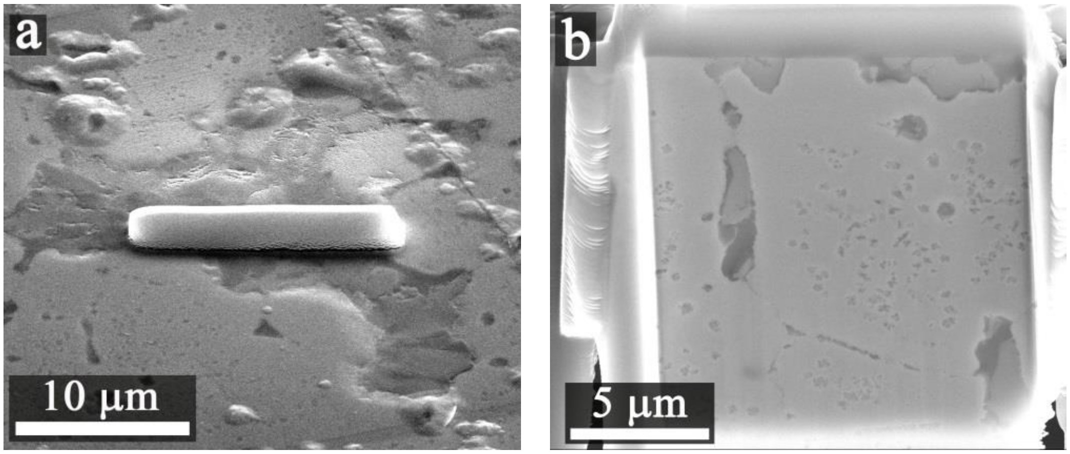

Figure 6-3. a. Location of lamella liftout in U-20Pu-10Zr-3.86Pd. Precipitate corresponds to precipitate shown in Figure 6-2b; b. Finished lamella.

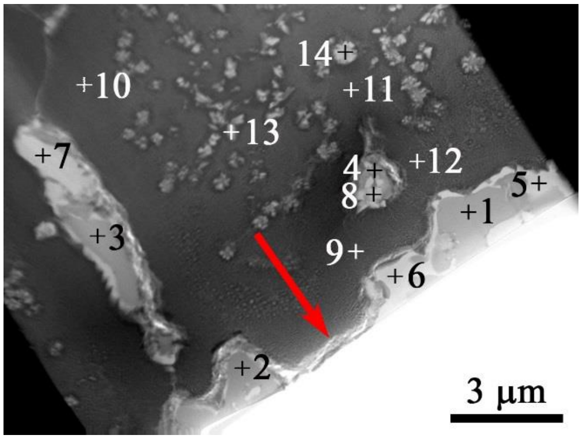

Figure 6-4. STEM brightfield image of U-20Pu-10Zr-3.86Pd. Corresponding EDS data are listed in Table 6-2.

Table 6-2. EDS data for points shown in Figure 6-4. Values in atomic %.

	U	Pu	Zr	Pd	Phasea
1	1.25	16.60	28.72	53.43	—
2	2.05	19.97	24.84	53.14	—
3	1.88	15.81	30.97	51.34	—
4	2.54	15.39	33.02	49.05	—
5	1.22	2.95	58.91	36.92	PdZr2
6	1.00	3.67	57.74	37.60	PdZr2
7	1.24	3.16	59.87	35.73	PdZr2
8	1.48	4.49	60.08	33.95	PdZr2
9	54.74	18.04	21.38	5.85	—
10	58.75	17.26	17.58	6.41	—
11	53.86	16.60	22.43	7.11	—
12	64.24	16.88	13.11	5.76	—
13	5.50	2.50	60.30	31.60	—
14	3.00	7.70	51.20	37.10	—

a. Suggested phase based on EDS analysis.

As shown in Figures 6-3b and 6-4, the precipitate is very shallow, extending roughly 2 μm below the surface. What was assumed to be trapped matrix material (EDS points 5-8 in Figure 6-2b and Table 6-1) is actually part of the bulk matrix. The location of the 'trapped' material is indicated by the red arrow in Figure 6-4.

Based on the EDS data listed in Table 6-2, the precipitate is mainly comprised of $PdZr_2$ (points 5–8 in Figure 6-4 and Table 6-2) and a phase with Pu, Zr, and Pd (points 1–4). As pointed out in the preceding SEM discussion, this could be a ternary phase, but there is not enough data to make that assertion. The composition, based on TEM EDS, is roughly 16Pu-30Zr-54Pd at. %, which is close to the measured composition on the SEM, 20Pu-33Zr-47Pd at. %. EDS points 9-12 were taken from the matrix, and show a rough composition of U-17Pu-20Zr at. %. As discussed, this should separate into α-U, δ-UZr_2, and ζ-(U-Pu) during annealing. This assumes the U-Zr-Pu composition in the matrix remains in the correct ratio to form α-U, δ–UZr_2, and ζ-(U-Pu). The formation of $PdZr_2$ and a potential ternary phase between Pu, Zr, and Pd will remove Pu and Zr from the matrix. Based on the extrapolated room temperature ternary phase diagram for U-Pu-Zr [4], if Zr is decreased to ~4 wt. % (U-18.4Pu-9.9Zr at. %), only α-U and ζ-(U-Pu) will form, and if Pu is decreased to ~8 wt. % (U-6.7Pu-22.5Zr at. %), only α-U and δ–UZr_2 will be present. The actual matrix composition will be some combination of these possibilities.

A Pd-rich ternary phase between Pd, Pu, and Zr could be beneficial for the metallic fuel properties, specifically the solidus/liquidus temperatures. A ternary compound, such as 16Pu-30Zr-54Pd at. %, could be beneficial in two ways. First, roughly 0.55 at. % Zr is removed for each at. % Pd, leaving considerably more Zr in the matrix, as compared to $PdZr_2$, and second, Pu is removed from the matrix and consumed in a ternary compound. Due to the lower Pu concentration in the matrix, and the higher Zr concentration in the matrix, the solidus/liquidus temperatures of the alloy will increase, approaching the original solidus/liquidus temperatures of U-20Pu-10Zr. A thorough characterization of this possible ternary phase is required in order to evaluate the possible benefits. The fraction of ternary phase being formed in the alloy is also needed to evaluate its effect on the solidus and liquidus temperatures.

The last two EDS points shown in Figure 6.4 (points 13 and 14) correspond to the sub-micron inclusions found in the matrix. These inclusions are present on the surface, as highlighted in Figures 6-2a and 6-2b with the red circle, and throughout the matrix. EDS analysis indicates the composition is roughly $PdZr_2$.

Sub-micron inclusions have been observed in previous U-Zr and U-Pu-Zr alloys [30][61][62]. In those alloys, the inclusions were high Zr deposits, believed to be stabilized by small amounts of oxygen or nitrogen. With the addition of Pd, the inclusions are clearly not the same as previously characterized. In the related alloy, as-cast U-15Zr-3.86Pd [7], sub-micron inclusions may be visible in the microstructure, although there was no characterization of the inclusions.

6.4.2 U-20Pu-10Zr-3.86Pd-4.3Ln

In order to explore the effects lanthanides may have on the fuel microstructure, an alloy including lanthanides was fabricated. Chemical analysis of U-20Pu-10Zr-3.86Pd-4.3Ln indicates the composition is U-19.5Pu-9.0Zr-2.7Pd-2.4Ln wt. % (U-19.0Pu-23.5Zr-6.0Pd-4.0Ln at. %), where Ln=50.5Nd-28.5Ce-15.5Pr-5.4La wt. % (49.8Nd-29.0Ce-15.7Pr-5.5La at. %). Uranium, Pu, and Zr are very close to target concentrations, but the composition is low in both Pd and lanthanides. There is still a small excess of Pd over the lanthanides (2.0 at. % excess), as was planned in the target composition (50.2U-15.8Pu-21.2Zr-7.0Pd-5.8Ln in at. %). A smaller amount of Pd and lanthanides should not affect the analysis presented in this manuscript, but there will be less Pd-lanthanide precipitates available for analysis. The alloy will be referred to by the target composition (in wt. %) throughout the text.

A representative large area view of U-20Pu-10Zr-3.86Pd-4.3Ln is shown in Figure 6-5a, with a magnified region shown in Figure 6-5b. The locations of EDS analysis are shown in Figure 6-5b, with the corresponding data listed in Table 6-3.

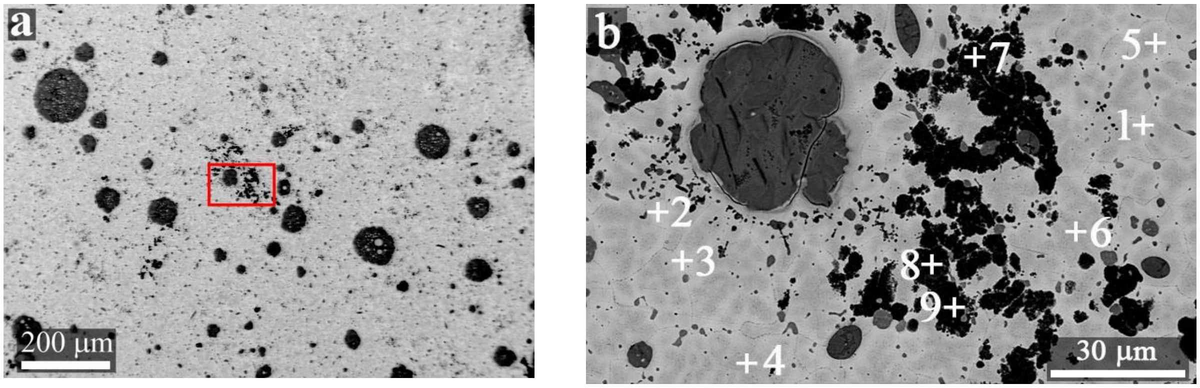

Figure 6-5. a. and b. BSE image of U-20Pu-10Zr-3.86Pd-4.3Ln. Corresponding EDS data are listed in Table 6-3. The red rectangle in 6-5a indicates the location of the magnified image in 6-5b.

Table 6-3. EDS data for points shown in Figure 6-5b. Values in atomic %.

	U	Pu	Zr	Pd	Nd	Ce	Pr	La
1	59.6	14.7	23.9	1.9	0.0	0.0	0.0	0.0
2	63.4	15.6	18.8	1.4	0.0	0.4	0.4	0.0
3	61.6	16.3	19.4	2.1	0.0	0.4	0.3	0.0
4	47.4	14.9	33.7	3.3	0.0	0.3	0.3	0.0
5	47.8	14.1	33.5	4.2	0.0	0.3	0.0	0.0
6	45.4	14.3	36.5	3.5	0.0	0.1	0.2	0.0
7	12.9	12.7	61.3	6.1	3.7	2.2	1.2	0.0
8	18.5	13.7	59.0	7.6	0.3	0.8	0.2	0.0
9	16.0	13.8	45.5	17.3	2.4	4.0	1.0	0.0

In the images shown in Figure 6-5, two precipitate types are apparent; the mostly round, grey precipitates and the randomly-shaped black precipitates. The grey precipitates vary in size and are distributed throughout the alloy. The black precipitates are small, and while they are also dispersed throughout the alloy, they appear in concentrated, larger regions, as shown in Figure 6.5. EDS data for the black precipitates (points 7-9 in Figure 6-5b and Table 6-3) show mixed compositions. The precipitates are high in Zr, with roughly 13 at. % Pu and 13-19 at. % U. A small amount of Pd is present, as well as measurable quantities of lanthanides in 2 of the points (points 7 and 9). This is in contrast to similar appearing black precipitates previously reported in U-15Zr-3.86Pd-4.3Ln, which are primarily Zr and Pd [7].

Figure 6-6 shows the magnified image of a precipitate. The locations for EDS analysis are shown, with corresponding EDS data listed in Table 6-4. There are multiple phases present in the precipitates: a light grey and black lamellar structure, indicated by red arrows in Figure 6.6 and EDS points 4–6, a darker grey solid structure, indicated by EDS points 1–3, and the black inclusions, indicated by EDS points 7–9. The red arrows point to the most obvious examples of the fine lamellar structure, but it is spread throughout this region of the precipitate. This microstructure is representative of all the grey, round precipitates observed. A full discussion of the precipitate microstructure, based on both SEM and TEM data, is given after the TEM data is presented.

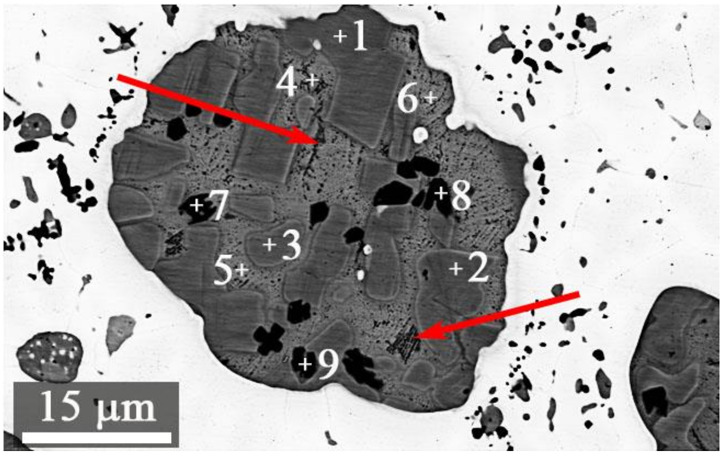

Figure 6-6. BSE of a precipitate in U-20Pu-10Zr-3.86Pd-4.3Ln. Red arrows indicate the fine lamellar structure. Corresponding EDS data are listed in Table 6-4.

Table 6-4. EDS data for points shown in Figure 6-6. Values in atomic %.

	U	Pu	Zr	Pd	Nd	Ce	Pr	La	Phase[a]
1	0.4	5.5	1.7	51.7	27.8	5.7	5.5	1.6	(Ln,Pu)Pd
2	0.4	5.1	1.6	51.4	28.4	5.6	5.7	1.7	(Ln,Pu)Pd
3	0.3	5.7	2.0	51.6	27.7	5.6	5.4	1.7	(Ln,Pu)Pd
4	0.0	8.4	2.3	26.3	32.7	15.1	10.4	4.9	Ln_7Pd_3
5	0.0	8.3	2.1	23.1	33.4	16.8	11.3	5.1	Ln_7Pd_3
6	0.0	8.0	2.4	24.1	33.6	16.2	10.6	5.0	Ln_7Pd_3
7	0.4	0.9	3.8	2.2	63.3	12.7	12.2	4.5	Ln oxides
8	0.6	0.9	4.4	1.5	63.4	12.6	12.2	4.3	Ln oxides
9	0.4	1.3	3.5	4.3	62.3	12.2	12.2	3.8	Ln oxides

a. Suggested phase based on EDS analysis.

The present work can be compared to prior work on alloys that did not contain Pu. The microstructure of as-cast U-10Zr-3.86Pd-4.3Ln is shown in Figure 6-7, with corresponding EDS data listed in Table 6-5, for comparison to the precipitate shown in Figure 6-6. The large area view is essentially the same as for the previously reported U-15Zr-3.86Pd-4.3Ln [7], although a magnified image of a precipitate was not included in that work. There are primarily two phases present in the precipitate, shown in Figure 6-7b, with small white or black inclusions as well. EDS analysis indicates the phases are LnPd and Ln_7Pd_3. There is a small molar excess of Pd present, although some of the Pd remained outside of the precipitates with Zr, pushing the Pd to Ln balance to the Ln-rich side.

The phases present in U-20Pu-10Zr-3.86Pd-4.3Ln appear to be the same as found in U-10Zr-3.86Pd-4.3Ln, i.e., the 1:1 compound (LnPd and (Ln,Pu)Pd), and Ln_7Pd_3. A significant difference between the structures is the lack of fine, lamellar structure in the Ln_7Pd_3 phase in U-10Zr-3.86Pd-4.3Ln, indicated by the red arrows in Figure 6-6. This fine structure present in Ln_7Pd_3 phase in U-20Pu-10Zr-3.86Pd-4.3Ln is a direct result of Pu. A comparison of the elemental composition between these precipitates, one with and one without Pu, is discussed below.

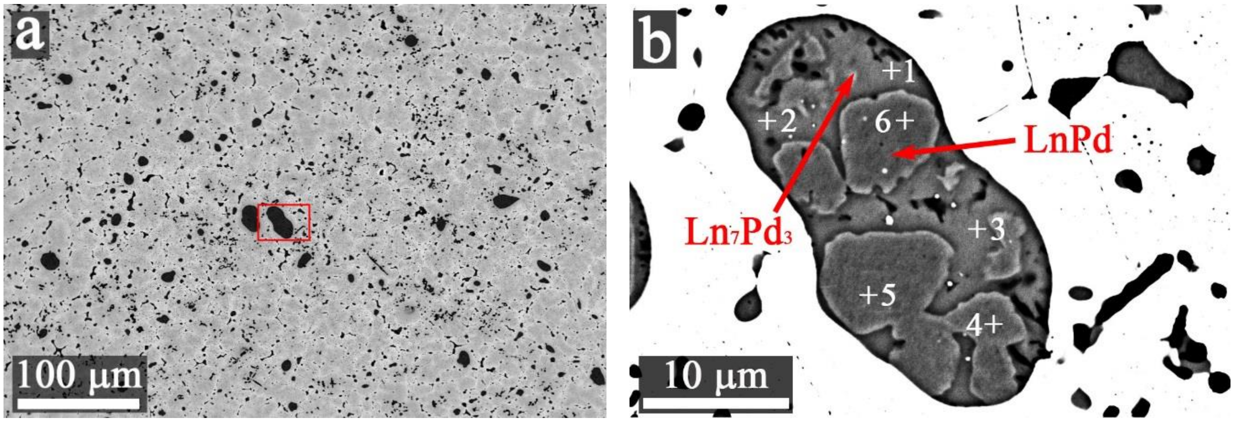

Figure 6-7. BSE of as-cast U-10Zr-3.86Pd-4.7Ln. a. large area view, b. magnified region, indicated in 6-7a by the red rectangle. Corresponding EDS data listed in Table 6-5.

Table 6-5. EDS data for points shown in Figure 6-7. Values in atomic %.

	U	Zr	Pd	Nd	Ce	Pr	La	Phase[a]
1	0.3	0.4	31.6	31.4	17.5	11.6	7.2	Ln_7Pd_3
2	0.5	0.3	31.9	31.6	17.1	11.7	7.0	Ln_7Pd_3
3	0.3	0.3	32.0	31.9	16.9	11.6	7.0	Ln_7Pd_3
4	0.4	0.4	51.1	28.6	8.2	7.9	3.3	LnPd
5	0.4	0.4	51.6	28.1	8.2	7.9	3.3	LnPd
6	0.5	0.2	51.3	28.5	8.3	7.9	3.3	LnPd

a. Suggested phase based on EDS analysis.

A lamella of U-20Pu-10Zr-3.86Pd-4.3Ln was prepared with the FIB for TEM analysis. The lamella was lifted from the same precipitate that is shown in Figure 6-6. As with the U-20Pu-10Zr-3.86Pd lamella, the stresses in the as-cast alloy prohibited thinning the lamella enough to take electron diffraction measurements. The location the lamella was lifted from is shown in Figure 6-8a with deposited platinum, with the finished lamella shown in Figure 6-8b. Figure 6-9 shows the STEM image of the lamella, as well as EDS mapping performed with the STEM. EDS analysis was taken from the mapping data, indicated by the white rectangles in Figure 6-9, with the corresponding data listed in Table 6-6. The red arrows indicate an overlapping region of the lamella, caused by internal stresses in the alloy.

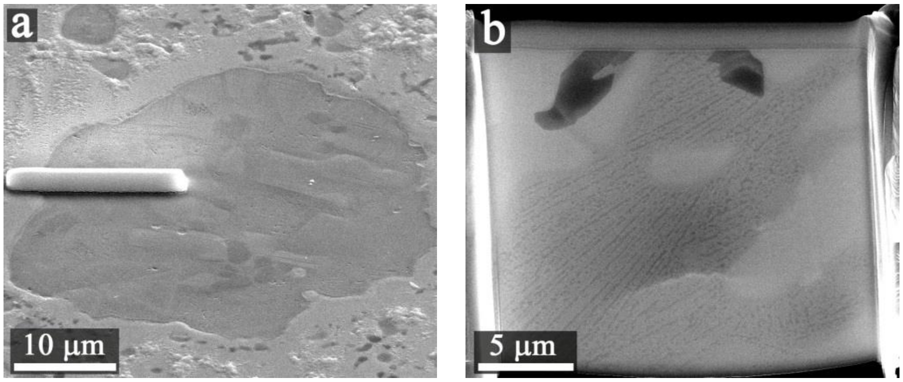

Figure 6-8. a. location of lamella liftout in U-20Pu-10Zr-3.86Pd-4.3Ln. Precipitate corresponds to precipitate shown in Figure 6-6, b. finished lamella.

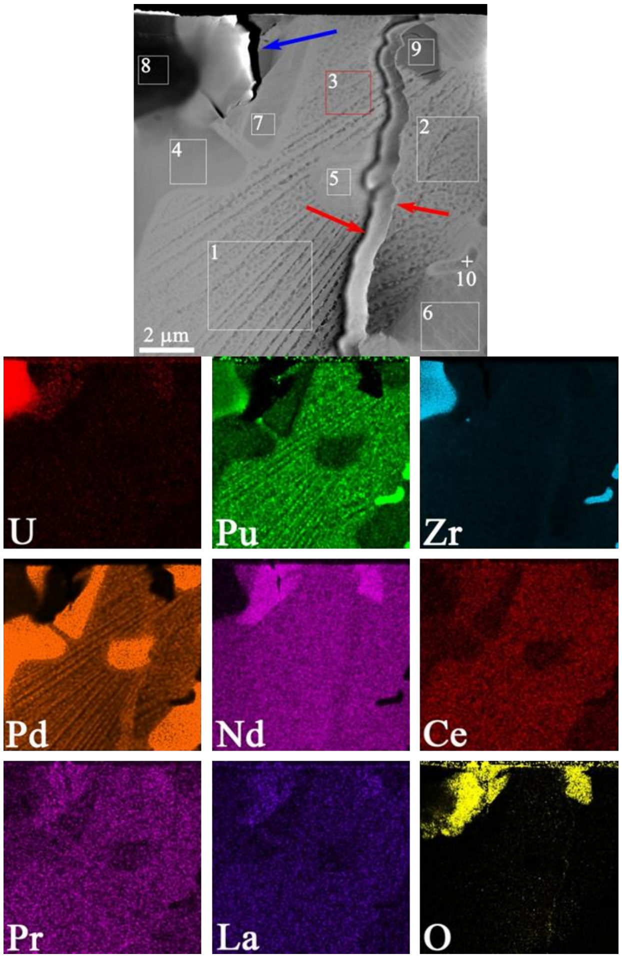

Figure 6-9. STEM dark field image of U-20Pu-10Zr-3.86Pd-4.3Ln with EDS mapping. The locations for EDS analysis are indicated with white rectangles. Corresponding EDS data is listed in Table 6-6. The red square (EDS point 3) indicates the location of the magnified region shown in Figure 6-10. The red arrows indicate an overlapping section of the lamella, the blue arrow indicates a tear in the lamella.

Table 6-6. EDS data for regions shown in Figure 6-9. Values in atomic %.

	U	Pu	Zr	Pd	Nd	Ce	Pr	La	Phase[a]
1	2.10	14.63	3.70	23.50	27.62	12.50	8.77	7.19	Ln_7Pd_3
2	1.98	14.22	3.64	23.77	26.83	13.15	9.01	7.39	Ln_7Pd_3
3	2.06	14.29	3.62	22.57	29.09	12.53	9.05	6.78	Ln_7Pd_3
4	1.59	7.88	2.62	45.91	23.36	7.07	6.46	5.10	LnPd
5	1.42	7.70	2.54	43.44	27.87	6.84	5.88	4.30	LnPd
6	1.30	7.58	2.46	44.53	25.77	6.95	6.44	4.97	LnPd
7	1.36	8.67	2.79	43.73	26.70	5.93	6.27	4.55	LnPd
8	45.27	12.33	17.76	5.48	4.16	4.62	5.19	5.19	—
9	0.64	1.39	5.38	2.12	67.07	8.37	8.58	6.45	Ln
10	1.8	63.4	20.1	2.1	3.4	3.7	3.2	2.4	Pu_4Zr

a. Suggested phase based on EDS analysis.

The bulk of the precipitate shown in Figure 6-6 is comprised of two structures. If Pu is excluded from the EDS data in Table 6-4, the ratio of Ln to Pd indicates the phases are Ln_3Pd_4 (points 1-3) and Ln_7Pd_3 (points 4-6). It is very unlikely to have a Pd-rich phase and a Ln-rich phase in the same precipitate. If Pu is included with the lanthanides, points 1-3 now have the correct ratio to be (Ln,Pu)Pd. This is not the case for Ln_7Pd_3, though. The Ln to Pd ratio is correct without including Pu. The TEM EDS data, shown in Figure 6-9 and listed in Table 6-6, indicates the same two phases in the precipitate, i.e., (Ln,Pu)Pd and Ln_7Pd_3. However, the amount of measured Pu is significantly higher in the TEM data, at 14 at. % in Ln_7Pd_3 (compared to 8 at. % in the SEM EDS data, Figure 6-6), and ~8 at. % in (Ln,Pu)Pd (as compared to 5 at. % in the SEM EDS data).

The role of Pu in the precipitates is not readily apparent. There does not appear to be any ternary phases present, although there is no data available for ternary compositions of Pu, Pd, and Nd (or any of the relevant lanthanides), thus more data is needed to determine if ternary phases are present. The data indicates a substitutional compound is being formed, where Pu is substituting into the crystal lattice of LnPd in place of the lanthanides, forming (Ln,Pu)Pd. This is based on the ratios of lanthanides, Pd, and Pu measured using EDS analysis. The EDS data does not indicate this is happening in Ln_7Pd_3, though, based on the ratio of lanthanides to Pd. Pu may simply be dissolved (interstitial) in this phase. The binary phase diagrams between Pu and the lanthanides indicate some Pu solubility in the lanthanides at high lanthanide concentrations (except for the Ce-Pu phase diagram [63], which is incomplete in this region). The Nd-Pu binary phase diagram [64] indicates that roughly 7 at. % Pu is soluble in Nd. The Pr-Pu and La-Pu phase diagrams [65][66] indicate lower Pu solubility, around 3 at. %. The solubility of Pu in Pd is higher, around 14 at. % [67]. The Ln_7Pd_3 phase contains roughly 14 at. % Pu (Table 6-6). The solubility of Pu in the lanthanides and in Pd may account for the Pu concentration, but this can't be confirmed without phase data for the ternary systems.

In addition to the change in Pu concentration between the phases, there is also a drop in Ce concentration. The Ce decrease is also present in U-10Zr-3.86Pd-4.3Ln, as shown in Table 6-5, where Ce drops from 17 at. % in Ln_7Pd_3 to 8 at. % in LnPd. In U-10Zr-3.86Pd-4.3Ln, the normalized ratio of lanthanides in the Ln_7Pd_3 phase is 45.7Nd-26.2Ce-17.3Pr-10.9La wt. %, and the normalized ratio of lanthanides in the LnPd phase is 58.9Nd-17.4Ce-16.7Pr-7.1La wt. %. With Pu present in the precipitate, Figure 6-9 and Table 6-6, the normalized ratio of lanthanides present in Ln_7Pd_3 is 49.2Nd-22.5Ce-15.8Pr-12.6La wt. %, and is 59.4Nd-15.4Ce-14.4Pr-10.8La wt. % for (Ln,Pu)Pd. Although there are differences in the normalized ratios, the trends are clear. The ratio of lanthanides in Ln_7Pd_3 is close to the ratio of lanthanides added when fabricating the alloy, i.e. 53Nd-25Ce-16Pr-6La wt. %. In both of the 1 to 1 precipitates (LnPd or (Ln,Pu)Pd), the ratio of lanthanides is high in Nd and low in Ce. This is important to point out since the addition of Pu into the phases does not appear to change the lanthanide composition in the precipitates.

The lamella, shown in Figures 6-8 and 6-9, is primarily of the precipitate, with only a small amount of the matrix region present in the upper left of the image. EDS point 8 (Table 6-6) corresponds to this area, and is a mix between the bulk matrix and the precipitate. The rest of the precipitate is comprised of primarily two compositions. The areas marked as 1, 2, and 3 in Figure 6-9 and Table 6-6 correspond to Ln_7Pd_3, while the areas marked as 4, 5, 6, and 7 correspond to (Ln,Pu)Pd.

In addition to Ln_7Pd_3 and (Ln,Pu)Pd, two Ln-rich areas were observed, one of them marked as area 9 for EDS analysis, and a small area comprised of Pu and Zr, point 10 in Table 6-6. Based on the Pu-Zr binary phase diagram [68], the structure of this is Pu_4Zr, with extra Zr dissolved. The TEM EDS data for the Ln-rich areas agree with the SEM data (points 7-9 in Figure 6-6, Table 6-4), in that Nd is more abundant than the other lanthanides, which is apparent in both the EDS data and in the mapping shown in Figure 6-9. The high oxygen present in the Ln-rich areas, based on the oxygen map shown in Figure 6-9, indicate the lanthanides are present as lanthanide oxides. The source of oxygen was likely the lanthanide starting materials. The lanthanides were packaged in mylar under argon, and opened in an argon glovebox, but there was still obvious oxidation on the surface upon opening.

The changes in concentration between (Ln,Pu)Pd and Ln_7Pd_3 are represented visually in the mapping images shown in Figure 6-9. Upon close examination, the mapping also shows a compositional change in the lamellar structure in Ln_7Pd_3, which is not apparent from the EDS data listed in Table 6-6. The fine lamellar structure indicates the higher concentrations of Pd and Pu alternate, although there is no obvious change in the lanthanide concentrations in this region. To further explore this, a very high magnification region, taken from the area marked with the red rectangle in Figure 6-9, was analyzed, and is shown in Figure 6-10. The Titan TEM has a resolution of 1 nm, thus data listed in Table 6-7 represents an average composition for the area of the circles. The circles labeled 1 through 4 indicate areas with higher Pd concentration, around 33 at. % as compared to ~20 at. % for the circles labeled 5 through 8. The Pu concentration starts at ~12 at. % for the circles labeled 1 through 4, and increases to ~23 at. % for the circles labeled 5 through 8. The only other obvious difference in these lamellar structures is a very small increase in Ce (~2 at. %) in the areas with higher Pu. These changes in concentration mirror the trends observed for the different phases in the precipitate, i.e. the phase with the higher concentration of Pd, namely (Ln,Pu)Pd, has a lower concentration of Pu and Ce, while the inverse is true for Ln_7Pd_3. This is represented visually in the mapping images shown in Figure 5-10 for Pd, Pu, Ce, and Nd. The remaining elements, U, Zr, Pr, and La, are evenly dispersed in this region, so were not included in the mapping images. The maps for Pd and Pu clearly show the alternating fine structure present. Ce is noticeably higher in concentration wherever there is Pu, while Nd is evenly dispersed, except in the areas with high Ce and Pu.

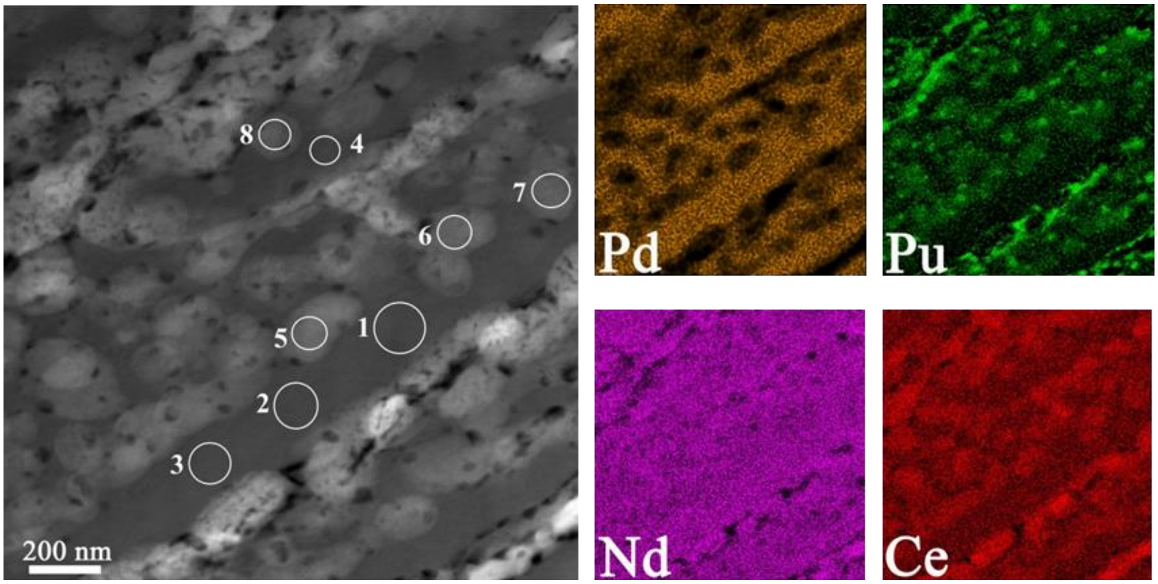

Figure 6-10. Magnified STEM brightfield image of U-20Pu-10Zr-3.86Pd-4.3Ln, with mapping images for Pd, Pu, Ce, and Nd. The location of this area is shown with the red rectangle in Figure 6-9. The locations for EDS analysis are indicated with white circles. Corresponding EDS data are listed in Table 6-7.

Table 6-7. EDS data for the regions shown in Figure 6-10. Values in atomic %.

	U	Pu	Zr	Pd	Nd	Ce	Pr	La
1	1.89	12.51	3.00	32.78	24.78	10.96	8.56	5.51
2	1.98	11.93	2.92	33.78	23.58	10.54	8.57	6.69
3	1.73	11.59	2.89	31.85	25.16	10.77	9.88	6.14
4	1.82	11.95	2.89	34.71	24.70	10.42	8.86	4.66
5	1.67	22.31	3.29	20.24	23.01	13.20	9.91	6.37
6	1.79	23.78	3.63	20.02	21.89	14.02	8.95	5.91
7	1.68	19.73	2.93	24.41	22.90	12.14	9.31	6.90
8	1.94	23.10	3.84	19.81	22.49	12.48	10.16	6.19

In Table 6-5, the ratio of lanthanides to Pd is very close to the ratio for Ln_7Pd_3 (~2.4 for data shown in Table 6-5, ideal ratio for Ln_7Pd_3 is 2.33), although the data in Table 6-7 indicates the ratio is an average taken across the fine lamellar structure. The Ln to Pd ratio varies between 1.5 for the Pd-rich areas (circles 1-4) to 2.6 for the Pu-rich areas (circles 5-8). The measured lanthanide concentration varies from 49 at. % to 52.5 at. %. The only change in specific lanthanides is a small increase (~3 at. %) in Ce in circles 5-8, corresponding to the increase in Pu.

The fine lamellar structure may only be present in the as-cast alloy. A heat treatment will likely cause this area to either separate into more than one phase, or collapse down to one phase. The characterization of the annealed structure is underway, but is outside the scope of this manuscript.

6.5 Conclusions

Palladium has been added to U-20Pu-10Zr transmutation fuel, with and without lanthanides present. The microstructural characterization of these alloys is to assess the ability of Pd, in an out-of-pile investigation, to bind and constrain the lanthanides, with the goal of preventing FCCI during irradiation. The following conclusions can be drawn from the data presented:

- A ternary phase between Pu-Zr-Pd may be forming in U-20Pu-10Zr-3.86Pd wt. %. A ternary phase will effectively increase the Zr concentration in the matrix, and decrease the Pu concentration in the matrix. Both of these effects are advantageous on the solidus/liquidus temperatures of the fuel, both fresh fuel and in-pile. Characterization of this possible ternary phase is needed to better understand its influence in the fuel alloy.
- In U-20Pu-10Zr-3.86Pd-4.3Ln, there are primarily two phases present in the precipitates, LnPd and Ln_7Pd_3. In the LnPd phase, Pu appears to be substitutional into the structure, creating a (Ln,Pu)Pd phase.
- At the nanometer scale, the Ln_7Pd_3 phase has a fine lamellar structure with multiple phases present. The average of these phases corresponds to Ln_7Pd_3 with Pu dissolved in the phase, and not substitutional in the crystal lattice. A heat treatment will likely cause the fine structure to separate into multiple phases, or condense into one phase.
- The lanthanide composition in the precipitates is consistent with previous characterizations of Pd-Ln precipitates. The presence of Pu does not alter lanthanide composition in the precipitates.

7. ACKOWLEDGEMENTS

The authors gratefully acknowledge the Department of Nuclear Energy, Advanced Fuels Campaign of the Nuclear Technology R&D Program in the Office of Nuclear Energy, under DOE-NE Idaho Operations Office Contract DE-AC07-05ID14517.

8. REFERENCES

[1] D. D. Keiser, “Fuel-Cladding Interaction Layers in Irradiated U-Zr and U-Pu-Zr Fuel Elements,” 2006.

[2] W. J. Carmack, H. M. Chichester, D. L. Porter, and D. W. Wootan, “Metallography and fuel cladding chemical interaction in fast flux test facility irradiated metallic U-10Zr MFF-3 and MFF-5 fuel pins,” *J. Nucl. Mater.*, vol. 473, pp. 167–177, 2016.

[3] S. D. Herrmann and S. X. Li, “Separation and Recovery of Uranium Metal from Spent Light Water Reactor Fuel Via Electrolytic Reduction and Electrorefining,” *Nucl. Technol.*, vol. 171, no. 3, pp. 247–265, 2010.

[4] R. D. Mariani, D. L. Porter, S. L. Hayes, and J. R. Kennedy, “Metallic Fuels: The EBR-II legacy and recent advances,” in *ATALANTE 2012, Nuclear Chemistry for Sustainable Fuel Cycles*, 2012, pp. 513–520.

[5] K. S. Lee, I. Y. Kim, W. Lee, and Y. S. Yoon, “Effect of Zr Thin Film on Zr Foil as a FCCI Barrier Between Lanthanide (La-Ce) and Clad Material,” *Met. Mater. Intnl.*, vol. 21, pp. 498–503, 2015.

[6] W. Y. Lo and Y. Yang, “Vanadium diffusion coating on HT-9 cladding for mitigating the fuel cladding chemical interactions,” *J. Nucl. Mater.*, vol. 451, no. 1–3, pp. 137–142, 2014.

[7] R. D. Mariani, D. L. Porter, T. P. O’Holleran, S. L. Hayes, and J. R. Kennedy, “Lanthanides in metallic nuclear fuels: Their behavior and methods for their control,” *J. Nucl. Mater.*, vol. 419, no. 1–3, pp. 263–271, 2011.

[8] M. T. Benson, L. He, J. A. King, and R. D. Mariani, “Microstructural characterization of annealed U-12Zr-4Pd and U-12Zr-4Pd-5Ln: Investigating Pd as a metallic fuel additive,” *J. Nucl. Mater.*, vol. 502, 2018.

[9] M. T. Benson, L. He, J. A. King, R. D. Mariani, A. J. Winston, and J. W. Madden, “Microstructural characterization of as-cast U-20Pu-10Zr-3.86Pd and U-20Pu-10Zr-3.86Pd-4.3Ln,” *J. Nucl. Mater.*, vol. 508, 2018.

[10] M. T. Benson, J. A. King, R. D. Mariani, and M. C. Marshall, “SEM characterization of two advanced fuel alloys: U-10Zr-4.3Sn and U-10Zr-4.3Sn-4.7Ln,” *J. Nucl. Mater.*, vol. 494, 2017.

[11] M. T. Benson, J. A. King, and R. D. Mariani, *Investigation of tin as a fuel additive to control FCCI*, vol. Part F12. 2018.

[12] Y. Xie, M. T. Benson, J. A. King, R. D. Mariani, and J. Zhang, “Characterization of U-Zr fuel with alloying additive Sb for immobilizing fission product lanthanides,” *J. Nucl. Mater.*, vol. 498, 2018.

[13] Y. Xie, J. Zhang, M. T. Benson, and R. D. Mariani, “Thermodynamic stability studies of Ce-Sb compounds with Fe,” *J. Nucl. Mater.*, vol. 499, 2018.

[14] Y. S. Kim *et al.*, “Effect of indium addition in U-Zr metallic fuel on lanthanide migration,” *J. Nucl. Mater.*, vol. 484, pp. 297–306, 2017.

[15] J. M. Harp, D. L. Porter, B. D. Miller, T. L. Trowbridge, and W. J. Carmack, “Scanning electron microscopy examination of a Fast Flux Test Facility irradiated U-10Zr fuel cross section clad with HT-9,” *J. Nucl. Mater.*, vol. 494, pp. 227–239, 2017.

[16] G. W. Egeland, R. D. Mariani, T. Hartmann, D. L. Porter, S. L. Hayes, and J. R. Kennedy, “Reduction of FCCI effects in lanthanide-iron diffusion couples by doping with palladium,” *J. Nucl. Mater.*, vol. 440, no. 1–3, pp. 178–192, 2013.

[17] G. W. Egeland, R. D. Mariani, T. Hartmann, D. L. Porter, S. L. Hayes, and J. R. Kennedy, “Reducing fuel-cladding chemical interaction: The effect of palladium on the reactivity of neodymium on iron in diffusion couples,” *J. Nucl. Mater.*, vol. 432, no. 1–3, pp. 539–544, 2013.

[18] S. K. Jha *et al.*, “Microstructural and textural evolution during hot deformation of dilute Zr-Sn alloy,” *J. Nucl. Mater.*, vol. 482, pp. 12–18, 2016.

[19] N. Keskar, K. V. Mani Krishna, D. Srivastava, and G. K. Dey, “Effect of Sn content and texture on the twinning behaviour of Zr-Sn binary alloys at low temperature,” *J. Nucl. Mater.*, vol. 465, pp. 71–77, 2015.

[20] S. Liu, Y. Zhan, J. Wu, and X. Wei, “Insight into structural, mechanical, electronic and thermodynamic properties of intermetallic phases in Zr-Sn system from first-principles calculations,” *J. Phys. Chem. Solids*, vol. 86, pp. 177–185, 2015.

[21] J. Wang, K. Wang, C. Ma, and L. Xie, “Critical evaluation and thermodynamic optimization of the (U + Bi), (U + Si) and (U + Sn) binary systems,” *J. Chem. Thermodyn.*, vol. 92, pp. 158–167, 2016.

[22] A. K. Pattanaik, R. Kandan, K. Nagarajan, and P. R. Vasudeva Rao, “Gibbs energies of formation of the intermetallic compounds of U-Sn system,” *J. Alloys Compd.*, vol. 551, pp. 249–254, 2013.

[23] C. B. Basak, “Microstructural evaluation of U-rich U-Zr alloys under near-equilibrium condition,” *J. Nucl. Mater.*, vol. 416, no. 3, pp. 280–287, 2011.

[24] Y. U. Kwon and J. D. Corbett, “The Zirconium–Tin System, with Particular Attention to the Zr5Sn3-Zr5Sn4 Region and Zr4Sn,” *Chem. Mater.*, vol. 2, no. 1, pp. 27–33, 1990.

[25] J. T. McKeown *et al.*, “Coexistence of the α and δ phases in an as-cast uranium-rich U-Zr alloy,” *J. Nucl. Mater.*, vol. 436, no. 1–3, pp. 100–104, 2013.

[26] R. I. Sheldon, E. M. Foltyn, and D. E. Peterson, “Sn-U (Tin-Uranium),” in *Binary Alloy Phase Diagrams, II*, T. B. Massalski, Ed. 1990, pp. 3409–3410.

[27] H. Okamoto, “U-Zr (Uranium-Zirconium),” *J. Phase Equilibria*, vol. 14, pp. 267–268, 1993.

[28] S. Ahn, S. Irukuvarghula, and S. M. McDeavitt, “Thermophysical investigations of the uranium-zirconium alloy system,” *J. Alloys Compd.*, vol. 611, pp. 355–362, 2014.

[29] “Reactor Fuels and Materials Development Plutonium Research: 1966 Annual Report (Mound Laboratory Report MLM-1402),” Miamisburg, OH, 1967.

[30] D. E. Janney and T. P. O’Holleran, “Zr inclusions in actinide-Zr alloys: New data and ideas about how they form,” *J. Nucl. Mater.*, vol. 460, pp. 13–15, 2015.

[31] I. P. Semitelou, J. K. Yakinthos, and R. E., “Amplitude-modulated magnetic structure of Nd5Sn3,” *J. Magn. Magn. Mater.*, vol. 128, pp. 79–82, 1993.

[32] F. Weitzer, K. Hiebl, and P. Rogl, “Crystal chemistry and magnetism of neodymium stannides including compounds of the structural series REnSn3n-2,” *J. Solid State Chem.*, vol. 98, no. 2, pp. 291–300, 1992.

[33] M. T. Benson, “Unpublished data.”

[34] G. Borzone, A. Borsese, and R. Ferro, “ON THE ALLOYING BEHAVIOUR OF CERIUM WITH TIN,” *J. Less-Common Met.*, vol. 85, pp. 195–203, 1982.

[35] G. Borzone, A. Borsese, and R. Ferro, “A Contribution to the Study of the Alloying Behaviour of the Rare Earths with Tin,” *Zeitschrift fur Anorg. und Allg. chemie*, vol. 501, no. 6, pp. 199–208, 1983.

[36] E. Franceschi, “DIMORPHISM OF LasSns, Ce,Sn, AND Pr,Sn, COMPOUNDS,” *J. Less-Common Met.*, vol. 66, pp. 175–181, 1979.

[37] L. W. Finger, D. E. Cox, and A. P. Jephcoat, “A correction for powder diffraction peak asymmetry due to axial divergence,” *J. Appl. Crystallogr.*, vol. 27, pp. 892–900, 1994.

[38] H. Okamoto, “The Sb-Zr (antimony-zirconium) system,” *J. Phase Equilibria*, vol. 14, no. 2, pp. 228–231, 1993.

[39] B. Legendre, E. Dichi, and V. Vassiliev, “The phase diagram of the In-Sb-Sn system,” *Zeitschrift Fur Met.*, vol. 92, no. 4, pp. 328–335, 2001.

[40] H. Okamoto, “Sb-Zr (Antimony-Zirconium),” in *Binary Alloy Phase Diagrams, II*, T. B. Massalski, Ed. 1990, pp. 3320–3323.

[41] V. D. Abulkhaev, “Neodymium-Antimony System,” *Russ. J. Inorg. Chem.*, vol. 44, no.2, pp. 264—267, 1999.

[42] H. Okamoto, “Ce-Sb (Cerium-Antimony),” *J. Phase Equilibria*, vol. 22, p. 88, 2001.

[43] M. T. Benson, J. A. King, J. M. Harp, and R. D. Mariani, “Controlling FCCI with Pd in Metallic Fuel,” in *Proceedings of Fast Reactor 17*, 2017.

[44] B. F. Hills, B. R. Butcher, B. W. Howlett, and D. Stewart, “The effect of cooling rate on the decomposition of the γ-phase in uranium-zirconium alloys,” *J. Nucl. Mater.*, vol. 16, no. 1, pp. 25-38, 1965.

[45] S. Irukuvarghula, S. Ahn, and S. M. McDeavitt, “Decomposition of the γ phase in as-cast and quenched U-Zr alloys,” *J. Nucl. Mater.*, vol. 473, pp. 206–217, 2016.

[46] H. Blank, “Fractional packing densities and fast diffusion in uranium and other light actinides,” *J. Alloys Compd.*, vol. 268, no. 1–2, pp. 180–187, 1998.

[47] T. A. Badaeva and G. K. Alekseenko, “Diagramma Sostoyaniya Sistemy Torii Tsirkonii,” *Zhurnal Neorg. Khimii*, vol. 4, no. 8, pp. 1873–1880, 1595.

[48] S. N. Klyamkin and K. N. Semenenko, “High pressure hydride phases formation in Ti2Ni- and MoSi2-type intermetallic compounds,” *J. Alloys Compd.*, vol. 253–254, no. 1997, pp. 41–43, 1997.

[49] E. R. Boyko, “The structure of the δ phase in the uranium–zirconium system,” *Acta Crystallogr.*, vol. 10, no. 11, pp. 712–713, 1957.

[50] H. Okamoto, “Nd-Pd (Neodymium-Palladium),” *J. Phase Equilibria*, vol. 13, pp. 220–222, 1992.

[51] W. J. Carmack *et al.*, “Metallic fuels for advanced reactors,” *J. Nucl. Mater.*, vol. 392, no. 2, pp. 139–150, 2009.

[52] D. C. Crawford, D. L. Porter, and S. L. Hayes, “Fuels for sodium-cooled fast reactors: US perspective,” *J. Nucl. Mater.*, vol. 371, no. 1–3, pp. 202–231, 2007.

[53] D. E. Burkes, R. S. Fielding, and D. L. Porter, “Metallic fast reactor fuel fabrication for the global nuclear energy partnership,” *J. Nucl. Mater.*, vol. 392, no. 2, pp. 158–163, 2009.

[54] Y. I. Chang, "The Integral Fast Reactor," *Nucl. Technol.*, vol. 88, no. 2, pp. 129–138, 1989.

[55] C. Matthews, C. Unal, J. Galloway, D. D. Keiser, and S. L. Hayes, "Fuel-cladding chemical interaction in U-Pu-Zr metallic fuels: A critical review," *Nucl. Technol.*, vol. 198, no. 3, pp. 231-259, 2017.

[56] S. W. Yang, H. J. Ryu, J. H. Kim, B. O. Lee, and C. B. Lee, "FCCI barrier performance of electroplated Cr for metallic fuel," *J. Nucl. Mater.*, vol. 401, no. 1–3, pp. 98–103, 2010.

[57] L. Capriotti *et al.*, "Characterization of metallic fuel for minor actinides transmutation in fast reactor," *Prog. Nucl. Energy*, vol. 94, pp. 194–201, 2017.

[58] D. E. Janney and J. R. Kennedy, "As-cast microstructures in U-Pu-Zr alloy fuel pins with 5-8 wt.% minor actinides and 0-1.5 wt% rare-earth elements," *Mater. Charact.*, vol. 61, no. 11, pp. 1194–1202, 2010.

[59] A. Aitkaliyeva, J. W. Madden, C. A. Papesch, and J. I. Cole, "TEM identification of subsurface phases in ternary U-Pu-Zr fuel," *J. Nucl. Mater.*, vol. 473, pp. 75–82, 2016.

[60] S. Irukuvarghula and S. M. McDeavitt, "Formation Mechanism of Delta Phase in the As-cast U-10wt%Zr Alloy," in *Transactions of the American Nuclear Society*, 2013, pp. 612–615.

[61] D. E. Janney, J. R. Kennedy, J. W. Madden, and T. P. O'Holleran, "Crystal structure of high-Zr inclusions in an alloy containing U, Pu, Np, Am, Zr and rare-earth elements," *J. Nucl. Mater.*, vol. 448, no. 1–3, pp. 109–112, 2014.

[62] S. Mukherjee, S. Kaity, M. T. Saify, S. K. Jha, and P. K. Pujari, "Evidence of zirconium nano agglomeration in as-cast dilute U-Zr alloys," *J. Nucl. Mater.*, vol. 452, no. 1–3, pp. 1–5, 2014.

[63] H. Okamoto, "Ce-Pu (Cerium-Plutonium)," in *Binary Alloy Phase Diagrams, II*, T. B. Massalski, Ed. 1990, pp. 1100–1101.

[64] H. Okamoto, "Nd-Pu (Neodymium-Plutonium)," in *Binary Alloy Phase Diagrams, II*, T. B. massalski, Ed. 1990, pp. 2799–2800.

[65] H. Okamoto, "Pr-Pu (Praseodymium-Plutonium)," in *Binary Alloy Phase Diagrams, II*, T. B. Massalski, Ed. 1990, pp. 3091–3092.

[66] H. Okamoto, "La-Pu (Lanthanum-Plutonium)," in *Binary Alloy Phase Diagrams, II*, T. B. Massalski, Ed. 1990, pp. 2413–2415.

[67] H. Okamoto, "Pd-Pu (Palladium-Plutonium)," in *Binary Alloy Phase Diagrams, II*, T. B. Massalski, Ed. 1990, pp. 3033–3035.

[68] H. Okamoto, "Pu-Zr (Plutonium-Zirconium," *J. Phase Equilibria*, vol. 16, pp. 287–288, 1995.